

# **IMU-based Suit for Strength Exercises: Design, Calibration and Tracking**

Thesis approved by  
the Department of Computer Science  
Technische Universität Kaiserslautern  
for the award of the Doctoral Degree:  
Doctor of Engineering (Dr.-Ing.)

to

**Sarvenaz Salehi Mourkani**

Date of Defence: 16 April 2021

Dean: Prof. Dr. Jens Schmitt

Reviewer: Prof. Dr. Didier Stricker

Reviewer: Prof. Dr. Karsten Berns







# Abstract

Wearable systems have been applied in various studies as a convenient and efficient solution for monitoring health and fitness. There is a large number of commercial products in the growing market of wearable systems that can be worn as wristbands, clasps, or in the form of clothing. However, these systems only provide general information about the intensity and possibly the type of user activity, which is not sufficient for monitoring strength and conditioning exercises. To achieve optimal muscular development and reduce the risk of exercise-related injury, a wearable system should provide reliable biomechanical details of body movements as well as real-time feedback during training. In addition, it should be an affordable, comfortable, and easy-to-use platform for different types of users with different levels of movement intensity and work autonomously over long periods of time. These requirements impose many challenges on the design of such systems. This study presents most of these challenges and proposes solutions.

In this work, a low-cost and light-weight tracking suit is designed and developed, which integrates multiple Inertial measurement units (IMUs). A novel data acquisition approach is proposed to improve the energy efficiency of the system without the use of additional devices.

Given a valid calibration, IMUs, comprising inertial sensors and magnetometers, can provide accurate orientation in three dimensions (3D). Unlike the inertial sensors, magnetometer measurements are easily disturbed by ferromagnetic materials in the vicinity of the sensor, either inside the IMU casing or in the final mounting position. Therefore, this work proposes a practical method for in-field magnetometer calibration and alignment to the coordinate system of an IMU. This method is verified experimentally in terms of magnitude deviation, heading error, plane projections, and repeatability. The results show a higher accuracy compared to the related works.

Sensor to body calibration is a critical requirement for capturing accurate body movements.

Therefore, a theoretical analysis of an existing method is carried out, showing its limited applicability for hip and knee joints. On this basis, by applying geometric constraints, a method is proposed for estimating the positions of three IMUs (mounted on the pelvis, upper leg, and lower leg) simultaneously. The result of experiments with different types of movements and arbitrary intensity shows that the proposed method outperforms the previous method.

Moreover, two real-time tracking algorithms based on the extended Kalman filter (EKF) are proposed for lower body motion estimation. The first approach provides an estimate of the pelvis orientation. The second approach estimates the position of IMUs and the joint angles with respect to the pelvis by incorporating the result of body-IMU calibration. The modeling of the biomechanical constraint compensates for lack of a reliable horizontal reference, e.g. Earth's magnetic field. Experiments to track strength exercises such as squat and hip abduction/adduction show promising results.

In order to finally provide a monitoring application in which users can follow the exercises according to the instructions and taking into account their health status, this work proposes an approach for the identification of exercises based on an online template matching algorithm, which detects the correct performance using a previously recorded exercise in the presence of a supervisor. Therefore, unlike most identification algorithms, no large datasets are required for training. The algorithm is optimized here to reduce execution time while maintaining the accuracy. Experiments show that for the specific application of this study, i.e. squat exercise monitoring, the proposed method outperforms the related works in optimization of online template matching.



# Acknowledgment

My PhD work is attributed to a great deal of help and support from so many wonderful people. Here I would like to express my gratitude to some of the most important ones.

First I want to thank Prof. Bengt Oelmann from Mid Sweden University, whose course in Design of Wireless Sensor Networks has inspired me to start working in the field of sensor networks and sensor fusion. This paved the way to my PhD position at DFKI in Kaiserslautern.

I would like to express my gratefulness to Prof. Dr. Didier Stricker for his support from the beginning and throughout my work. Didier thanks also for kindly accepting that I handed in my thesis after a long delay due to my new job. Your constructive comments has definitely helped me to improve the state of this thesis.

I especially thank Dr. Gabriele Blesser for her supervision and guidances. Gabi I learned alot from your enthusiasm, discipline and precision in the research and work.

I would like to thank my former colleagues at DFKI, who helped me to capture the dataset needed for evaluation of Body-IMU calibration, tracking and exercise identification. Mohammad Reza Yousefi, Jilliam Diaz Barros, Stephan Krauß, Johannes Köhler, Bernd Krolla, Vladimir Hasko, thank you all for patiently performing all those exercises and squats! I especially thank you Reza for your support in promoting my work and idea of start-up, including all your efforts in filming for the application of tracking suit.

For the purpose of evaluation I also used the simulation platform developed by my former colleague Markus Miezal. Thanks Sir! and also thank you so much for preparing such a nice and personal doctoral hat for me. Your energetic and happy mood was always a reminder that one can have fun even if the process of research and reaching good results could be tough and tiring.

I would very much like to thank Leivy Michelly Kaul for kindly helping me in administrative work and translations from the beginning and having always such a positive attitude.

I am also thankful to Prof. Dr. Berns and Prof. Dr. Deßloch for accepting to be the co-examiner and head of committee of my thesis review.

During my work at DFKI, I got to know great people, who remained my friends even after moving out of the city: Christiano/Prof. Gava, Mohamed Selim, Alain Pagani, Tewodros Amberbir Habtegebrial, Stephan, Jill, Jason Rambach, Markus, Gabi, Bertram Taetz, I was so happy to see you all after my defence and to be able to celebrate with you.

Finally, my biggest thanks go to my parents Siavash and Shahnaz, my sisters Golnaz and Sanaz

and my brother Salar, for always being there for me either when I wanted to celebrate my achievements or complain about my work, giving me their support and encouragement. To my beautiful family, from bottom of my heart I would like to say thank you so much cause I couldn't have done this without you and love you all.

*Stuttgart, May 2021*

*Sarvenaz Salehi*



# Contents

<b>1. Introduction</b>	<b>1</b>
1.1. Motivation . . . . .	1
1.1.1. Monitoring of strength exercises . . . . .	1
1.1.2. System for monitoring strength exercises . . . . .	4
1.1.3. Technology and social factors . . . . .	4
1.2. Problem Formulation . . . . .	5
1.3. Contributions . . . . .	6
1.4. Organization of the thesis . . . . .	9
<b>2. Background and Related Work</b>	<b>11</b>
2.1. IMU Calibration . . . . .	11
2.1.1. Parameter estimation: Data fitting . . . . .	12
2.2. Lower Body Movements . . . . .	13
2.2.1. Hip joint . . . . .	13
2.2.2. Knee joint . . . . .	14
2.2.3. Pelvic bone . . . . .	14
2.3. Body-IMU Calibration . . . . .	14
2.3.1. Static . . . . .	16
2.3.2. Functional . . . . .	18
2.3.3. Autocalibration . . . . .	18
2.4. Body Motion Tracking . . . . .	20
2.4.1. Kalman filter . . . . .	20
2.4.2. Extended Kalman filter . . . . .	21
2.4.3. Orientation estimation . . . . .	22
2.4.4. Lower Body Pose Estimation . . . . .	22
2.5. Exercise Monitoring . . . . .	24
2.5.1. Time series data mining . . . . .	25
2.5.2. Exercise identification . . . . .	26
<b>3. System Design</b>	<b>29</b>
3.1. Related Work . . . . .	29
3.1.1. Visual systems . . . . .	29
3.1.2. Inertial systems . . . . .	30
3.1.3. Magnetic systems . . . . .	31
3.1.4. Wearable motion monitoring systems . . . . .	31
3.2. Proposed system design . . . . .	34
3.2.1. Hardware design . . . . .	34

3.2.2.	Firmware design . . . . .	36
3.2.3.	Software . . . . .	39
3.3.	Experimental results . . . . .	40
3.3.1.	Power consumption . . . . .	40
3.3.2.	Weight and cost . . . . .	41
3.3.3.	Measurement Quality . . . . .	41
3.4.	Conclusion . . . . .	44
<b>4.</b>	<b>System Calibration</b>	<b>45</b>
4.1.	Inertial Sensors Calibration . . . . .	45
4.2.	Magnetometer Calibration . . . . .	46
4.2.1.	Parameters . . . . .	46
4.2.2.	Calibration Method . . . . .	47
4.2.3.	Experimental Results . . . . .	49
4.3.	Body-inertial measurement unit (IMU) Calibration . . . . .	56
4.3.1.	Problem formulation . . . . .	56
4.3.2.	Observability analysis . . . . .	58
4.3.3.	Seel <i>et al.</i> method with correction using joint axes . . . . .	59
4.3.4.	Proposed method . . . . .	60
4.3.5.	Joint Rotation Axis and Angle Estimation . . . . .	60
4.3.6.	Proposed measurement model . . . . .	62
4.3.7.	Constraints of three connected segments . . . . .	62
4.3.8.	Observability analysis of proposed method . . . . .	63
4.3.9.	Experimental results . . . . .	67
4.4.	Conclusion . . . . .	80
<b>5.</b>	<b>Lower Body Motion Tracking</b>	<b>83</b>
5.1.	Orientation estimation . . . . .	83
5.1.1.	Common Estimator . . . . .	83
5.1.2.	Extended Estimator . . . . .	85
5.1.3.	Experimental results . . . . .	85
5.2.	Pose Estimation . . . . .	89
5.2.1.	Kinematic Process Model . . . . .	89
5.2.2.	Observation Model . . . . .	90
5.2.3.	Experimental Results . . . . .	90
5.3.	Conclusion . . . . .	96
<b>6.</b>	<b>Exercise Identification</b>	<b>99</b>
6.1.	Offline dynamic time warping (DTW) . . . . .	99
6.2.	Online DTW . . . . .	100
6.2.1.	SPRING . . . . .	101
6.2.2.	Normalization-supported SPRING(NSPRING) . . . . .	102
6.2.3.	Improved SPRING(ISPRING) . . . . .	103
6.2.4.	Dynamic Normalization based Real-time Pattern Matching (DNRTPM) . . . . .	104

6.3.	Proposed method . . . . .	105
6.3.1.	Motion primitive detection . . . . .	105
6.3.2.	Feature extraction . . . . .	106
6.3.3.	Identification . . . . .	106
6.4.	Experimental Results . . . . .	110
6.4.1.	Identification with SPRING . . . . .	112
6.4.2.	Identification with ISPRING . . . . .	115
6.4.3.	Identification with NSPRING . . . . .	117
6.4.4.	Identification with DNRTPM . . . . .	119
6.4.5.	Identification with the proposed method . . . . .	121
6.4.6.	Performance comparison . . . . .	125
6.5.	Conclusion . . . . .	126
<b>7.</b>	<b>Conclusion</b>	<b>127</b>
7.1.	Results . . . . .	127
7.2.	Future Works . . . . .	129
7.2.1.	System design . . . . .	129
7.2.2.	Calibration . . . . .	129
7.2.3.	Pose Estimation . . . . .	130
7.2.4.	Exercise Identification . . . . .	131
<b>A.</b>	<b>Abbreviations</b>	<b>133</b>
<b>B.</b>	<b>Mathematical Notations</b>	<b>135</b>
<b>C.</b>	<b>Quaternion, Conversions and Filtering</b>	<b>137</b>
C.1.	Quaternion . . . . .	137
C.1.1.	Quaternion Derivative and Integration . . . . .	137
C.2.	Axis-Angle . . . . .	138
C.3.	Conversions . . . . .	138
C.3.1.	Quaternion to Rotation Matrix . . . . .	138
C.3.2.	Axis Angle to Rotation Matrix . . . . .	138
C.4.	Filtering . . . . .	139
C.4.1.	Accelerometer/Magnetometer Model Jacobian . . . . .	139
C.4.2.	Quaternion Jacobian . . . . .	139
	<b>List of figures</b>	<b>144</b>
	<b>List of tables</b>	<b>146</b>
	<b>Bibliography</b>	<b>159</b>



# 1. Introduction

Strength training is one of the critical components of most fitness and rehabilitation processes. When doing strength exercises, it is important to follow the correct routine to avoid injuries and achieve better results. Also, the final goal, e.g. the return to the sport in rehabilitation, is achieved by following a routine. Therefore, the monitoring of such exercises is advantageous with regard to performance improvement, injury prevention, and rehabilitation [13].

Wearable motion tracking systems are a convenient and efficient solution for monitoring sports activity. To this end, the wearable system should be ubiquitous, easy to use, and comfortable enough to be worn during exercises. The data provided should include biomechanical details of the movements, e.g. joint angle and the position of body segments, to evaluate the quality of the performance and provide real-time feedback to the user [90].

Recent advances of microtechnology in the design of miniaturized lightweight sensors and embedded systems enable the integration of motion sensing systems into clothing. This ensures a stable sensor placement and thus the reliability of the measurements and above all comfort for the user. However, there are still some challenges in developing a robust and low-cost multi-sensor wearable motion tracker [21].

The aim of this thesis is to present the design and development of a wearable multi-sensor system that is affordable for all types of users and can be used for a long time for the application of exercise monitoring. In order to obtain more accurate results when the target is a variety of users with different body shapes and sizes, a novel body-IMU calibration is also proposed. The result of this calibration approach serves as an observation model for an EKF, which is designed to accurately estimate the positions of the leg segments and the joint angles. Finally, an approach is proposed based on an online template matching method for exercise identification. This approach is evaluated in terms of accuracy and execution time, taking into account different types of motion signals.

This offers a complete wearable platform to monitor lower body strength exercises in real-time and to provide feedback on the quality of the user's performance.

## 1.1. Motivation

### 1.1.1. Monitoring of strength exercises

Strength is the ability of a muscle or a group of muscles with the same functional role in producing force, which is critical for athletic performance, as well as for activities of daily living [66]. The assessment of this quantity helps physicians and therapists plan programs to maintain and develop strength [44].

Musculoskeletal contractions can be classified into concentric, eccentric, and isometric con-

tractions. All these types occur during smooth and coordinated movement of strength exercise. These contractions, which are the result of resistance training, could have an impact on the overall energy expenditure [51]. Although the extent of the effects depends on body composition and body size, a quantitative assessment of the effects in terms of frequency, duration, and intensity could help to predict energy expenditure [18,97].

The results in [1] have shown the increases in maximum muscle strength and fast muscle capacity for both highly trained and untrained groups of individuals. For the elite cyclist in particular, a similar study, but over a longer period of time, demonstrated a relatively higher power output as a result of strength and endurance training compared to pure endurance training. The realized factors for these results are the increased peak torque and its earlier achievement [110].

According to [111], strength training also influences running and cycling endurance performance.

The study in [146] indicates the lower body resistance training, including full squat and split squat, could improve the muscle strength and jumping ability of elite female water polo players. Moreover, there have been several studies on the relationship between exercise and the improvement of cognitive activities and mood, based on analysis of the Brain-derived neurotrophic factor (BDNF). The application of this strategy in patients with dementia, Parkinson's disease, and schizophrenia has been shown to successfully improve on the life skills of these patients [94, 137, 140].

The importance of monitoring such exercises in terms of performance improvement, injury prevention and rehabilitation is assessed here using various examples.

#### **1.1.1.1. Performance improvement**

In a study of the influence of direct monitoring of training on strength performance in [76], the primary results show that the extent and rate of training load increases were more significant for directly monitored compared to unsupervised training. This evaluation was based on the strength performance measurements, e.g. repetition maximum (RM) and body composition, e.g. fat-free mass (FFM), before and after 12 weeks of the training program. They relate these results to the way in which the personal trainers encourage the use and tolerance of the higher training loads, resulting in optimized stimulation of motor units and muscle tissue mass in each session, in addition to psychological factors, in particular, competitiveness i.e., performances for the audience and external motivation.

#### **1.1.1.2. Injury prevention**

The detection of hip joint osteoarthritis based on the range of motion (ROM), is investigated in [60], among former elite long-distance runners, soccer players, weight lifters, and shooters aged 45-68 years. The results showed that apart from a direct correlation between body mass index (BMI) and this disorder, a clear left-right difference in hip rotation only occurs in patients with severe osteoarthritis.

The strength deficits and imbalances in the long head of biceps femoris (LHBF) are the two potential and quantifiable risk factors in hamstring injuries, which are the most common injuries in male professional football players [151]. The rate of hamstring injuries decreases with corrective strength training and retesting of isometric, concentric, and eccentric strength.

According to [55], 50 to 75% of regular runners suffer overload injuries of lower body. The studies in [130] show that the strength exercises while monitoring the ROM could reduce the risk of such injuries. They evaluated the ROM in the frontal and transverse planes, before and after a six-weeks strength exercise training session, in healthy women. The result showed that the increase in muscle strength in hip abductors and external rotators affects the biomechanics of the lower extremities, which reduces the stress on the joints of the lower extremities and the risk of injuries.

A decade-long study [45] of 1401 soccer players from 10 European countries identified 2123 lower extremity injuries in the major muscle groups: adductors, hamstrings, quadriceps, and calf. Of these, the 34% was known as overload injuries, 27% were re-injuries with another identical injury. There are other potential extrinsic risk factors, such as fatigue, match stress, and season planning. However, previous injuries on the same muscle or other muscle groups have been identified as critical risk factors.

The abnormal movement biomechanics of the trunk, hip, and knee, caused by impaired hip strength, could have a strong impact on neuromuscular control and therefore be associated with injuries to the anterior cruciate ligament (ACL). Such anomalies could be used to assess and predict this type of injury [61]. Their treatment after anterior cruciate ligament reconstruction (ACLR) could, in addition to the planning of targeted rehabilitation, significantly reduce the recurrent injuries and resulting functional disabilities [47].

### 1.1.1.3. Rehabilitation

In Alpine skiing, the risk of re-injury of the ACL or the other knee after surgery is high. To achieve the state of return to sports, the athlete should achieve adequate endurance, strength, and eccentric control in the lower extremities. Therefore, three phases of the rehabilitation process are proposed in [65]; advanced functional, sports-specific, and return to the sports phase. Everyone should meet the minimum criteria to move to the next level. The advanced functional phase for restoring muscular strength includes squat exercises from shallow to the skier tuck position and leg press with repetitions to increase endurance. The athlete should maintain the specific joint angles during various stages of the exercises as squats deeper than 60 degrees could increase anterior tibial translation.

Since the sports-specific phase requires the performance of jump landing tasks in order to achieve sufficient stance stability, the minimum criterion for entering this phase is to maintain a symmetrical bilateral squat with 60 degrees of knee flexion for 30 seconds and a one-legged squat of knee flexion for 30 degrees while maintaining optimal knee alignment. More precisely, the reason for controlling the dynamic of the hip joint is the hip's tendency to adduction and

internal rotation during flexion. This was observed during weight-bearing in intense activities such as running or landing from a jump [100].

### **1.1.2. System for monitoring strength exercises**

The previous section discussed the benefits of monitoring strength exercise in terms of performance improvement, injury prevention, and rehabilitation. This section describes how such services are provided using a system for monitoring the strength exercises.

As has been described, performance improvement is achieved by monitoring the strength exercises by measuring RM, which can be achieved by consistently indicating the number of repetitions during the exercise. Therefore, a system is needed that tracks the movements precisely and recognizes the correctly performed exercises. The exercise identification process, which is based on a precise tracking of lower body movements, provides the repetition numbers that can later be used to evaluate user performance in relation to RM. Moreover, external motivation to improve the performance can be achieved by receiving visual feedback from the monitoring system of the identified phases of the exercise.

By consistently estimating the joint angles of the lower extremities, such a system provides a reliable measure of ROM, which is the most important factor in the detection and prevention of injuries. Furthermore, the quantification of the imbalances can be achieved by such a platform, which additionally provides a precise estimation of the leg segment positions.

According to the previous section, the knee joint angle is used to identify each stage of the rehabilitation process. Moreover, the symmetrical execution of the strength exercise can be recognized as a factor in the progress of rehabilitation by tracking the leg segment positions. In addition to the knee joint angle, the 3D estimation of the hip joint angle helps to control the dynamics by detecting abduction and internal rotation during flexion.

In rehabilitation clinics, these values are usually measured manually using goniometers. However, this procedure is time-consuming and cumbersome and cannot provide precise measurements in dynamic situations [144]. Moreover, clinicians need to be trained in the correct placement of such devices, and therefore it is imperative that patients go to rehabilitation centers to monitor their progress in recovery.

### **1.1.3. Technology and social factors**

There are a variety of technologies and social factors which drive interest in sports monitoring equipment [77]:

#### **1.1.3.1. The proliferation of smartphones**

”Smartphones will become the sixth sense for the user, gathering information from wireless sensors in the user’s environment and from the network, interpreting the information, and providing valuable feedback to the user.” Joshua J. Romero [112].

Smartphones offer a combination of built-in sensor units, software platform, touchscreen dis-



play, and wireless connectivity (e.g. Bluetooth and Wi-Fi) for the development of basic fitness monitoring.

### 1.1.3.2. Wearable technologies and e-textiles

Recently, wearable technologies have become more popular and more accessible than before due to lower prices. The miniaturization of their components and advances in e-textiles have made it possible to integrate sensor units into clothing. Therefore, they are now considered to be fashion items, indicating the user's interest in maintaining his or her well-being rather than a sign of illness [31].

### 1.1.3.3. Social networking and gamification

The ability to record and share fitness data on social networks is offered by most sports monitoring devices via the cloud and Internet-enabled technologies. This encourages users to stay motivated and set new goals by competing with family and friends [113].

Moreover, gamification in the form of individual interaction [5] or social competition [36] leads to increasing encouragement to keep up with physical activity.

## 1.2. Problem Formulation

Wearable systems offer not only professional athletes, but also ordinary people who are willing to lead a healthy life and motivated to stay in training, the opportunity for self-reflection.

IMU-based motion detection systems are the area of interest for most fitness applications, unlike traditional technologies such as optical and mechanical trackers [147], [4]. The main reason for this is that they can work in a self-contained manner (independent of external hardware). They are also unobtrusive, comparably inexpensive, and easy to set up and use.

Most of the existing products have only one sensing unit [121]. They therefore only provide biometric information and not biomechanical details of movements. As described above, a strength exercise monitoring system should provide such detailed information, including joint angles and body segment positions. However, products with more sensing units are not easy to use for daily training due to complications in placement and high prices [142], [153].

Moreover, a wearable system should be able to function autonomously over long periods of time in different training situations. These requirements lead to many challenges when designing such a system. For instance, to accurately estimate joint movements, several sensing units should be placed on the body and connected to a control unit for data acquisition and processing. This increases the total weight and power consumption, which consequently reduces user comfort and the system operational lifetime. Furthermore, the complexity and dimensions of the sensing units and their connections can have a negative effect on system cost and aesthetics and thus on user acceptance.

The first step in using the motion tracking suit is to calibrate the IMUs, especially the magnetometer, which can easily be influenced by ferromagnetic materials in its vicinity.

Moreover, knowing how each IMU is attached to each body segment when the user wears the textile is critical to providing the biomechanical details of the movement. The use of assumptions and information from anthropometric tables could lead to inaccurate tracking because there are different types of target persons with different body shapes. In addition, there are different types of clothing material used for the design of the wearables, which result in different sensor placements, even for a specific person. Manual measurements of these parameters are also cumbersome and error prone. Therefore, an accurate, robust, and autonomous sensor-body calibration method is required for a wearable training suit.

Although the use of low-cost, lightweight IMUs in the wearable system increases user acceptance, the inherent noise and unstable bias of their measurements, even when well-calibrated, lead to high error due to drift. It is therefore necessary to minimize this error by fusing and filtering the measurements in order to obtain higher-level information, i.e. joint angles and segment positions. These parameters are necessary to quantify the critical factors for the monitoring of strength exercises such as ROM, imbalances, or symmetrical performance.

To obtain RM, a real-time exercise identification process is also required to determine the number of correct repetitions during the exercise.

### 1.3. Contributions

The contributions of this work are the following:

- Design and development of a low-cost motion tracking system, including a network of wired microelectromechanical systems (MEMS) IMUs that fits into a suit for the feasible detection of human body motions. Using miniaturized IMUs and textile cables, the system is designed to be light-weight and easy to use, providing maximal movement flexibility for the user. A customized firmware with a novel cascaded approach to data acquisition and a power-management process extends the autonomous operating time compared to conventional approaches. Power consumption and data quality are evaluated in different experiments that show the potential use of the proposed platform in personal training scenarios. These are described for two different system configurations in the following conference papers [117], [118]:

Sarvenaz Salehi, Gabriele Bleser, Norbert Schmitz, and Didier Stricker. A low-cost and light-weight motion tracking suit.

In 10th International Conference on Ubiquitous Intelligence and Computing (UIC) (2013), pp. 474-479. 16

Sarvenaz Salehi, Gabriele Bleser, and Didier Stricker. Design and development of low-cost smart training pants (stants).

In 4th International Conference on Wireless Mobile Communication and Healthcare, At Athen, Greece (2014), IEEE, pp. 39-44. 15, 16, 28, 65

- A practical method for in-field magnetometer calibration and alignment with inertial sensors, in an IMU. The procedure is attitude independent and works without the need for

precise equipment or external heading information.

In the first step, bias, scale factors, and non-orthogonality parameters are estimated based on magnitude information and data collected under motion. In the second step, misalignment parameters are determined from the inclination using the gravity measured by accelerometers under static conditions. In each step, an initial guess established based on linear least squares, followed by a non-linear optimization, leads to a reliable estimate of all calibration parameters.

Different performance aspects of the method are evaluated in several tests with real data. This approach and its results are described in the following conference paper [119]:

Sarvenaz Salehi, Navid Mostofi, and Gabriele Bleser. A practical in-field magnetometer calibration method for imus.

In Proceedings of the IROS Workshop on Cognitive Assistive Systems: Closing the Action-Perception Loop (2012), pp. 39-44.

- A new body-IMU autocalibration method developed specifically for the lower body. First, an observability analysis of an existing position calibration method is presented, which shows its limited applicability for the hip and knee joints. On this basis, a method is proposed to simultaneously estimate the positions of three IMUs (mounted on the pelvis, upper leg, and lower leg) relative to those joints. In addition, new constraints are proposed to improve the estimation. An experimental evaluation based on simulated and real data shows an improvement in terms of accuracy and robustness compared to a previous method, especially when it comes to suboptimal (low-variation) movements during calibration. This method and part of the results are presented in the following conference paper:

Sarvenaz Salehi, Gabriele Bleser, Attila Reiss, and Didier Stricker. Body-imu autocalibration for inertial hip and knee joint tracking.

In Proceedings of the 10th EAI International Conference on Body Area Networks, BodyNets15, ICST (Institute for Computer Sciences, Social-Informatics and Telecommunications Engineering), pp. 51-57. 16

- Two approaches for real-time lower body pose estimation. The first approach estimates the orientation of pelvis, which is considered as the body reference. The second approach estimates the leg pose, ie the hip and knee joint angles and position of the IMUs, which are mounted on the leg segments. The latter can be interpreted as the position of leg segments.

The proposed orientation estimator is based on an EKF with an extended state vector, containing the angular acceleration and magnetic disturbance offset. This leads to better results in compared to a conventional orientation estimator.

The leg pose estimation approach is also based on an EKF, where only inertial measurements contribute as control inputs in the filter. In the proposed approach, the joints' constraints are incorporated as observation models. This algorithm assumes that the joint

axes and the positions in relation to the IMUs are known. These values are achieved by the body-IMU calibration algorithm. The evaluation of this approach shows promising results.

- An efficient online template matching approach for exercise identification, which provides real-time user feedback by counting the correctly performed exercises. By utilizing the motion primitives detection and the feature extraction concepts, this method reduces execution time while maintaining the accuracy. Moreover, the identification process is verified in comparison to the related works, using different types of motion signals, i.e. hip and knee joint angles and the leg segments' positions for the squat exercises.

The result of the last three contributions is published in the following conference paper [120] and article:

Sarvenaz Salehi and Didier Stricker. Validation of a low-cost inertial exercise tracker. In Proceedings of SENSORNETS 2020

Sarvenaz Salehi, Didier Stricker. Strength exercise monitoring with inertial sensors. Submitted in Communications in Computer and Information Science book series (CCIS), Springer

## 1.4. Organization of the thesis

This thesis is organized in the following way:

**Chapter 2 Background and Related Work** presents the background and the related works of IMU calibration and more specifically, the magnetometer calibration, body-IMU calibration, orientation and body pose estimation and exercise identification.

**Chapter 3 System Design** provides an overview of the related products and scientific projects in motion capturing technologies and wearable motion monitoring systems. Moreover it describes the system design of a low-cost and energy efficient IMU-based suit. The design approach is presented in three divisions: the hardware, including the sensing and controller units, the firmware including a novel cascaded approach for data acquisition and a power management process, and the software platform for development of exercise monitoring applications. Moreover, the system was evaluated in terms of power consumption, weight and cost, and measurement quality, in comparison to the other similar available systems.

**Chapter 4 System Calibration** is dedicated to the calibration procedure required before using the motion tracking suit. The first stage is IMU calibration, including a practical and in-field magnetometer calibration. The second stage is body-IMU calibration for extracting the IMU positions with respect to the joints. Here, an observability analysis of an existing method is presented. Based on that, new constraints are proposed to improve the estimation. This approach is extensively evaluated with different types of movements using synthetic and real data.

**Chapter 5 Lower Body Motion Tracking** explains two real-time motion tracking approaches based on EKF, which are used to estimate the lower body pose, during the strength exercises. The first is pelvis orientation estimation, and the second is leg pose estimation. The latter provides the positions of leg segments and knee and hip joint angles. This is followed by an evaluation of lower body pose estimation for squat and abd/adduction exercise.

**Chapter 6 Exercise Monitoring** addresses the exercise identification, using an online template matching algorithms. Moreover, solutions are proposed to reduce execution time while maintaining the accuracy. This approach is evaluated and compared to the related works using motion signals, i.e. joint angles and the leg segment positions for squat exercise identification .

**Chapter 7 Conclusion** summarizes the thesis and gives suggestions for future work.



## 2. Background and Related Work

This chapter presents a background for the key concepts for calibration, body motion tracking and exercise identification, as well as an overview of the existing algorithms. Section 2.1 describes the IMU calibration. The focus is on the related work of magnetometer calibration as it presents greater challenges in motion estimation compared to the inertial sensors. An introduction to the movements of the joints of the lower body is presented in Section 2.2. The studies and estimation theory related to body-IMU calibration are discussed in Section 2.3. Section 2.4 describes the filtering techniques and related research on orientation and lower body motion estimation. Finally, Section 2.5 introduces the related concepts of data mining in time series, followed by related work on exercise identification.

### 2.1. IMU Calibration

In an IMU, the inertial sensors, including accelerometer and gyroscope, are integrated with an aiding sensor. One of the most commonly used aiding sensors is magnetometer. Given a valid calibration, IMUs can provide accurate orientation in three dimensions. While gyroscopes measure angular velocities, accelerometers, under moderate body accelerations, provide a vertical reference, and the Earth's magnetic field vector measured by magnetometers is a useful reference in the horizontal plane. Ferraris *et al.* proposed in [35] a practical method for the calibration of inertial sensors, where the bias, scale factors and mounting misalignment of these sensors with respect to the IMU case coordinates are obtained using two sets of static and rotating IMU measurements. This method is used in this thesis.

In contrast to inertial sensors, magnetometer measurements are easily disturbed by ferromagnetic materials i.e., hard/soft iron [7] in the vicinity of the sensor, either inside the IMU casing or in the final mounting position. As a result, parameters such as biases, scale factors, non-orthogonality of the axes, and misalignment of the magnetometer coordinate frame with the one of inertial sensors, which is normally pre-calibrated by the manufacturer, are rendered invalid after installation at the customer's site. This can significantly degrade tracking performance. To compensate for such errors, a specific in-field calibration for magnetometers is required. It should be mentioned that this work covers the time-invariant disturbances, that move with the sensor frame while external effects caused by hard/soft iron materials outside the IMU coordinate frame need to be handled online, e.g. either by adapting the calibration parameters or by discarding the corresponding measurements [109, 114].

Various methods for magnetometer calibration have been proposed in the literature. The use of precise external references such as Helmholtz coils for magnetometer calibration [133] is expensive and may not be practical for all types of applications. Other proposed methods use the Earth's magnetic field, sometimes in combination with attitude information. Swing is a tra-

ditional attitude-dependent method that requires a number of known headings in the horizontal plane [16]. A simpler approach is to use only information about the Earth's magnetic field, such as field magnitude (scalar checking) or inclination. Using field magnitude, an ellipsoid fitting approach is proposed in [106], which is, however, based on minimizing algebraic distances and leads to a suboptimal estimation of the calibration parameters.

Vasconcelos *et al.* [145] suggest a geometric approach to obtain an optimal estimate of the calibration parameters using a maximum likelihood estimator (MLE). However, the method turns out to be sensitive with regard to a perturbed initial guess, where the latter is not uncommon when working with real data. There is also a solution for the alignment problem proposed, which requires external information sources. In [2], Alonso and Shuster present a complete calibration procedure based on scalar checking and a so-called centering approach. Although misalignment is proven to be unobservable from the magnitude, the proposed work lacks a solution for correcting such. Besides the field intensity, another bit of information concerning the Earth's magnetic field is its inclination, which can be obtained from the gravity measured by accelerometers under static conditions.

Hu *et al.* [50] use an ellipsoid fitting method for bias estimation, and a solution based on the inclination obtained from accelerometer measurements is provided to estimate the remaining calibration parameters in one coefficient matrix. However, the accuracy of this method depends on the location on Earth. At the equator, where magnetic field vector and gravity are orthogonal, the scale factors are unobservable, and their estimation deteriorates as we approach the equator. Furthermore, additional noise and errors caused by the use of accelerometer data acquired under motion lead to a degraded estimate of the respective parameters.

### 2.1.1. Parameter estimation: Data fitting

In the estimation theory, parameter estimation techniques deal with the estimation of values that do not change over time, e.g. the calibration parameters described in the previous section. In such techniques, the measurement vector  $\vec{z}$  is modeled as:

$$\vec{z} = h(\vec{x}) + \vec{v} \quad (2.1)$$

, where  $\vec{x}$  is the parameter vector, and  $\vec{v}$  is both measurement noise and unknown modelling errors. For data fitting an estimate of  $x$ ,  $\hat{x}$ , minimizes the sum over the squared norm of residuals as defined in the following:

$$\operatorname{argmin}_{\vec{x}} \|\vec{z} - h(\vec{x})\| \quad (2.2)$$

Assuming the Euclidean norm, this can be solved by using least-squares estimation. For a nonlinear measurement model as for the problem of calibration parameters, a numerical solution can be achieved by a nonlinear optimization method like Gauss-Newton. In this method,  $\vec{v}$  is assumed to be a zero-mean Gaussian process.  $h(\vec{x})$  is linearized using the Taylor expansion. Starting with some initial guess,  $\hat{x}_0$ , an estimation of the parameter vector is obtained through an iterative procedure as follows:



$$\hat{x}_{k+1} = \hat{x}_k + (H^T(k)H(k))^{-1}H(k)(z - h(\hat{x}(k))) \quad (2.3a)$$

$$H(k) = \left. \frac{\partial h(x)}{\partial x} \right|_{x=\hat{x}(k)} \quad (2.3b)$$

, where  $H(k)$  is the Jacobian matrix of the measurement model with respect to the parameters and is realized in the current estimate. This process is successful if the initial guess is close to the global minimum, otherwise, it results in a local minimum or divergence. This problem is addressed in this work using the linear least-squares approximation  $h$  to find an initial guess.

## 2.2. Lower Body Movements

Here the focus is on three important components involved in the movements of the lower body: hip and knee joints and pelvic bone.

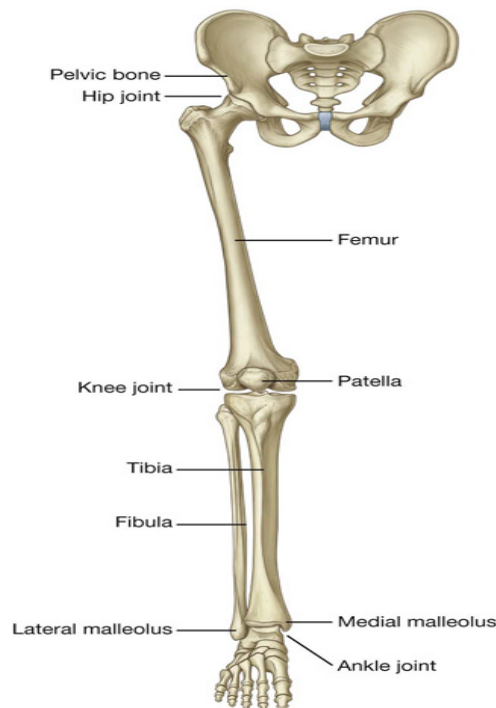


Figure 2.1.: Joints and bone segments in lower body [10]

### 2.2.1. Hip joint

The articulation between the pelvis and the femoral head is the hip joint, Figure 2.1, which can be interpreted as a ball and socket joint. The movements take place around three mutually perpendicular axes: flexion and extension around a transverse axis, internal and external rotations

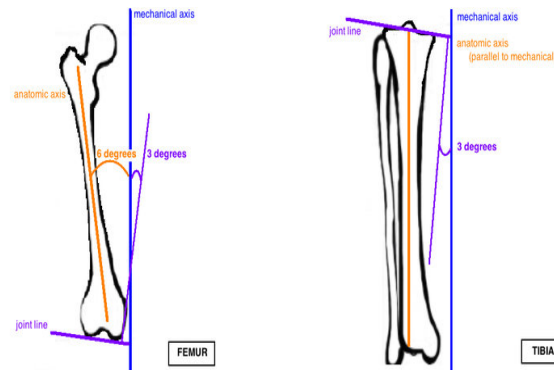


Figure 2.2.: Natural misalignment of the knee joint axis with mechanical and anatomical axis of lower body [48]

(medial and lateral) around a longitudinal axis, abduction, and adduction around the sagittal axis, see Figure 2.3.

### 2.2.2. Knee joint

The articulation between patella, femur, and tibia is the knee joint, Figure 2.1, which can form a hinge joint since it mainly allows flexion and extension rotation around the knee joint axis (joint line), which in a native knee, has a misalignment of 3 degrees with respect to transverse axis of the body [24], see Figure 2.2. The joint axis during the flexion/extension movement of the knee simultaneously exhibits internal/external rotations. More precisely, in an open chain kinetic, the tibia rotates externally during knee extension, and in a closed kinetic chain femur rotates internally during knee flexion. Therefore, due to these movements and natural misalignment, the expected estimate of rotation axis based on the measurements of the sensors attached to the adjacent segments is a vector that is not parallel to the hip joint flexion/extension axis. This fact was taken into account when defining a new geometrical joint constraint for the body-IMU calibration in Chapter 4.

### 2.2.3. Pelvic bone

The pelvis can move relative to the thigh at the hip joint and relative to the trunk at the lumbosacral joint. The movements relative to the hip joint are the reverse of the standard thigh movements since the same muscle group is involved in such movements, see Figure 2.3. As a result, simultaneous rotation of pelvis and thigh in different directions can be difficult. This leads to suboptimal movements for the body-IMU calibration process as elaborated in the observability analysis in Chapter 4.

## 2.3. Body-IMU Calibration

Body-IMU calibration is a key requirement for capturing accurate body movements in applications based on wearable systems [105,155]. The mounting positions of IMU in relation to joints

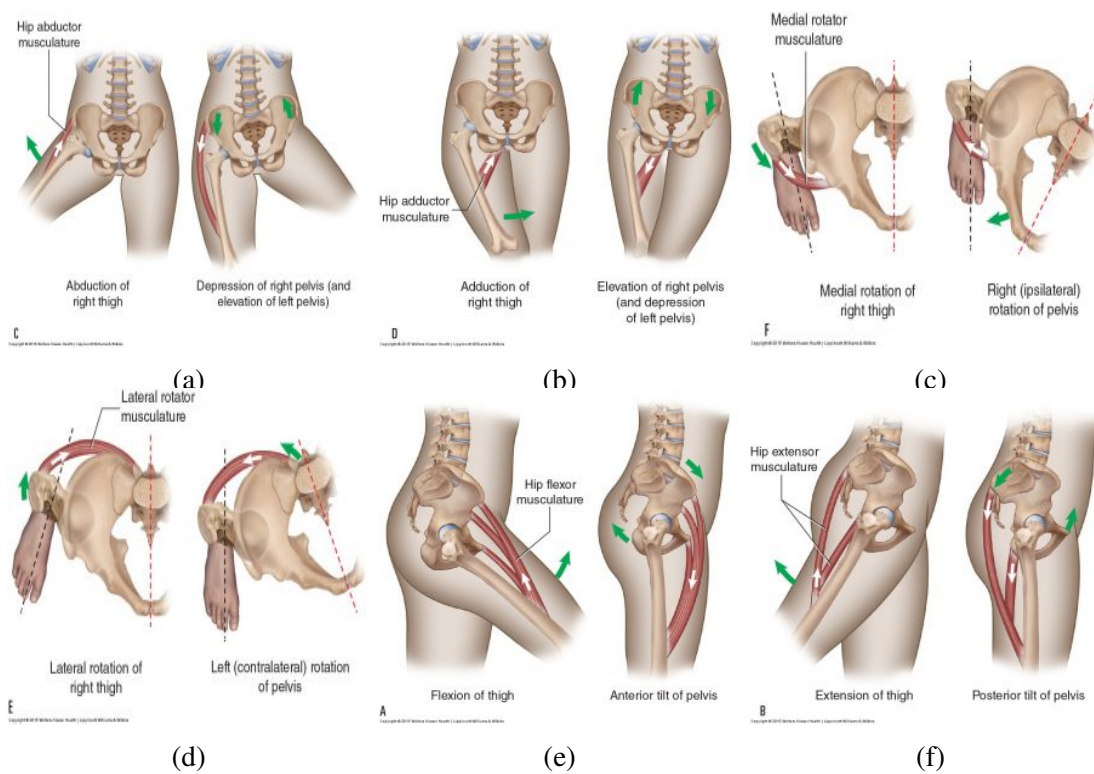


Figure 2.3.: Pelvis and thigh reverse movements with the same muscle group [88]: (a) Hip abductor muscles (b) Hip adductor muscles (c) Medial rotator muscles (d) Lateral rotator muscles (e) Hip flexor muscles (f) Hip extensor muscles

are critical information in joint angle estimation using accelerometer measurements, especially during fast rotations [22] and when modeling kinematic chains [80]. The use of assumptions and information from anthropometric tables could lead to inaccurate tracking because there are different types of target users with different body shapes. In addition, there are various types of clothing materials used in the design of the wearables that result in varying sensor placements, even for one individual. Manual measurements of these parameters are also cumbersome and error-prone. Therefore, an accurate, robust, and autonomous sensor-body calibration method is required for a wearable training suit.

In order to compensate for the resulting errors, [93] uses a rotational mapping based on the integration of gyroscope measurements. Thus, the tracking accuracy of the joint angle is limited to time due to drift. In [65] and [71], the IMU positions are used during tracking. However, these parameters are determined by manual measurements, which is not accurate. In [156], a method based on Kalman filters to minimize the position errors is proposed. However, this method requires multiple IMUs on each segment with controlled positional errors in relation to each other. Furthermore, the large state vector, required for this method is not efficient, considering the computational power available in mobile applications. The derivation of an efficient, robust, and precise method based on a practical procedure is a crucial as well as a challenging task when developing a wearable system with multiple embedded IMUs. Here the related work, based on the condition of acquiring the measurements, is examined in three different groups of methods: static, functional, and autocalibration.

### 2.3.1. Static

This type of calibration is also known as single or double pose calibration, where the subject should hold one or two known poses. The measurements during these poses are compared with the expected measurements, and an alignment rotation is estimated. This estimated rotation is used during tracking of body movements to align the measurements with the segments. In [122], a T-pose is introduced, in which the subject stands upright and holds the arms horizontally to the side, see Figure 2.4.

In [12], a simple and easy-to-perform calibration procedure was developed, which is based on two static poses, Figure 2.5; For the upper body, the IMU mounted on the torso is calibrated first. The orientation of this IMU is determined by means of two accelerometer measurements from standing in the reference pose and bending forward, respectively. The direction of the body  $z$  axis in IMU is obtained from the first measurement, i.e. the gravity. The  $x$  is calculated by the cross product of the two measurements since the bending is around  $x$  body axis. The  $y$  axis then is the cross product of  $z$  and  $x$  direction to obtain a right-handed coordinate system. For the IMUs on arms, the  $z$  directions are determined from accelerometer measurements at the nominal pose, and their  $x$  and  $y$  axes by comparing their magnetometer measurements those on the torso.

Palermo *et al.* [96] propose a similar approach for the lower body with two static poses: standing and sitting/lying with the legs stretched out. The problem with such methods is that the joint axes, as well as the IMU positions, cannot be identified.

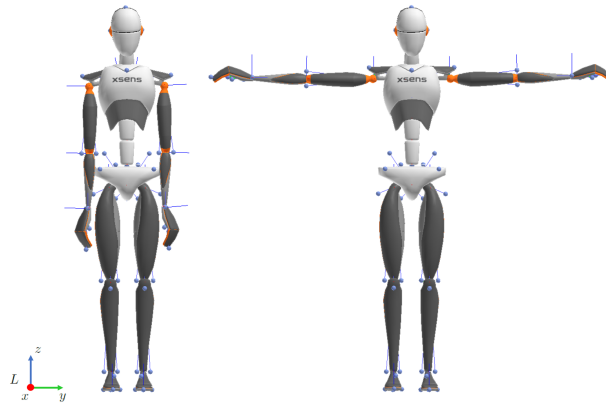


Figure 2.4.: Body IMU calibration for upper body based on two static poses

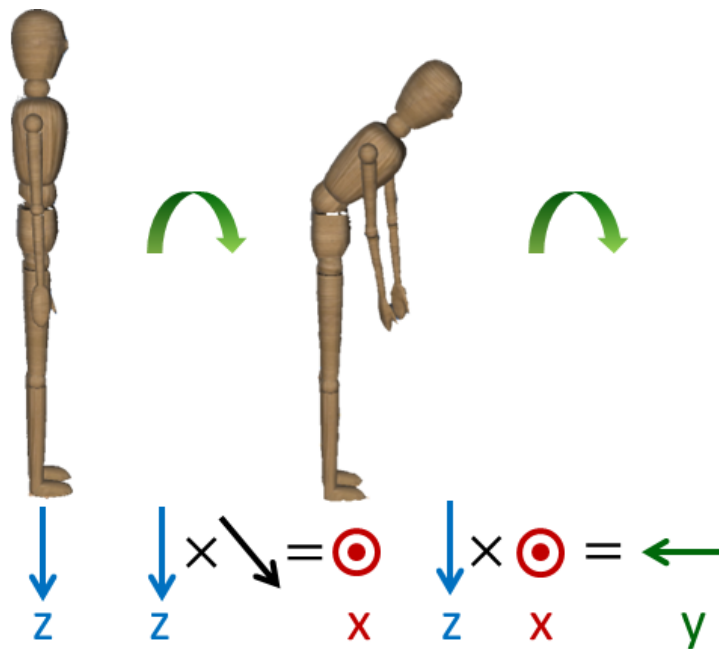


Figure 2.5.: Body IMU calibration based on two static poses

### 2.3.2. Functional

In [34], [93], two functional calibration procedures are proposed, to obtain joint axes of the lower body based on a fusion of the measurements of each IMU. The estimated joint axes are then used to track the joint angles in a reliable and clinically interpretable way. However, these procedures require passive and precisely controlled movements that are difficult to perform without supervision.

Moreover, none of the above-mentioned contributions provides a method for estimating the sensor positions with respect to the adjacent joints.

### 2.3.3. Autocalibration

In order to enable a ubiquitous fitness tracking, a calibration method should be performed by subject autonomously and without supervision or the need to use additional tools. In [123], Seel *et al.* propose a novel and practical method for estimating the joint axis of a hinge joint and the IMU positions with respect to a spheroidal joint, based on the gyroscope and accelerometer measurements of two IMUs mounted on adjacent segments. In [124], the applicability of these methods is discussed for the examination of joints with different degree of freedom (DOF), and simple extensions are presented. In [123, 124], the method is applied to the knee and ankle joints, while in [90], it is adopted for a home-based clinical knee rehabilitation system. The methods of Seel *et al.* work without the need for dedicated calibration movements. However, it did not provide an analysis of the types of movement that lead to the most accurate results. If there are insufficient variations in the different DOFs, the position calibration method will lead to inaccurate results. This was shown when applying the method to the hip joint, where it is difficult to perform movements with sufficient variation.

The proposed IMU position estimation method in this thesis builds upon the method presented in [123, 124], considering to improve its accuracy and robustness under suboptimal movement conditions and making it applicable to the body-IMU calibration for the designed IMU-based exercise tracker focusing on the hip and knee joints.

#### 2.3.3.1. Bayesian parameter estimation

In Bayesian approach the parameters are assumed to be the random values, derived from the probability distribution,  $P(x)$ , and the aim is to find an estimate,  $\hat{x}$  that is most probable given the measurements. This is called maximum a posteriori (MAP), which is calculated according to the Bayes rule as follows:

$$\hat{x}_{MAP} = \arg \max_x P(z|x)P(x) \quad (2.4)$$

, where  $P(x|z)$  is the conditional probability distribution of some measurements given the parameters. Since the peak of this probability is often in an area of  $x$  with constant probability, in Equation 2.4,  $P(x)$  can be discarded. This gives the MLE:

$$\hat{x}_{MLE} = \arg \max_x P(z|x) \quad (2.5)$$

This is particularly useful when there is little prior knowledge available. Similar to the data fitting, the Gaussian measurement model is assumed, and  $P(z|x)$  is defined by a normal distribution. Therefore, the MLE can be solved using the least-squares estimation(LSE) techniques. In this work, this approach is applied in the body-IMU calibration process.

### 2.3.3.2. Observability analysis

A system is observable when the amount of information contained in the measurements is sufficient for parameter estimation. This can be evaluated by estimating a lower limit of the measurement model noise, i.e. variance of  $v$  in 2.1. This is known as Cramer-Rao Lower Bound(CRLB). Assuming the estimator 2.5 is unbiased:

$$E[\hat{x} - x] = \int (\hat{x} - x)P(z|x)dz = 0 \quad (2.6)$$

Then from derivative of 2.6 with the assumption of the integrability of the derivative of an integrand:

$$\frac{\partial}{\partial x} \int (\hat{x} - x)P(z|x)dz = \frac{\partial}{\partial x} 0 \quad (2.7a)$$

$$\int \frac{\partial}{\partial x} ((\hat{x} - x)P(z|x))dz = 0 \quad (2.7b)$$

$$\int -P(z|x) + (\hat{x} - x)\frac{\partial}{\partial x} P(z|x)dz = 0 \quad (2.7c)$$

The derivative of probability can be calculated using the natural logarithm:

$$\frac{\partial \ln y}{\partial x} = \frac{1}{y} \frac{\partial y}{\partial x} \Rightarrow \frac{\partial P(z|x)}{\partial x} = P(z|x) \frac{\partial \ln P(z|x)}{\partial x} \quad (2.8)$$

knowing that  $\int P(z|x)dz = 1$ , Equation 2.7c is rewritten to:

$$\int (\hat{x} - x)P(z|x) \frac{\partial \ln P(z|x)}{\partial x} dz = 1 \quad (2.9)$$

To derive the estimator variance, Equation 2.9 is modified to:

$$\left( \int ((\hat{x} - x)\sqrt{P(z|x)}) \left( \sqrt{P(z|x)} \frac{\partial \ln P(z|x)}{\partial x} \right) dz \right)^2 = 1 \quad (2.10)$$

, which, according to Cauchy-Schwarz [134] can be formed in the following inequality:

$$\int ((\hat{x} - x)\sqrt{P(z|x)})^2 dz \cdot \int \left( \sqrt{P(z|x)} \frac{\partial \ln P(z|x)}{\partial x} \right)^2 dz \geq 1 \quad (2.11)$$

, which is equivalent to:

$$E[(\hat{x} - x)^2] \geq E\left[\left(\frac{\partial \ln P(z|x)}{\partial x}\right)^2\right]^{-1} \quad (2.12)$$

, where  $E[\cdot]$  is the expected value. The left side of this inequality is the variance of the estimated parameter, and the right side is the inverse of the Fisher information matrix (FIM). Therefore, for variance to be bounded the FIM matrix should be invertible. In other words, the system is observable when the corresponding FIM is full rank. Note that if  $FIM = 0$ , the variance is infinite, i.e. nothing known about the parameters. This criterion is used to detect the suboptimal movements for body-IMU calibration. As in [148] with the assumption of Gaussian model in 2.1, the FIM can be simplified as follows:

$$\frac{\partial \ln P(z|x)}{\partial x} = \frac{\partial}{\partial x} \ln \left[ c \exp\left(\frac{-1}{2}(v^T \Sigma_z^{-1} v)\right) \right] = \frac{\partial}{\partial x} \left( \ln c - \frac{v^T \Sigma_z^{-1} v}{2} \right) = H^T \Sigma_z^{-1} v \quad (2.13)$$

Substituting into FIM in 2.12:

$$FIM = E\left[(H^T \Sigma_z^{-1} v)(H^T \Sigma_z^{-1} v)^T\right] \quad (2.14a)$$

$$= E\left[H^T \Sigma_z^{-1} v v^T (\Sigma_z^{-1})^T H\right] \quad (2.14b)$$

$$= H^T \Sigma_z^{-1} E[v v^T] (\Sigma_z^{-1})^T H \quad (2.14c)$$

$$= H^T \Sigma_z^{-1} \Sigma_z (\Sigma_z^{-1})^T H \quad (2.14d)$$

$$= H^T \Sigma_z^{-1} H \quad (2.14e)$$

## 2.4. Body Motion Tracking

One of the most commonly used techniques for sensor fusion and motion estimation is Kalman filtering. Therefore, this section starts with an introduction to this technique.

### 2.4.1. Kalman filter

The Kalman filter [54] is a linear estimator that uses the statistical model of states, known as the process model, and the statistical model of the relation between states and observations, known as the measurement model. In a recursive approach, the Kalman filter estimates the state of a process by minimizing mean squared error. This is achieved by two groups of linear difference equations:

- Time update or prediction equations, where the current estimate and error covariance are propagated in time, resulting in an a priori estimate.
- Measurement update or correction, where the predicted state estimate is improved according to new measurements, therefore results in a posteriori estimate.



Since the motion process and measurement models are mainly nonlinear, an extended version of the Kalman filter, EKF, is commonly used.

### 2.4.2. Extended Kalman filter

The EKF [53] is based on the linearization of all the nonlinear models around the currently estimated states. For a system with the states  $x_k$  and the measurements  $z_k$ , time update and measurement update stages in an EKF are presented in Equations (2.15) and (2.17).

$$x_k = f(x_{k-1}, u_{k-1}, w_{k-1}) \quad (2.15a)$$

$$z_k = h(x_k, v_k) \quad (2.15b)$$

, where  $u_{k-1}$  is the control input.  $w_{k-1}$  and  $v_k$  are process and measurement noises each with covariances of  $Q_{k-1}$  and  $R_k$ . They are assumed to be zero-mean Gaussian noises and independent from each other.

$$\hat{x}_k^- = f(\hat{x}_{k-1}, u_{k-1}) \quad (2.16a)$$

$$P_k^- = F_k P_{k-1} F_k^T + W_k Q_{k-1} W_k^T \quad (2.16b)$$

with

$$F_k = \frac{\partial f}{\partial x} \Big|_{\hat{x}_{k-1}, u_{k-1}} \quad (2.16c)$$

$$W_k = \frac{\partial f}{\partial w} \Big|_{\hat{x}_{k-1}, u_{k-1}} \quad (2.16d)$$

Here, the superscript minus signifies a priori estimate.

$$K_k = P_k^- H_k^T (H_k P_k^- H_k^T + V_k R_k V_k^T)^{-1} \quad (2.17a)$$

$$\hat{x}_k = \hat{x}_k^- + K_k (z_k - h(\hat{x}_k^-)) \quad (2.17b)$$

$$P_k = (I - K_k H_k) P_k^- \quad (2.17c)$$

with

$$H_k = \frac{\partial h}{\partial x} \Big|_{\hat{x}_k^-} \quad (2.17d)$$

$$V_k = \frac{\partial h}{\partial v} \Big|_{\hat{x}_k^-} \quad (2.17e)$$

, where  $\hat{x}_k$  is an a posteriori estimate of the state, and  $K_k$  is the filter gain, which is a weighting factor for the actual versus predicted measurements ( $h(\hat{x}_k^-)$ ).

### 2.4.3. Orientation estimation

In the literature, there are many methods for real-time orientation tracking using IMU measurements. Of all of them, those based on recursive approaches and especially Kalman filtering have shown more promising results [62]. Here, the focus is on methods for orientation estimation in body motion tracking applications.

In [71], a complementary Kalman filter is designed to estimate the angular velocity offset and orientation error in states based on accelerometer and gyroscope measurements. However, the integration of angular velocity and the exclusive use of accelerometer measurements to estimate the offset leads to a drift in the horizontal plane.

Marins et al. proposed an EKF-based approach using inertial and magnetic sensors [74]. The states contain quaternions to represent the orientation (Appendix C), which is a computationally more efficient solution compared to the Euler angles used in [71] and does not suffer from singularity [19]. They applied an iterative Gauss-Newton algorithm to obtain a linear observation model by estimating quaternions from accelerometer and magnetometer measurements. This reduces the computation, but at the same time increases the uncertainty of the noise of the quaternion measurement model.

The problem of uncertainty in the assumption of constant measurement noise can lead to a non-robust estimate during the whole tracking because the measurements contain outliers. For example, the accelerometer measurements for dynamic body movements contain not only gravity but also high accelerations from the movement. Furthermore, magnetometers in the vicinity of ferromagnetic materials or other magnetic fields lead to distorted measurements [7]. Therefore, Sabatini proposed in [114] an adaptive approach to scale the measurement noise when the outliers are detected. Outlier detection is performed by comparing the vector norm with the known reference values. For magnetometers, the reference value of the local dip angle is also taken into account. Since the uncertainty of the magnetic disturbances is high, a more robust approach is to estimate them as a random process. In [109], the estimation error is obtained as a first-order Markov process in a complementary Kalman filter. The process noise is adapted based on the deviation of the magnetic measurements from the reference vector norm and the dip angle. Another approach in [115] introduced a variable state dimension extended Kalman filter (VSD-EKF), in which the filter switches between two different models of magnetic disturbances. These disturbances are detected on the basis of a fading memory average of normalized innovation and two upper and lower crossing thresholds. For the disturbances below the lower threshold, the filter switches to a quiescent EKF with disturbances modeled as first-order Gauss Markov (GM) process (GM-1). If they are higher than the upper threshold, the filter switches to high-order EKF, where the disturbances are modeled as a second-order GM (GM-2). In this thesis, the magnetic disturbances are assumed to be small and change slowly; therefore, they are modeled as a GM-1, similar to a quiescent EKF in [115].

### 2.4.4. Lower Body Pose Estimation

In all related work in this section, it is assumed that the leg segments are rigid bodies that are connected to each other at the knee, hip, and ankle joints. To track the movement, at least one IMU is mounted on each segment.

In [154], the orientation from accelerometer and magnetometer measurements is estimated with the help of axis-angle representation. A linear Kalman filter is used to smoothen these measurements and fuse them with the gyroscope measurements. The linear acceleration error caused by placing the sensor far from the center of the joint is not considered in this approach. Furthermore, the magnetic disturbances are not modeled. It therefore leads to the wrong estimation in the vicinity of ferromagnetic materials.

To account for the error of linear acceleration, the idea of using physical and virtual sensors, based on Newton-Euler equations for estimating the joint angle, is presented in [27, 28]. According to these methods, the joint acceleration can be measured by placing a pair of virtual sensors on the adjacent links on the center of the joint. In these approaches, a joint angle is defined by the directional difference in the measured acceleration of sensors in the joint coordinate frame. In [23], Cheng et al. provide an overview that compares four different methods for measuring the joint angle in two dimensions. They demonstrated that when the sensors are mounted far from the center of the joint, especially for fast rotations, a method called Common Model Rejection with Gyro Differentiation (CMRGD) achieves less error and is easier to implement compared to the other methods. In this method, the gyroscope measurements are numerically differentiated to derive the angular acceleration needed to calculate the joint center acceleration vector.

Instead of using magnetometers, as they can be easily distorted, several studies have applied biomechanical constraints to improve the body motion estimation in the horizontal plane. Such studies can be divided into two categories:

In the first category, the joint angles are estimated in a state estimation approach, based on the known mounting orientations of the IMUs. Then the position of the end effectors of the leg segments is calculated using the forward kinematics and assuming the known segment lengths [67, 105]. In [67], assuming a constant joint acceleration and using the Denavit Hartenberg (DH) convention, the angle is estimated with respect to each possible DOF at hip and knee joints in an EKF. The accelerometer measurement model follows a similar approach in [23] and [28].

In the second category, the state vector contains the relative orientation and the position of the segments. In [64], an optimization approach considers the biomechanical constraints together with the biases of the inertial sensors and the error of the limited DOF at the knee joint. In addition, the body-IMU calibration parameters are estimated simultaneously, but the accuracy of such parameters is not evaluated in that work. Moreover, this approach cannot be used in a real-time application because it requires a batch of observations. In [138], a similar approach is developed by considering additional priority equations and using a sliding window optimization, which makes it more suitable for real-time estimation. They have also provided an assessment of repeatability in the estimation of calibration parameters. However, this approach is still associated with high computational cost due to the online estimation of additional calibration parameters.

In the same category of methods, Luinge *et al.* [70] used the kinematic coupling (KIC) algorithm for a hinge joint. Assuming  $A$  and  $B$  are IMUs, which are mounted on the adjacent

segments of the joint  $m$  from the coupling concept, the following constraint is defined:

$${}^G\Delta\vec{P} = {}^G\vec{l}_mB - {}^G\vec{l}_mA \quad (2.18)$$

, where  ${}^G\Delta\vec{P}$  is the relative position of  $B$  wrt.  $A$  and  ${}^G\vec{l}_mA, {}^G\vec{l}_mB$  are the distance vectors between joint  $m$  and the respective IMUs, all defined in the global coordinate system,  $G$ , which is typically aligned with gravity and magnetic north. In this approach, the EKF state vector with a length of 21 contains following parameters: the relative positions and velocities of two adjacent segments of the joint, the error in the orientation of the segments, gyroscope biases, and the acceleration of sensor A predicted by low-pass filtering, in order to extract the gravity measurement. They also prove an extension of this approach for two joints, knee and ankle, to estimate the positions and the velocities of three segments. Therefore, if no magnetic field is estimated the length of the state vector, when no magnetic field is estimated, is increased to 39 for 13 state variables. For this algorithm, the joint positions are required to be known with an accuracy of 2 – 3cm.

In this thesis, a similar approach to [70] is used to estimate the relative position of the segments of a leg, with respect to a reference point, in this case the pelvis, provided that the orientation of pelvis is known. The body-IMU calibration parameters are integrated to reduce the error due to angular velocity drift. Therefore, there is no need for additional states or measurements, e.g. magnetometer.

## 2.5. Exercise Monitoring

It is common practice that the trainers initially monitor trainees and instruct them based on their state of health while they perform a strength exercise for the first time so that they can later perform the exercise independently. The likelihood of injury is usually high in this later phase, as the correct way doing of the exercise cannot be adequately controlled. This is important, especially in the rehabilitation process, where the ROM is limited in the different phases of recovery. Since the physical characteristics and abilities of individuals vary, a personalized monitoring application is necessary. Therefore, patients who normally have difficulty going to the rehabilitation centers can do the exercises at home.

Exercise identification is the process of identifying the start and stop time of one repetition of an exercise, which could be composed of multiple smaller components, known as motion primitives. Short-term factors such as fatigue or long-term factors such as different stages in rehabilitation will result in the motion pattern of an individual to differ over time. Therefore, the identification algorithm should deal with the spatial and temporal variability.

A further challenge in the identification of movement data is the scalability to the higher dimension to achieve online monitoring.

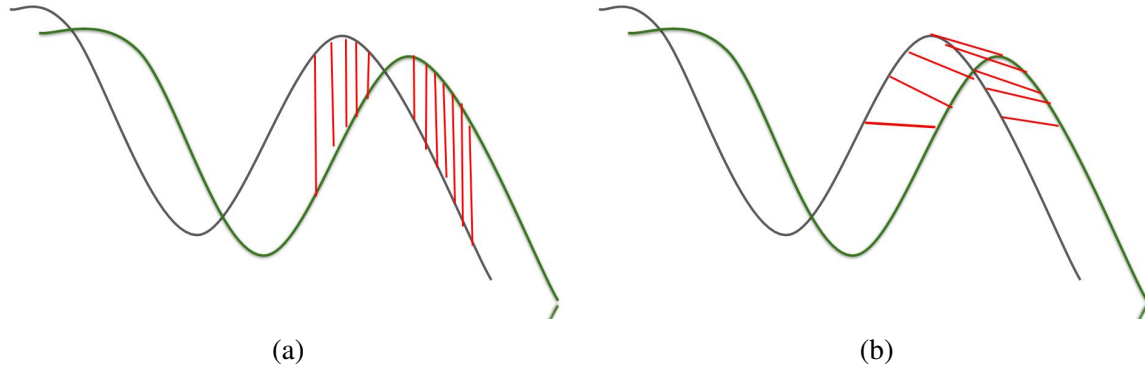


Figure 2.6.: Similarity measures: (a) Euclidean distance (b) DTW distance

## 2.5.1. Time series data mining

A time series is a collection of values, for example, motion signals that are provided sequentially over time. In time-series data mining, the goal is to realize the human ability in recognition of the shape of the data; In other words, identification of similarities between patterns while ignoring small fluctuations and considering different time scales, e.g. if the exercises are performed correctly from time to time but at different speeds. Some of the important terms in this area are introduced below:

### 2.5.1.1. Similarity measure

This is defined by a function which returns the distance,  $D(X, Y)$ , between two input time series  $X, Y$  and has the following properties:

$$D(X, Y) \geq 0, D(X, Y) = D(Y, X), D(X, Z) \leq D(X, Y) + D(Y, Z) \quad (2.19)$$

The Euclidean distance is one of the computationally simple examples of the similarity measure used in data mining [57]. Although it is time- and space-efficient, it is highly sensitive to the fluctuations in the time axis [8]. The similarity measure used in this thesis is the DTW [11] which compared to Euclidean handles the local distortions in the time axis better, see Figure 2.6 and usually provides robust results [30]. This is described in detail in Chapter 6.

Assuming the set of all subsequences of length  $m$  in  $X$ ,  $S_X^m$ , and  $X' \in S_X^m$ , a subsequence similarity measure is defined as:

$$D_{subseq}(X, Y) = \min(D(X', Y)) \quad (2.20)$$

, which represents the distance of  $Y$  from its best matching point in  $X$ .

### 2.5.1.2. Range query

Based on a similarity measure  $D$ , the range query finds a set of time series,  $S$ , which lie within a given distance,  $\epsilon$ , from a given query,  $Y$ :

$$S = \{X_i \in X \mid D(X_i, Y) \leq \epsilon\} \quad (2.21)$$

### 2.5.1.3. Subsequence matching

Based on the range query with a subsequence similarity measure, subsequence matching finds all subsequences  $X' \in X$  with  $D_{subseq}(X', Y) \leq \epsilon$ .

### 2.5.1.4. Segmentation

Segmentation is the process of finding the starting and ending location of a pattern of interest in the time-series data. In motion segmentation, this results in the sequence of motion data being divided into motion primitives. zero velocity crossing (ZVC) is a popular method for extracting motion primitives, which is explained in more detail in the next section.

## 2.5.2. Exercise identification

After motion data segmentation, each segment can be labeled to identify a type of exercise. Usually, repetition in strength exercise involves a sequence of increasing and decreasing velocity. Therefore, the ZVC approach is one of the most optimal approaches to find the motion primitives where the velocity of the signal changes the sign. In [37], it is assumed that the ZVCs of different DOFs coincide, therefore the motion primitive is detected, where more than two DOFs have ZVCs with a time difference of  $300ms$ . This method was applied to the position data obtained from electromagnetic sensors.

The Hidden Markov Model (HMM) is a stochastic approach that considers a signal as unobservable sequences of Markov states. At each time point, the system undergoes a state transition defined by a probability in a transition matrix. In [52], a template-free approach is proposed, where the data is windowed and the probability density function of each window was used in a hidden Markov model (HMM) in order to different states of the movements. The segment is identified, where the transition between the states occurs.

HMM is used more in the template-based approaches. In [9], this approach is applied to the segmentation of movements in sign language, which contains the finger positions, measured with ultrasonic gloves. Although they have reduced dimensionality using principle component analysis (PCA), their approach suffers from expensive computational costs. In [68], a two-step approach is proposed to solve this problem by reducing the number of HMM runs. This is achieved by first scanning the observation signal for the candidate segments, using ZVC or velocity peaks in the joint angles.

There are other learning-based classifiers that are used for motion identification, such as Convolutional Neural Networks (CNNs) [143] or support vector machine (SVM) [84]. However, these need enough labeled training data to ensure acceptable accuracy.

An alternative method that does not require training data is DTW. DTW is a popular template-based algorithm that calculates the distance between each point of the observed signal and the template and creates a distance matrix. This matrix is searched for a warping path, which leads to a minimum distance. This can be applied to identify an exercise, given a template of motion data, performed, and captured under the supervision of a trainer. DTW is a suitable solution for such cases as it allows temporal and spatial variations. However, the time complexity of DTW is  $O(n^2)$ , so that it can only be used for offline scenarios due to the high computational cost, especially in higher dimensions. In [63] an online DTW approach is proposed. To speed up the process of searching for the warping path, a similar approach to [103] is used to apply constraints to the warping path by defining two ranges for the start and end points. This constrains the warping path to eliminate unnecessary calculations. However, this leads to approximate results compared to the original DTW. Moreover, this method requires training of multiple template classes and the time complexity is still high as all distances in the matrix of each template class must be updated on the arrival of each sample in the stream. This approach is applied for motion segmentation of a personalized virtual rehabilitation in [150], where they applied the k-nearest neighbor approach to find the best motion primitives. UCR [102] finds the best-so-far subsequences in the static time series using the idea of early abandoning of DTW computation based on a cascading lower bounds. This prunes off many candidates during the search, which leads to higher speed. This approach applies an incremental z-score normalization, which results in fast and accurate processing. SUCR [41] is UCR for streaming time series. Both UCR and SUCR can only find the subsequences that have the same length as the template. In [116] an online approach is proposed that addresses the problem of subsequent matching using DTW. This algorithm has a linear time complexity of  $O(n)$ , which means the processing time of the current observation point does not depend on the past data length. Moreover, it only requires a single matrix to find the matching subsequence. In [116], they experimented the algorithm with various types of datasets, including an experiment on joint position data from an optical motion capture system is presented. However, the analysis is restricted to the execution time while no detailed analysis is provided in terms of precision and accuracy. In this thesis, this algorithm is optimized using an online segmentation technique based on ZVC and evaluated for real-time motion identification of different types of motion signals and compared with [116] and three other modifications of it in terms of both execution time and accuracy.





## 3. System Design

This chapter introduces the design and development of a low-cost motion tracker system, including a network of wired MEMS-based IMUs that fits into a suit for the feasible capturing of human body motion. In order to enable long-term data acquisition, using a microcontroller low power consumption is used a new approach for data acquisition for multiple sensing units is proposed. This method reduces the load on the central processing unit (CPU) and the wiring effort.

The first section presents related works. Section 3.2 describes the proposed design. This contains the details of the hardware and firmware design, including a novel cascaded approach to data acquisition and a power management process to increase the energy efficiency of the system. It also provides the specification of the software platform. The system is evaluated in Section 3.3 in terms of power consumption, weight, cost, and measurement quality compared to similar products available.

### 3.1. Related Work

This section explains the most common technologies used for motion capturing. These include visual, inertial, and magnetic tracking systems. Section 3.1.4 presents a more specific type of such a system, namely wearable motion monitoring systems, and describes their design considerations for two main components, i.e. the sensing units and the communication interface.

#### 3.1.1. Visual systems

The visual motion capture system can be defined as a system that encodes motion from successive images into values such as body segment positions or joint angles. Research in this field can be divided into two areas: marker-based and marker-free systems.

##### 3.1.1.1. Marker-based systems

In these systems, markers are attached to the body segments, and their positions are recorded by multiple surrounding cameras. One type of markers is passive markers that have a retroreflective material so that they reflect the infrared light emitted by the LEDs. These LEDs are mounted around the camera lens [147]. The positions of these markers are tracked by triangulating multiple overlapping projections from two or more calibrated cameras. The other type is active markers that can generate light themselves. While the former can have problems such as false reflections or noisy and missing data, the latter provides clean, high-quality motion detection

and real-time visualization without time-consuming post-processing [101].

However, there are problems with both techniques when using for body motion tracking, such as the unreliable detection of bony landmarks, soft tissue, and wobble markers that lead to faulty estimates.

### 3.1.1.2. Marker free systems

The availability of high-resolution cameras promotes the use of marker-free techniques for human motion tracking in many applications, e.g. in film production, gaming, and diagnosis [15, 32, 69, 87]. With this method, the subject does not need to wear the markers since every pixel recorded is a marker. The optical flow technique is used to estimate the movement of each pixel over time [49].

The model-based approaches in [25, 40] predict a number of parameters such as joint angles and synthesize the human model from the perspective of different cameras. They compare the real image edges with the synthesized ones and update the parameters for the best match.

Learning-based approaches such as [29] derive the 3D pose directly from the images or track the variables learned from the observation and then reconstruct the movements. In [127], a low-cost solution based on depth images is introduced using Kinect [91].

In order not to be limited to indoor infrastructure, i.e. fixed installed cameras, [126, 149] propose the idea of single or multiple cameras worn on the body. The relative positions of body segments, as well as the global body position, are estimated based on structure from motion (SfM). Here, the changes in the images of the external environment caused by the movements of the users are recorded. However, it is a challenge to use such systems for body motion tracking applications because the single-camera approach does not capture detailed body motions, and the multi-camera approach has a heavy weight and high computational latency. Moreover, both systems require knowledge of the environment in advance, which consequently requires intensive calculations to reduce errors and delays in data during 3D localization.

### 3.1.2. Inertial systems

In contrast to visual systems, inertia-based systems are of interest for most applications of tracking human body motion. The main reason is that they can operate independently of external hardware. They are also unobtrusive, comparatively inexpensive, and easy to set up and use [79, 153].

In these systems, an IMU is mounted on each body segment, usually consisting of a 3-axis accelerometer, a gyroscope, and a magnetometer. The measurements from these sensors are recorded and processed to obtain the orientation and/or position of each segment or to estimate the joint angles directly. Using this data and biomechanical constraints, such systems track body movement. Filtering and sensor fusion approaches are used to reduce noise and drift during tracking [108]. As systems for human body tracking are mostly presented as wearable systems, further details on such products in relation to wearable motion trackers are dealt with in Section 3.1.4. The related works on various filtering and sensor-fusion approaches for inertia-based tracking of body motion are previously discussed in Sections 2.4.3 and 2.4.4.

### 3.1.3. Magnetic systems

Magnetic motion detection is a cost-effective approach without occlusion problems [85, 99]. This technique uses a magnetic transmitter consisting of three orthogonal coils. These coils generate an electromagnetic dipole field. The orientations and positions are extracted from the relative current and voltage between magnetic receivers mounted on the body segments and the magnetic transmitter. However, the result of tracking is influenced by electrical and magnetic interference and the area covered by a magnetic source. Several methods of filtering and system design are proposed to solve these problems [3, 92].

### 3.1.4. Wearable motion monitoring systems

With the advent of low-cost, miniaturized sensor technologies, a wide variety of wearable products containing such technologies are now available on the market. This contributes to the monitoring and maintenance of the physical well-being of individuals in the consumer sector. According to [75], the global market for wearable sensors is expected to exceed US\$ 2600 million by 2024, with a compound annual rate of 29% over the forecast period. Here, such products are described with regard to their sensing units and their communication interfaces in Sections 3.1.4.1 and 3.1.4.2.

#### 3.1.4.1. Sensing unit

Depending on the type of movements that need to be captured in different applications, wearable systems consist of single or multiple sensing units. Note that a sensing unit implies the integration of different sensors that can be accommodated in a single package and only be worn at one point of the body.

##### Single sensing unit

There are a large number of commercial products available in the form of a single sensing unit. The wristbands are one of the most popular wearable devices because they are portable and easily accessible. In addition to the inertial sensor technology offered by most of the smartwatches available on the market, some of them have an integrated global positioning system (GPS) for outdoor activities, e.g. running [39].

By using pressure sensors and the compass, altitude, air pressure, and tidal curve can be made available to the user [20].

By using optical sensors that detect the blood flowing through the veins, the user's heart rate can also be monitored and recorded [121].

More accurate monitoring of heart rate could be achieved by chest straps that measure cardiac parameters. This data is used to analyze exercise intensity and calorie consumption [98].

Clasps are another type of wearables that can be placed anywhere on clothing [124] [132].

All the above systems provide only general information about the intensity and possibly the nature of user activity. However, due to their limited number of sensing units, they do not provide the biomechanical details of body movements.

### Multiple sensing units

By increasing the number of sensing units, sufficient details about body movements can be provided. However, this can greatly increase the cost and weight of the wearable systems. One of the best-known manufacturers of IMU-based wearable systems is Xsens [153]. Their products are either strap-based with wireless trackers or in the form of a lycra suit with up to 17 wired trackers, see Figure 3.1. The output rate of strap-based systems is  $60\text{Hz}$ , and that of the suit is  $240\text{Hz}$ , both for the maximum number of trackers. A software package provides real-time 3D animation and diagrams for joint angles, segment positions, and kinematics. Although these systems provide data acquisition in any environment along with validated kinematic data, they have high prices [153]. They also do not support integration with personal mobile devices such as mobile phones or tablets. Therefore, their use is limited to the studios or for scientific research purposes.

A simpler and more affordable solution, also based on IMUs, is offered by a startup company called Enflux [33]. A solution for recording whole-body movements, shown in Figure 3.1 with 10 IMUs from this company, costs ten times cheaper than Xsens. Trousers and shirts have separate control units placed on the pelvis and chest. These units provide the measurements with the output rate of  $66\text{Hz}$ . The product comes with several Android and Windows-based apps for the prevention of sports injuries. A similar product is Smartsuit Pro from Rokoko [107], which integrates 19 IMUs (see Figure 3.1). However, the sensing units are bulkier and the price is twice as high as [33]. Furthermore, many scientific research projects have not targeted such products, so the quality of the measurements and motion estimation still needs to be validated. Athos [6] uses a different motion-capturing approach that provides fitness tracking solutions based on electromyography (EMG) technology (see Figure 3.2). The full-body suit contains 18 EMG sensors and four heart rate sensors. It provides real-time information about the activity of several muscle groups on the smartphone. Therefore, the user can see both the muscle distribution and the left-right balance during the workout. The cost of a shirt and shorts with two integrated cores is similar to Enflux. However, this system does not provide detailed biomechanical information, which is crucial for self-training applications without supervision.

#### 3.1.4.2. Communication interface

In most commercial IMUs, extra modules such as transceiver and battery are added to the sensing unit to achieve high mobility through wireless networking. This increases power consumption and leads to bulky packages that can hinder the user's movements during the workout. Therefore, such units are not suitable for integration into clothing. Moreover, the wired networking approach, which is usually based on the star topology, poses other problems, such as high complexity of connections in body network and low flexibility of movement [82, 136]. To increase flexibility, an alternative is the use of textile cables [33, 139]. This additionally facilitates the integration of connections into the clothing. As a further solution for better integration in clothing, the use of smart textiles in products such as Athos (introduced in Section 3.1.4.1) is proposed. Similar products are evaluated in [22] and [78] for different types of applications, including gait analysis. However, their degree of accuracy does not yet meet the high requirements of sports monitoring applications with regard to the estimation of joint kinematics. Moreover, each sensing unit should be dimensioned differently for different body areas of



(a) Xsens



(b) Entflux



(c) Rokoko (photo taken from fixguide.com)

Figure 3.1.: Commercial products integrating multiple sensing units: (a) Xsens suit (b) Entflux (c) Rokoko

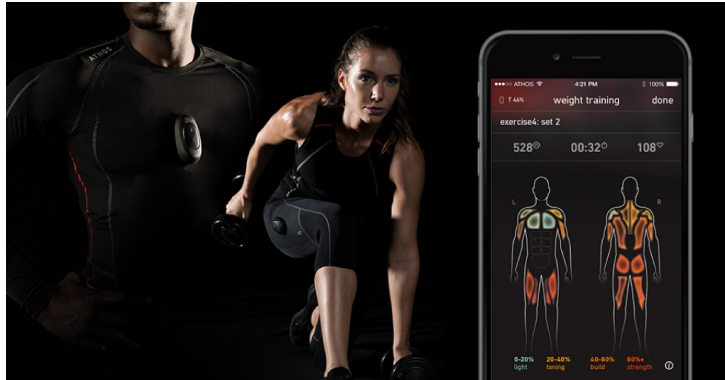


Figure 3.2.: Athos motion capture suit

different users [141].

When considering inertia-based motion detection suits with integrated wired IMUs, they usually have a control unit embedded in the garment or a hub that collects the readings from all the sensors and sends them via a wireless connection to a PC or mobile device for further processing. The type of wireless connection is an essential factor for the accessibility of the system. For example, the proprietary solution of the wireless communication protocol in [153] does not make it accessible to every personal mobile device, while the standard connections such as Bluetooth allow easier access [6, 33].

## 3.2. Proposed system design

This section introduces a novel design for a light-weight wearable system with low power consumption and multiple integrated IMUs. In hardware design, components are selected to reduce the overall cost and size of the system. This is described in Section 3.2.1. In addition to a selection of low-power components in hardware design, the power consumption is reduced mainly by a novel approach to data acquisition and power management in the firmware design process. This is explained in detail in Section 3.2.2. Finally, Section 3.2.3 provides a brief description of the software platform, including the user interface.

### 3.2.1. Hardware design

The hardware platform, shown in Figure 3.3, consists of multiple small-size (20 x 15 x 3 mm) and light-weight (2g) sensing units, which contain *MPU9150* IMUs from Invensense<sup>1</sup> (Figure 3.2.1).

*MPU9150* consists of 3-axis accelerometer and 3-axis gyroscope in addition to a 3-axis magnetometer (*AK8975*). This chip also contains a FIFO (first-in-first-out) buffer that reduces power consumption by allowing the CPU to trigger a burst reading of sensors and going in the low-power mode while the unit is collecting the measurements.

<sup>1</sup><https://www.invensense.com/products/motion-tracking/9-axis/mpu-9150/>

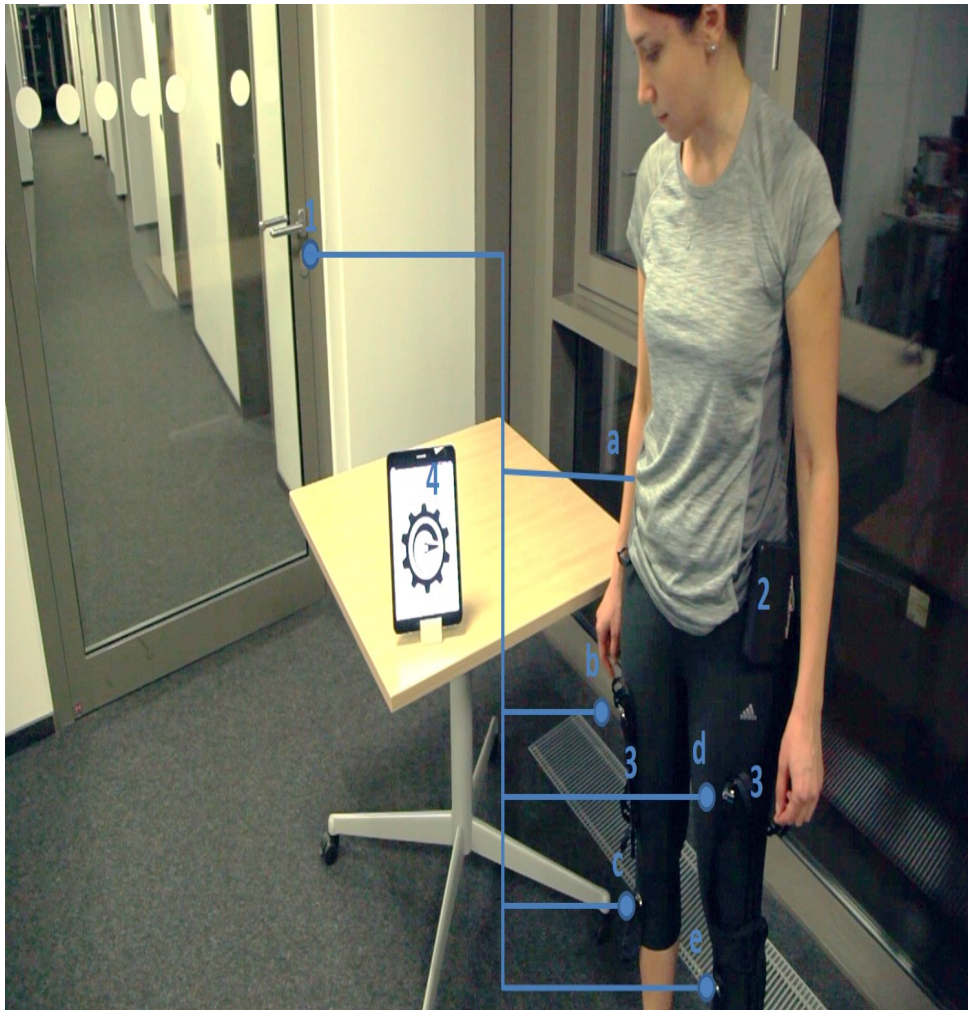


Figure 3.3.: hardware components: (1) 5 IMUs are mounted on pelvis (a, not visible), upper/lower right leg(b/c) and upper/lower left leg(d/e); (2) controller unit;(3) textile cables; (4) tablet to store and process data.

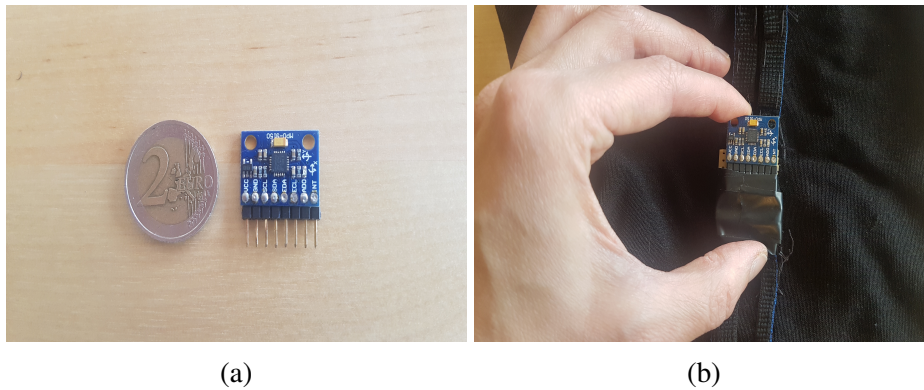


Figure 3.4.: (a) IMU (b) IMU connector

The controller unit (CU) (see Figure 3.5) is a SAM4N microcontroller<sup>2</sup> from Microchip (formerly Atmel) based on a 32-bit ARM Cortex-M4 RISC processor. It operates with a maximum clock frequency of 100MHz. Featuring a variety of serial interfaces, this microcontroller supports further expansion of the system in order to deploy different types of sensors and communication interfaces. In this work, *SAM4N XplainedPro*<sup>3</sup> is used, which is an evaluation board for this microcontroller. This board contains an embedded debugger, which facilitates the programming.

IMUs communicate with the microcontroller via the inter-integrated circuit (I<sup>2</sup>C) bus<sup>4</sup>, and the microcontroller receives the interrupts from the IMUs through the general purpose input output (GPIO) pins.

The IMUs are connected to each other and to the CU via 6-wire textile cables. To reduce the effects of cross talk and high capacitance of the I<sup>2</sup>C bus, the data lines are distributed over multiple cables, where more than one I<sup>2</sup>C connection exists. The connectors for the textile cables are designed based on standard 2.54 mm pin header for easier plugging and unplugging of the IMU boards. These connectors together with the textile cables are then sewed and fixed on a pair of stretch pants making sure that the connectors provide a suitable placement of IMUs for lower body motion capturing.

The data transmission to an external processing device, such as a smartphone or laptop, is possible through the universal asynchronous receiver-transmitter (UART) interface of microcontroller and is implemented via Bluetooth. The Bluetooth module is *HC05*, which follows standardized protocol the *IEEE* 802.15.1 standardized protocol and the maximum range of 100m.

### 3.2.2. Firmware design

The firmware is designed to provide two functionalities: initialization and data transfer. The initialization module detects and configures the available or user-selected IMUs and CU

<sup>2</sup><https://www.microchip.com/wwwproducts/en/ATsam4n16c>

<sup>3</sup><https://www.microchip.com/DevelopmentTools/ProductDetails/PartNO/ATSAM4N-XPRO>

<sup>4</sup><https://www.i2c-bus.org/>



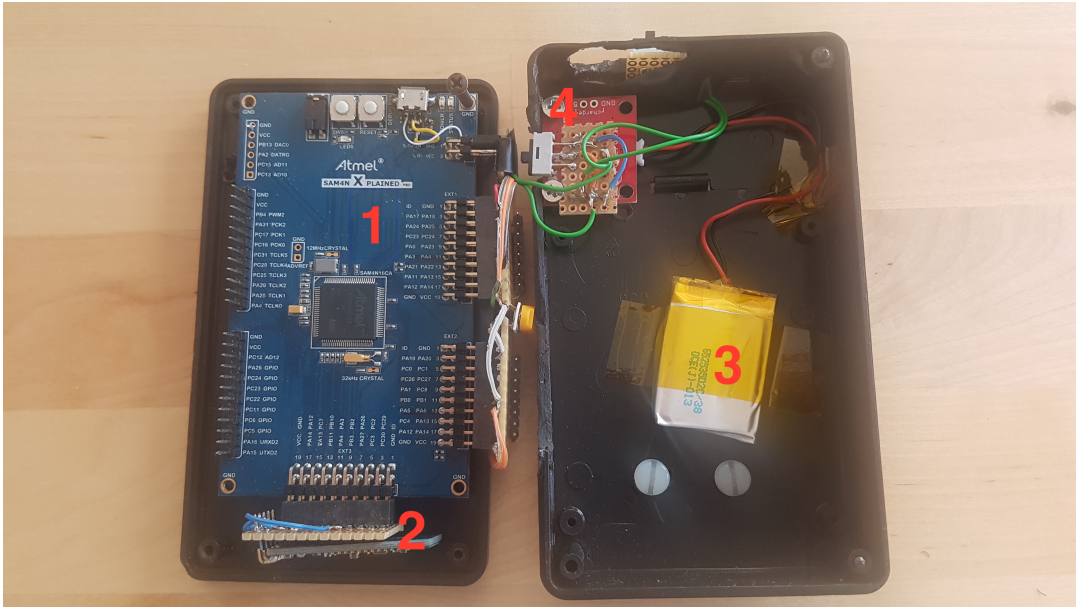


Figure 3.5.: controller unit contains (1) the microcontroller evaluation board; (2) Bluetooth module; (3) battery; (4) charger

interfaces.

In the data transfer module, the measurements are read from the sensors and transmitted to a remote device for further processing.

For efficient data acquisition from multiple IMUs without adding additional components such as multiplexers [104], a new cascaded approach is designed, which in contrast to the star-based networking approach has less wiring complexity. In addition, a power management approach based on direct memory access (DMA), has further optimized the system's energy consumption. Before describing the proposed methods, the main hardware modules used in this development are explained in the following paragraphs.

**Peripheral DMA Controller** The SAM4N microcontroller contains a bus matrix that manages the Peripheral DMA Controller (PDC) in parallel to the CPU. This refers to the communication between the peripheral devices, e.g. I<sup>2</sup>C and memory can be operated without CPU interference. This module can be configured through the user interface of the peripheral device. This interface contains sets of pointers and counters for the current and next data transfer. Using the transmit and receive signal, a peripheral triggers its channel on the PDC, to launch a data transfer. When data is transferred, the peripheral generates an end-of-transfer interrupt. This module is used in this work in mono directional receive mode for IMU data read via I<sup>2</sup>C, and in mono directional transmit mode for data transfer over Bluetooth via UART.

**I<sup>2</sup>C interface** enables serial communication over one clock line and one data line with the speed of up to 400Kbits/s. One or multiple master devices communicate with slave devices via this interface. Each message contains START/STOP conditions, the address frame including a

unique address of a slave device, data frame, read/write and ACK/NACK bits. Most IMUs have a single factory hard-coded address. It is therefore impossible to connect multiple similar IMUs to the same bus without additional hardware. This problem is addressed in the next section, and a solution is proposed.

**Auxiliary I<sup>2</sup>C sensor interface** is integrated into most of the MEMS based inertial sensors in the market [14, 86], to enable the connection with aided sensors e.g. magnetometers or pressure sensors. This interface supports two modes of master and pass-through. The latter is used for the external system to directly control the access to an external sensors on the auxiliary bus, directly. The former, which is used in this work, allows the sensor to act as a master and read out measurements of the external sensor directly without the intervention of an external processor. After configuration for different modes, this interface follows the same protocol as I<sup>2</sup>C interface for data transfer. In this work, the auxiliary bus has been deployed for communicating with a magnetometer in the same IMU as well as with a cascaded IMU. This connection is elaborated in the next section.

### 3.2.2.1. Cascaded approach

To retrieve the readings from multiple IMUs based on a polling approach, the CU should continuously switch between all these sensors. This causes a high CPU load and power consumption. Furthermore, the switching time leads to a lower output sampling rate and probably to data loss. To avoid such problems, the auxiliary I<sup>2</sup>C functionality of IMU was used to support master-slave transactions. This allows the design of a cascaded sensor-reading approach where each sensor in the higher level acts as the master and retrieves the data stored in a sensor in the lower level as the slave. For this approach, sensors are initialized before the main data transfer starts. During the data transfer, sensor measurements of all levels are taken from the buffers of the sensors of the highest level.

All sensor data can be called up according to a particular order of reading. This sequence is adapted to common joint angle estimation algorithms that use kinematic chains and a hierarchical processing scheme, such as the one presented in Chapter 5. Here, the first measurements update the base of a limb, e.g. the pelvis in a lower-body setting, followed by the second and third sensor measurements that update the upper and lower segments of the limb, e.g. the thighs and lower legs. In addition, this cascaded approach results in much less complicated wiring than the switching approach.

In this work each IMU can support up to five slaves via the auxiliary I<sup>2</sup>C bus. In order to keep the sequence and avoid operation interference, two slaves are defined to read a certain number of bytes and one slave is defined to write control values. Since the magnetometer is connected to the sensor via the auxiliary bus, two other slaves are reserved for controlling and reading from this sensor.

Since the microcontroller provides two separate I<sup>2</sup>C buses with a two-level cascaded method on each I<sup>2</sup>C bus, up to 8 IMUs can be connected. Figure 3.6 displays the first level of the

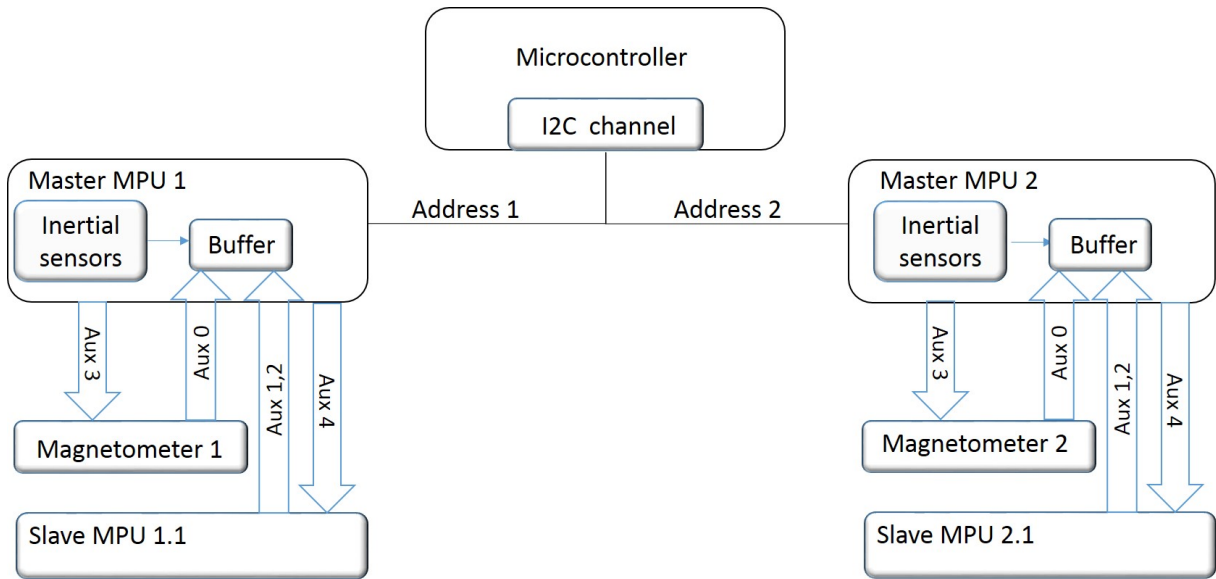


Figure 3.6.: Data acquisition using the cascaded approach.

cascaded configuration. The buffers of the sensors in the higher level are configured to be filled with the data provided by the slaves from the sensors in the lower level at the same speed as their sampling rate.

### 3.2.2.2. Power management

The data transfer module puts the CPU into sleep mode by means of a Wait For Interrupt function. The firmware enables I<sup>2</sup>C data transfer on a DMA channel when a Data Ready interrupt is received from a master IMU. Therefore, the measurements are transferred from the IMU to memory while the CPU is switched back to sleep mode and waiting for a Transfer Complete interrupt. This process is executed sequentially for all available master IMUs.

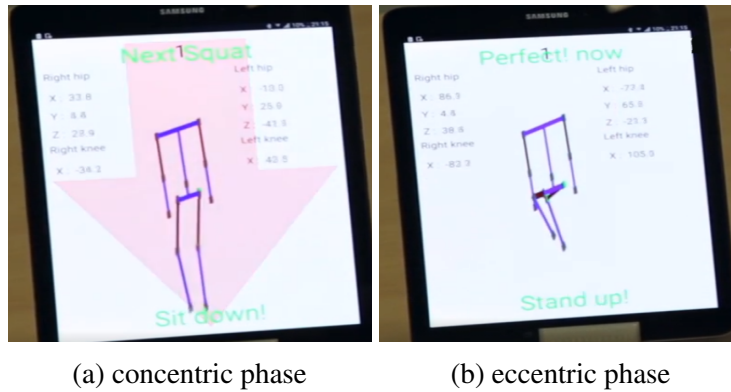
Once the I<sup>2</sup>C transfer is complete, the UART data transfer on a DMA channel is activated to transfer the data from the memory to the external device.

A SysTick timer is used to prevent deadlock situations by checking and restarting the blocked data transfer processes.

### 3.2.3. Software

The software for monitoring the strength exercises is implemented on a Macbook in C++ and on an Android-based tablet in Java and Java native interface (JNI), which is used to develop the methods of calibration, motion tracking and identification in the Chapters 4, 5, and 6. In addition, a user interface is developed to select among the available IMUs. This is beneficial since a user can customize the system for different types of exercises.

For real-time feedback, a stick figure visualization is developed using Open GL ES. Furthermore, an identification and guidance feature is provided for the current and the next phases of



(a) concentric phase

(b) eccentric phase

Figure 3.7.: The stick figure visualization of squat exercise on tablet. Each phase of squat is detected and user is guided to the next phase

	1 IMU no DMA	1 IMU with DMA	2 IMUs with DMA	2 IMUs with DMA and cascaded
Time [us]	2646	7.77	15.4	7.84

Table 3.1.: Effect of using DMA and cascaded approach on the CPU processing time

the squat exercise. Figure 3.7 shows this application on the tablet.

### 3.3. Experimental results

In the following, the system evaluation in terms of power consumption, weight, and costs, as well as measurement quality, is presented.

#### 3.3.1. Power consumption

To evaluate the performance of the proposed data acquisition method in reducing the power consumption, CPU processing time and power consumption are measured in two experiments and compared with the direct reading, subsequently referred to as the traditional method. Both the proposed and the traditional methods are interrupt-driven and use the sleep mode. However, in the traditional method at each sampling, the IMU measurements are directly read through I<sup>2</sup>C and written on the UART interface.

In the first experiment, the processing time, as one of the major factors in increasing the power consumption is measured by counting the CPU cycles in read/write mode and dividing those through the clock speed.

The results in Table 3.1 shows that using DMA reduces the CPU load during sampling by 99 percent.

	4 IMUs, sampling	4 IMUs, init.	8 IMUs, sampling
traditional method [mA]	22.6	13.2	not supported
proposed method [mA]	9.5	12.7	9.8

Table 3.2.: Comparison of the CPU current drain

Moreover, with the cascaded approach, one more IMU can be added without increasing the processing time by eliminating the need for switching between different I<sup>2</sup>C addresses.

For a more practical evaluation, the second experiment measures the current consumption while sampling a maximum number of IMUs, which the current system can support without using extra components, *i.e.*, 4 IMUs using the traditional and 8 using the proposed method. The results in Table 3.2 show that using the proposed method reduces the power consumption by 58 percent.

During initialization, both methods have almost comparable power consumption, the value is slightly less for the proposed method, since it establishes the connection to 4 IMUs on a single I<sup>2</sup>C bus, while the traditional method requires two I<sup>2</sup>C buses.

The result for the sampling of 8 IMUs implies that the use of the proposed methodology to increase system capacity to support twice the number of IMUs will further optimize power consumption.

The total power consumption of the system with a 5V power supply was measured 414 mW.

### 3.3.2. Weight and cost

The weight of the proposed system is compared with two commercially available inertial motion capturing systems in Table 3.3. Since the commercial systems cover the full-body, the respective weights have been halved for easier comparison. The table shows that the weight of the IMUs used in this work is significantly lower than those used in other products.

Moreover, the total cost of the components used, including the controller, eight IMUs, the required amount of textile cables, and the pants, is less than 200 euros, which can be a promising premium price for an affordable final product.

### 3.3.3. Measurement Quality

The IMUs were individually calibrated using the procedures described in Chapter 4. The evaluation focuses on the quality of the inertial data (rather than the magnetometers), which provide the most critical information for motion tracking (Chapter 5).

Figure 3.9 illustrates the calibration results of one IMU by showing the calibrated accelerometer and gyroscope measurements, which were continuously captured under 24 different static poses and 24 different 90-degree rotations, *i.e.* four on each side of the calibration cube with the IMU mounted inside, Figure 3.8.

	XSENS [153]	Animazoo [4]	Proposed system
IMU weight [g]	30	11.2	2
controller weight [g]	200	45	164
suit weight(Total) [g]	965	750	453

Table 3.3.: Weight comparison

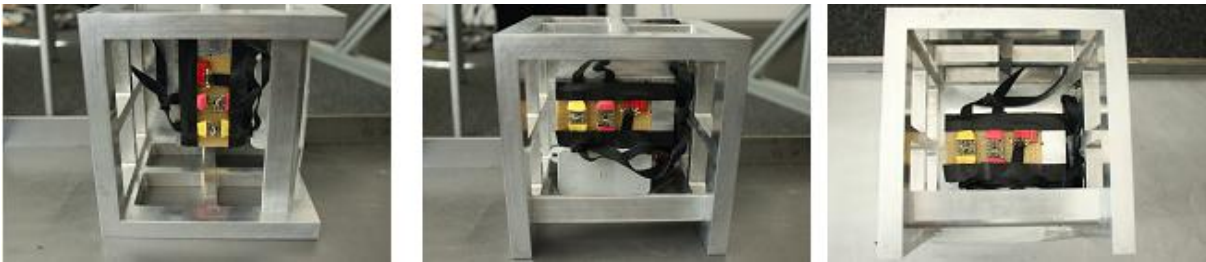


Figure 3.8.: Inertial sensor calibration: Calibration cube in different static poses on a leveled calibration table.

Having applied the estimated calibration parameters, the plots nicely illustrate the absence of sensor biases, scale errors and crosstalk between the different axes; e.g. during the static poses, as expected, one accelerometer axis measures around  $9.81 \text{ m/s}^2$  (i.e. gravity), while the other axes measure around  $0 \text{ m/s}^2$ . The peaks are also expected since they correspond to the 24 rotations of the cube.

In order to obtain quantitative results, the calibrated measurements of the proposed IMU were compared with those of two available commercial IMUs: Xsens [153] and Trivisio [142]. For this, 3000 calibrated inertial data samples were captured from each IMU in a static pose. For the proposed IMU, the temperature conditions were similar to those during the calibration procedure. For the commercial IMUs, the factory calibration parameters were used, i.e. no re-calibration was performed. The results in Table 3.4 show acceptable gyroscope biases for the proposed IMU, which are in the range between the Xsens and the Trivisio.

The average accelerometer vector length also nearly equals gravity for all of the IMUs. Gyroscope and accelerometer noise levels are given in terms of the trace of the covariance matrix. While the accelerometer noise level of the proposed IMU is in the same order of magnitude as the Trivisio, both are two orders of magnitude higher than the Xsens.

For the gyroscopes, the noise level of the proposed IMU is lower compared to both commercial IMUs (one order of magnitude compared to Trivisio and two orders of magnitude compared to Xsens). Note that the quality of the gyroscope measurements plays a dominant role in inertial

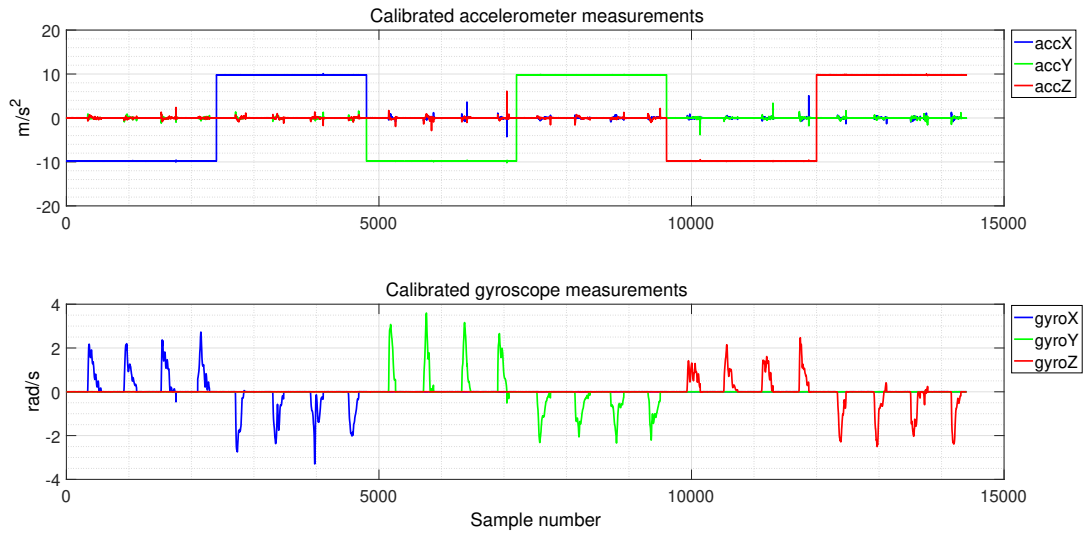


Figure 3.9.: Calibration results.

	MPU9150	Trivisio	XSENS
Gyroscope bias [rad/s]	0.004	0.0006	0.04
Accelerometer vector length mean [ $m/s^2$ ]	9.818	9.819	9.816
Gyroscope covariance trace	$2.4 \times 10^{-6}$	$4.1 \times 10^{-5}$	$5.55 \times 10^{-4}$
Accelerometer covariance trace	0.001	0.002	0.00001

Table 3.4.: Measurement quality evaluation in terms of noise levels (standard deviation under static conditions).

motion estimation.

The above experiment shows that, under static conditions, the measurement quality provided by the proposed low-cost and light-weight IMU is comparable to well-known commercial systems. Assessment of its long-term behavior and the measurement quality under dynamic and varying temperature conditions is presented in the next chapters.

### 3.4. Conclusion

This chapter presented the design and development of a low-cost and unobtrusive wearable system for lower body motion capturing, designed for long-term monitoring and support of users' daily workout. Low power consumption and user convenience, which are two fundamental challenges in the development of motion capture systems, are considered in design and development aspects.

Energy-efficient systems are necessary for many applications, such as long-term health monitoring. In the proposed system, this is achieved by utilizing low-power components and a novel data acquisition approach, that reduces the CPU load.

The system is designed so that all electronic components can be integrated and/or hidden in a flexible suit. This makes it more appealing and convenient for the user. Low weight and small dimensions of the components provide a suitable platform for applications with high dynamics, such as sports training.

Furthermore, given the small form factor and light weight of the sensors allow for more stable and precise positioning on the limbs, reducing unwanted motion artifacts.

Future work will focus on further miniaturization of the controller board to increase wearing comfort. Additionally, the data transmission of this system can be further optimized further by implementing a real-time and in-situ motion tracking approach on the controller unit. This reduces the packet size by transferring only three angles instead of nine measurements per IMU. In addition to providing the tracking and detection algorithms in a mobile platform, the current software is customized to select which of the connected IMUs are involved in the monitoring process. When a user study is conducted in the future, the software's user interface can be further enhanced to provide more personalized options, such as the planning of exercises based on the evaluation of progress.



## 4. System Calibration

To use the IMUs to track the body movements, these sensors must be calibrated before they are attached to the body segments. Therefore, the first two sections of this chapter are dedicated to the calibration of sensors in the IMU. Since the magnetometer measurements can easily be influenced, e.g. due to the ferromagnetic materials in the vicinity, this work in Section 4.2 proposes a practical and in-field magnetometer calibration. This approach is evaluated in terms of magnitude deviation, heading error, plane projection, and repeatability.

Moreover, after mounting, knowledge of the IMU poses relative to the body segments is crucial to enable accurate pose estimation. This is known as body-IMU calibration and is described in Section 4.3. The observability analysis of an existing method is presented, and based on this, new constraints are proposed to improve the autocalibration procedure. This approach is evaluated using synthetic and real data containing different types of movements.

### 4.1. Inertial Sensors Calibration

In order to convert the digital outputs of the gyroscopes and accelerometers to physically meaningful measurements of 3D angular velocity ( $rad/s$ ) and 3D acceleration ( $m/s^2$ ), the sensors must be calibrated for offsets, scale factors and alignment errors in the three sensitive axes. The measurements of the gyroscope( $\tilde{\vec{\omega}}$ ) and the accelerometer( $\tilde{\vec{a}}$ ), can be formalized as:

$$\tilde{\vec{\omega}} = C_{\omega} S_{\omega} \vec{\omega} + \vec{b}_{\omega} \quad (4.1a)$$

$$\tilde{\vec{a}} = C_a S_a \vec{a} + \vec{b}_a, \quad (4.1b)$$

where  $\vec{\omega}$ ,  $\vec{a}$  are the true angular velocity and acceleration, and  $\vec{b}_{\omega}$ ,  $\vec{b}_a$  are the gyroscope and accelerometer biases.  $S_{\omega}$  and  $S_a$  are the diagonal matrices containing the scale factors of the three axes of each sensor.  $C_{\omega}$  and  $C_a$  are the rotation matrices representing the misalignment between the actual and nominal sensitivity axes of the sensors. Here the influence of the linear acceleration on the angular velocity is assumed to be negligible.

The typical calibration principle is to expose the inertial sensors to a known angular velocity and linear acceleration and to select the calibration parameters in such a way that the observed sensor output becomes as probable as possible. However, in order to avoid the need for sophisticated equipment, such as a turntable, a method proposed by Ferraris *et al.* [35] was used, which is based on known rotations and local gravity. The procedure requires a series of manual manipulations of a high-precision cube containing the IMU on a leveled surface (see Figure 3.8). More precisely, for each of the six sides, the cube is first held stationary and then rotated in steps of 90 degrees on the respective side. The calibration parameters of both the 3D accelerometer

and gyroscope are then derived by solving a linear equation system based on the sensor model, the known poses and orientations, and the raw measurements captured under static poses and single-axis rotations. The necessary equipment, i.e. a calibration table ( $33 \times 33 \text{ cm}$ ), which can be precisely leveled and has an orthogonal edge on one side, as well as a high-precision aluminum cube ( $15 \times 15 \times 15 \text{ cm}$ ) with a mounting plate ( $6 \times 10 \text{ cm}$ ) for IMU fixation were explicitly designed (see Figure 3.8). The calibration procedure is performed once for each sensor before integration into the motion capture suit, and the resulting calibration parameters are permanently stored.

## 4.2. Magnetometer Calibration

This work proposes a practical method for in-field magnetometer calibration and alignment to the coordinate system of an IMU. The procedure is attitude-independent and works without the need for precise equipment or external heading information. It is based on the assumption of a homogeneous magnetic field during calibration, i.e. of constant magnitude and inclination of the Earth's magnetic field vectors independent of the IMU pose. In order to extract this information correctly from the IMU measurements, the manual procedure is divided into two steps with different data collection approaches that are easy to perform and less error-prone than the one-step method proposed in [50]. In the first step, partly inspired by the method in [106], bias, scale factors and, non-orthogonality parameters are estimated using ellipsoid fitting and a set of magnetometer measurements recorded under motion. After an orthogonal coordinate system has been defined in the first step, a rotation, which aligns this system with the IMU coordinate system given by the inertial sensors, is achieved in the second step. This step is based on the assumption of constant inclinations and uses a set of accelerometer measurements under different static poses, thus removing errors due to body acceleration. In contrast to the method in [50], the proposed approach is independent of the location on earth since the magnetometer calibration parameters are estimated in the first step purely from the magnetometer measurements. The presented method provides a reliable parameter estimation, which is confirmed by several experiments comparing the results with two calibration methods provided by commercial IMUs.

### 4.2.1. Parameters

#### 4.2.1.1. Magnetometer calibration parameters

As shown in [106], to convert the sensor readings,  $\tilde{\vec{m}}$ , into the true magnetic field,  $\vec{m}$ , in the magnetometer coordinate system, each axis should be corrected for bias, scale factor, and non-orthogonality, according to the following model:

$$\vec{m} = C_m S_m^{-1} (\tilde{\vec{m}} - \vec{b}_m), \quad (4.2)$$

where  $\vec{b}_m$  defines the bias vector,  $S_m$  is a diagonal matrix containing the scale factors, and  $C_m$  is a lower triangular matrix that is used to correct non-orthogonality as suggested in [145].

#### 4.2.1.2. Misalignment parameters

Equation (4.2) defines an orthogonal magnetometer coordinate system. To relate the calibrated magnetometer measurements,  $\vec{m}$ , to the inertial measurements, namely acceleration, and angular velocities, the respective coordinate systems must be aligned. Since the IMU frame and the magnetometer frame are both orthogonal, the alignment consists of a rotation, which can be parametrized in a minimal way by an axis-angle representation (Appendix C). The resulting model for converting  $\vec{m}$  into an aligned vector,  $\vec{m}_{aligned}$ , is then given by:

$$\vec{m}_{aligned} = Rot(\vec{\theta})\vec{m}, \quad (4.3)$$

where  $\vec{\theta}$  contains the axis-angle parameters of the rotation, and  $Rot(\vec{\theta})$  denotes their conversion to a rotation matrix (see Appendix C).

### 4.2.2. Calibration Method

As already mentioned, the calibration method consists of two steps. The first step is to sample the IMU while manually rotating it in all directions to obtain sufficient coverage of the ellipsoid. The magnetometer calibration parameters are then calculated from the recorded raw magnetometer measurements. In the second step, the IMU is sampled while it is static and posed in different directions. The misalignment parameters are then estimated using the recorded magnetometer measurements (calibrated with the results of the first step) and the acceleration measurements, which provide the gravity under static conditions.

#### 4.2.2.1. The first step (dynamic)

Assuming a homogeneous field such as the Earth's magnetic field without disturbances, the locus of the true magnetometer measurements in the sensor frame is on the surface of a sphere with the center at the origin and the radius equal to the intensity of the local magnetic field. This sphere is deformed into an ellipsoid as a result of biases, scale factors, and non-orthogonality [145]. Therefore, the compensation of these effects can be seen as a problem of fitting an ellipsoid to the raw measurements by minimizing the sum of the squared geometric distances [38], for which a nonlinear least-squares optimization technique is required. With Equation (4.2), the minimization problem is defined as:

$$\underset{C_m, S_m, b_m}{\operatorname{argmin}} \sum_{i=1}^n (\|C_m S_m^{-1}(\vec{m}_i - \vec{b}_m)\| - m_{ref})^2, \quad (4.4)$$

where  $n$  is the number of magnetometer measurements. The constant  $m_{ref}$  is equal to the local geomagnetic field intensity, which can be selected according to the given location. Here, it is set to unit length since only the direction of the magnetic vector is important for the application of motion tracking.

Typically, an iterative nonlinear optimization technique requires a good initial guess. This is

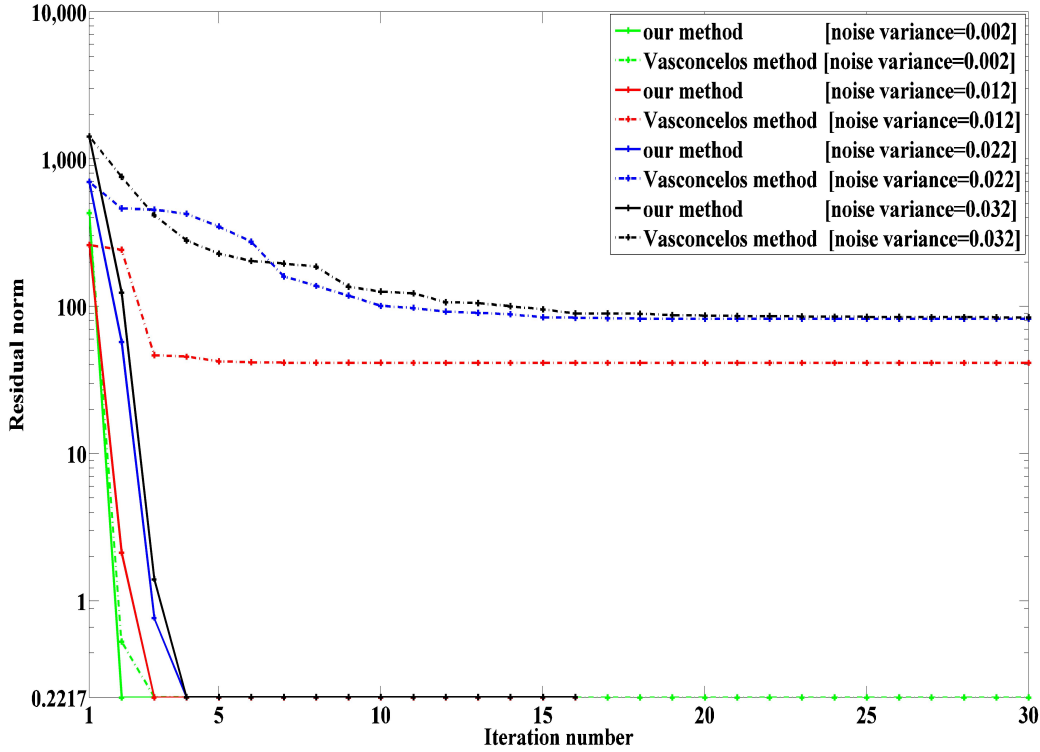


Figure 4.1.: Illustrates the development of the residuals in relation to the performed iterations when starting with the same initial guess.

achieved by the linear least-squares approximation proposed in [106], which is based on Singular Value Decomposition (SVD). Since the experiment has shown that under realistic calibration conditions the initial guess is easily perturbed by sensor noise, a preliminary study examined various optimization tools with respect to their sensitivity to such disturbances. Our final method uses the Levenberg Marquart algorithm (LMA) [83], which proved to be considerably more robust than the Newton method as used in [145] (see Figure 4.1 for the selected results of the preliminary study).

#### 4.2.2.2. The second step (static)

In order to obtain the misalignment parameters, we used inclination which is defined as the angle between the Earth's magnetic field vector and the horizontal plane of the Earth and varies at different geographical locations [89]. However, this angle can be considered constant for a local area, where the calibration procedure takes place. Using the fact that the gravity vector,  $\vec{g}$ , is always orthogonal to horizontal plane of the Earth, the following equation is derived:

$$\vec{g}^T \vec{m}_{aligned} = \cos(\pi/2 - \alpha), \quad (4.5)$$

where  $\alpha$  indicates the local inclination angle. Here,  $\vec{g}$ , as obtained from the accelerometers under static conditions, and  $\vec{m}_{aligned}$  are assumed to be normalized and specified in the IMU coordinate frame. Substituting (4.3) in (4.5) results in a nonlinear optimization problem, which is again solved with LMA:

$$\operatorname{argmin}_{\vec{\theta}, \alpha} \sum_{i=1}^n (\vec{g}_i^T \operatorname{Rot}(\vec{\theta}) \vec{m}_i - \cos(\pi/2 - \alpha))^2, \quad (4.6)$$

where  $n$  is the number of measurements,  $\vec{m}_i$  is the normalized  $i^{\text{th}}$  calibrated magnetometer measurement, and  $\vec{g}_i$  is the normalized  $i^{\text{th}}$  calibrated gravity measurement.

In order to obtain an initial guess, (4.5) can be reformulated using  $R := \operatorname{Rot}(\vec{\theta})$  and  $c = \cos(\pi/2 - \alpha)$ . This results in an equation system, which is linear with respect to  $R$  and  $c$  and can be solved for these parameters with SVD: R to the axis-angle representation [128] after having orthogonalized the matrix using SVD:

$$\vec{g}_i^T R \vec{m}_i - c = 0 \quad (i = 1 \dots n) \quad (4.7)$$

Parameter  $c$  provides an initial guess for the inclination, while initial values for  $\vec{\theta}$  are obtained by converting  $R$  to the axis-angle representation.

### 4.2.3. Experimental Results

#### 4.2.3.1. Test setup

The proposed calibration algorithm was implemented and tested using measurements from a commercially available IMU [142], which includes a two axes magnetometer (*MS2100*) combined with a single axis magnetometer (*SEN-Z65*) both manufactured by PNI<sup>1</sup>, and a tri-axes accelerometer (*ADXL345*) manufactured by Analog Devices<sup>2</sup>. The IMU measurements were sampled at 100 Hz using a USB transceiver. Figure 4.2 illustrates the effects and working principles of magnetometer calibration, visualizing the uncalibrated measurements in comparison to the calibrated ones. Ideally, after calibration, the data points should lie on the surface of a unit sphere located at the origin of the IMU coordinate system, i.e. the vectors should have unit length regardless of the IMU pose. In order to quantify the performance of the proposed calibration procedure, various criteria were defined and evaluated. First, the deviation from unit length (magnitude deviation) was evaluated on the basis of calibrated data sequences recorded under arbitrary IMU rotations. Then, the directional accuracy of the calibrated magnetic field measurements was investigated in terms of the heading error and plane projections based on known motions. These were performed in an especial test setup, as illustrated in 4.3 and consisted of rotations around the three axes of the cube, the latter being aligned with the IMU mounted inside. Using the above criteria, the results of the proposed algorithm were compared with the results of the calibration method provided with the software development kit (SDK) of the IMU, which corresponds to the aforementioned method of Hu *et al.* [50], and with the

<sup>1</sup><https://www.pnicorp.com/>

<sup>2</sup><https://www.analog.com/en/index.html>

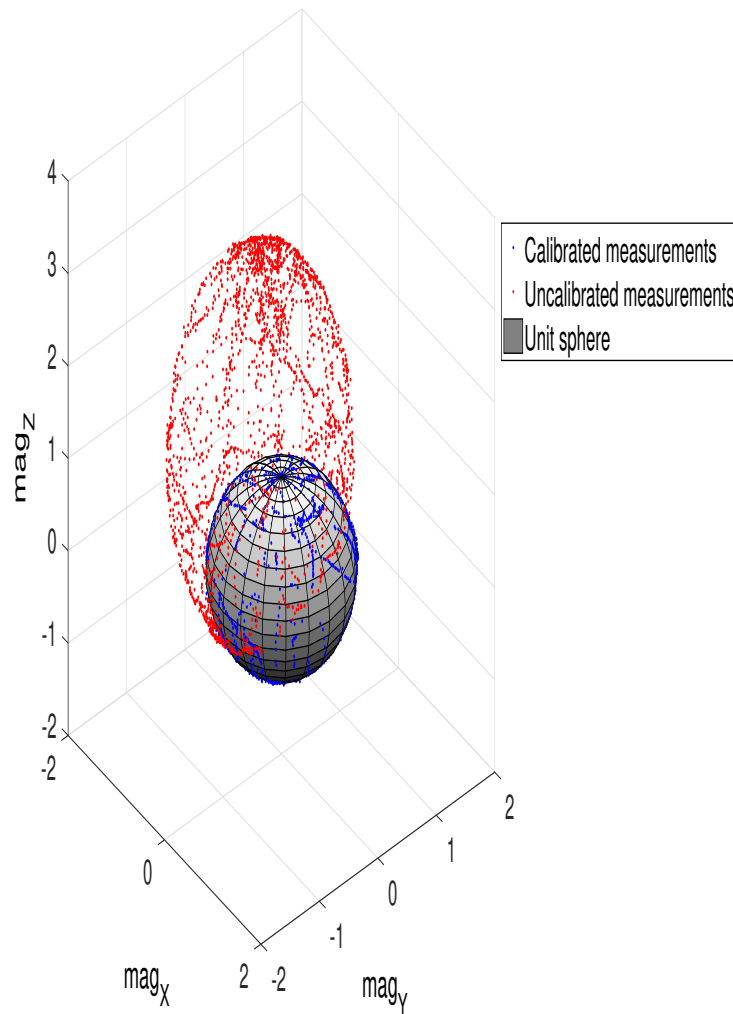


Figure 4.2.: Magnetometer measurements before (red) and after (blue) calibration by the proposed method. In order to simplify comparison, the uncalibrated measurements are scaled to the mean value of the magnitudes. Ideally, the calibrated measurements should map to a unit sphere.



Figure 4.3.: A high precision aluminum cube on a turntable made of glass and aluminum with a flat wooden plate as a levelled base served as test setup for performing known motions. Here, the Xsens MTi is mounted inside the cube.

calibrated magnetometer measurements of the Xsens MTi, which like established commercial IMU provided a baseline for the comparison. Prior to recording the evaluation sequences, both IMUs were calibrated in an outdoor area (in Kaiserslautern, Germany) to ensure a homogeneous magnetic field. The calibration of the Xsens MTi was performed based on the instructions in [153]. The calibration parameters for the Trivisio IMU were determined using both the method provided in the SDK (Hu *et al.* ) and the proposed method. Since the proposed calibration algorithm is based on a manual data acquisition procedure, in addition to the above accuracy evaluation, the repeatability of the method was assessed in terms of the variation of bias parameters when performing the calibration tasks several times.

#### 4.2.3.2. Results

Before discussing the results of the various accuracy evaluations as described before, it is worthwhile to consider the advantage of the proposed algorithm over Hu *et al.*, based on a dataset, which was recorded at a location near the equator. As mentioned before, when being based on inclination information, the scale factor estimation deteriorates significantly as the inclination angle approaches zero degrees. The effect is visible in Figure 4.4, where the measurements calibrated with Hu *et al.* (purple) deviate from the unit sphere, while the measurements calibrated with the proposed method are well aligned. This result demonstrates the independence of the proposed method from its location on Earth and a clear superiority over Hu *et al.* The reason is that in our method biases, scale factors and non-orthogonality parameters are obtained purely from magnetometer measurements based on magnitude information, whereas inclination is only used for the calibration of misalignment.

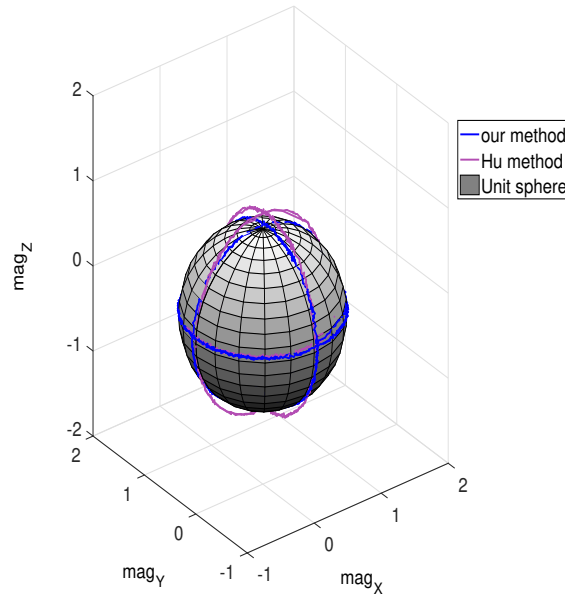


Figure 4.4.: Magnetometer measurements calibrated with our method (blue) and the method of Hu *et al.* (purple). The dataset was sampled in a location close to the equator.

**1. Magnitude deviation** After calibration, the measured magnetic field vectors should have a unit length independent of the IMU pose. The deviation in magnitude from unit length has, therefore, been defined as a measure for accuracy. Figure 4.5 shows the results on a data sequence of 5000 samples, while the IMUs were rotated around different axes. The mean magnitude of our method is 0.99, that of Xsens is 0.98 and that of Hu *et al.* is 1.11. Hence, our method provides comparable results to Xsens and surpasses Hu *et al.* Another useful conclusion that can be drawn from such an experiment is the expected level of magnitude variation, which can be helpful to distinguish valid magnetometer measurements from disturbed outliers in real-time orientation estimation.

**2. Heading error** As mentioned before, heading errors were determined using the test setup of Figure 4.3. After mounting the IMU in the aluminum cube, heading changes of 90 degrees were performed in three different attitudes. Given these known poses, the initial magnetometer vector was rotated accordingly and then compared with the measured vectors. The test conditions were the same for both IMUs and for each pose, the first 100 measurements sampled under static conditions were used. Since it is important to track the heading change in most orientation tracking applications, this test evaluates the change of heading without the need for local heading values as reference. The results are visualized in Figure 4.6. The angular errors in terms of mean and standard deviation (SD) were calculated for each of the three methods. The mean error for our method is  $1.6^\circ$ , which is low in comparison with  $2.07^\circ$  for Xsens and  $1.92^\circ$  for Hu. The SDs were  $0.74^\circ$ ,  $0.79^\circ$ , and  $0.9^\circ$  respectively. This evaluation shows that the head-



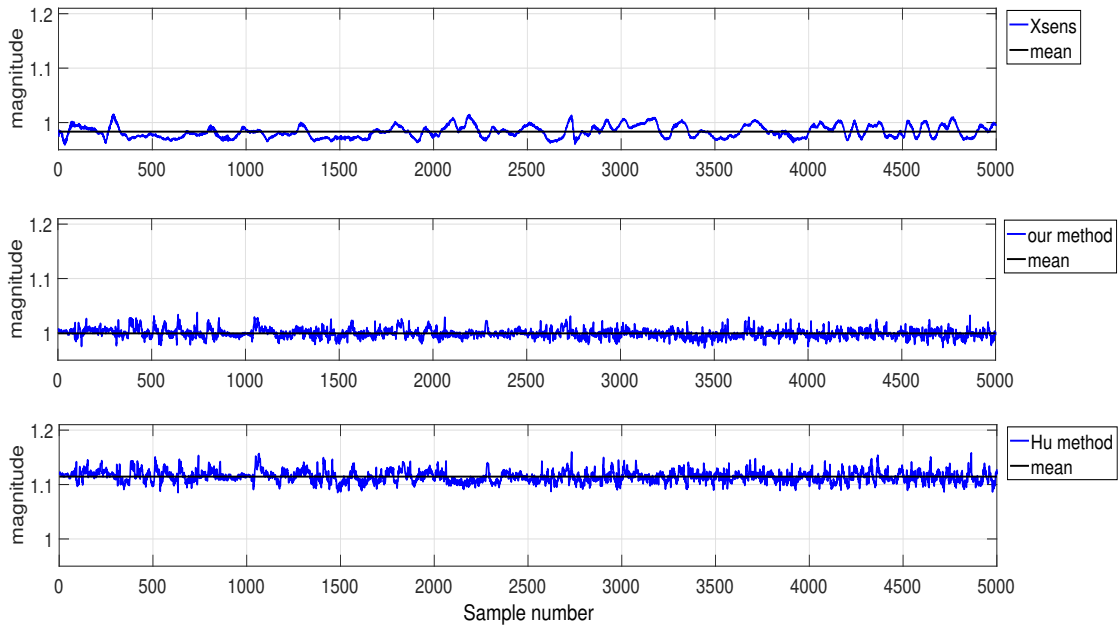


Figure 4.5.: Magnitudes of the magnetic field vectors measured under a wide range of rotations and calibrated with the three methods.

ing angle changes are reliable even when the IMU is tilted  $\pm 90$  degrees in different attitudes because the magnetometer measurements with our method are well-calibrated and aligned with the frame of the IMU.

**3. Plane projections** As a last accuracy test, the IMUs were rotated around the  $x$ -,  $y$ -, and  $z$ -axes and the projections of the calibrated measurements on the three coordinate planes ( $yz$ ,  $xz$ ,  $xy$ ) were examined. The results are shown in Figure 4.7. Ideally, the projected measurements should form a circle with eccentricity zero. Therefore, the error is calculated based on the eccentricity of the ellipses, which are fitted to each set of projected data. For the three data-sets the eccentricity [around  $x$ , around  $y$ , around  $z$ ], calibrated according to our method, is equal to [0.07,0.07,0.07], for Hu equal to [0.16,0.11,0.16], and for Xsens equal to [0.17,0.08,0.14]. Hence, our method provides the most consistent results. This error obviously increases if orthogonality and alignment are not taken into account in the calibration procedure. Since the rotations have been performed on the planes of the aluminum cube, which are assumed to be aligned with the IMU coordinate frame, the result of the projections is not close to the circle, if the axes of the magnetometer are not well-aligned.

**4. Repeatability** To demonstrate the repeatability of our method, we repeated the manual data acquisition procedure and calibration ten times. The percentage of the standard deviation of the biases for the three axes with respect to the range of measurements in these tests was calculated with [0.07, 0.036, 0.35] percent. This shows that variations in the manual data capturing

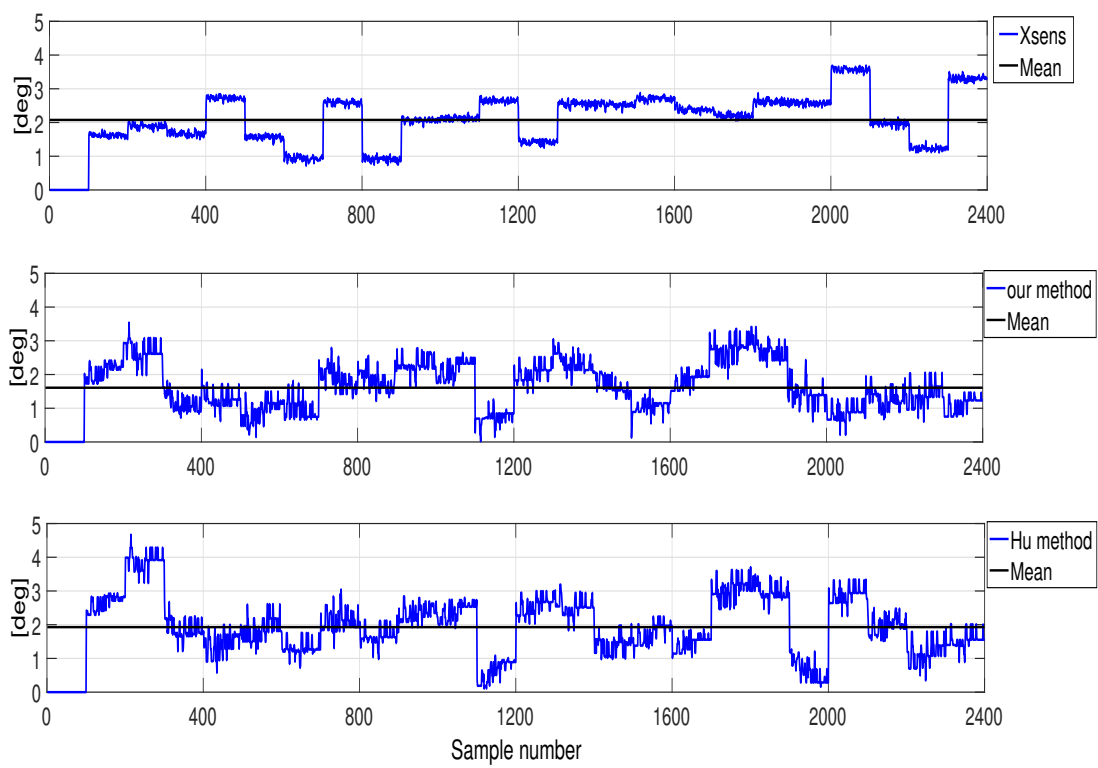


Figure 4.6.: Heading errors resulting from the three calibration methods.

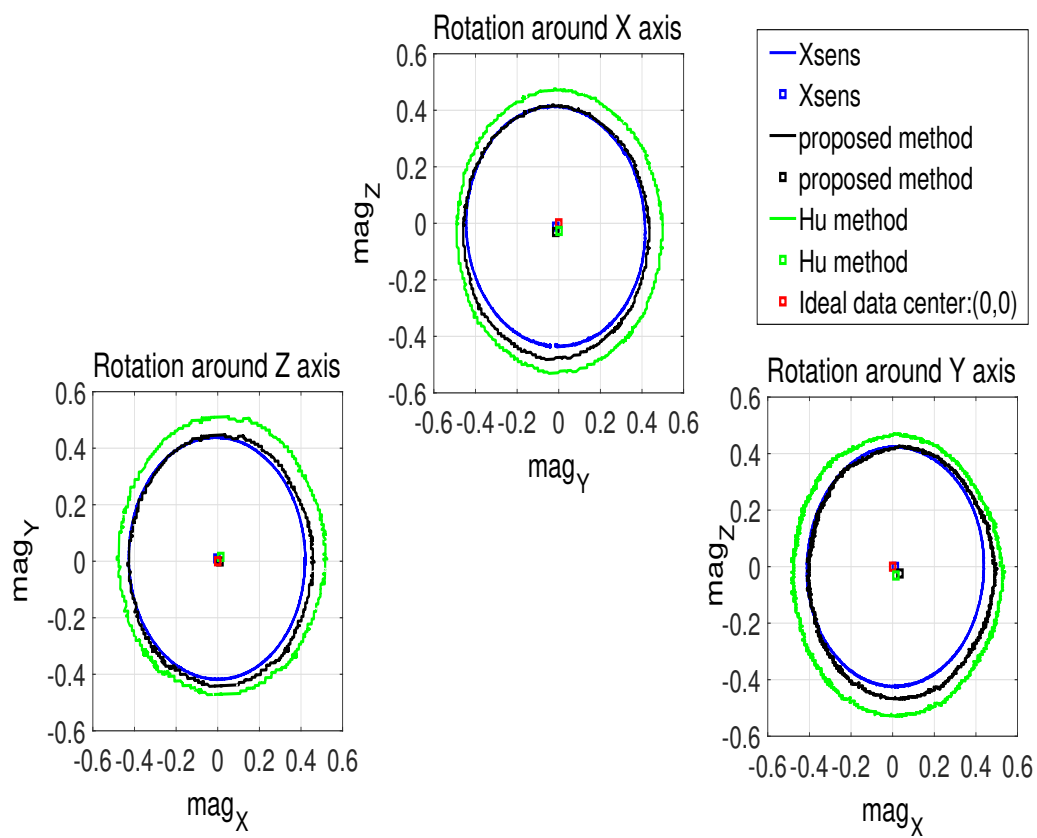


Figure 4.7.: Projection of the calibrated magnetometer measurements on the different coordinate planes using the three calibration methods.

process lead to repeatable calibration parameters. It should be mentioned that in all the measurements for this experiment, almost the entire ellipsoid surface, the locus of magnetometer measurements, was covered with 3,000 samples, which proved to be a suitable number of samples to obtain consistent results. An assessment of how the coverage of measurements affects the number of iterations is presented in [145].

### 4.3. Body-IMU Calibration

At the beginning of this section, the problem of body-IMU calibration is formulated and described. Section 4.3.2 provides a preliminary observability analysis of the method, which is presented in [123]. An additional correction to this method based on [124] is described in Section 4.3.3.

Based on the observability analysis, a new calibration approach is presented in Section 4.3.4 which, in contrast to Seel, considers three linked segments with IMUs (pelvis, upper leg, lower leg) and two joints (hip, knee), respectively, in one estimation problem. This makes it possible to benefit from an additional constraint, which is shown in experiments to provide more robust and accurate results under suboptimal movement conditions (see Section 4.3.9).

#### 4.3.1. Problem formulation

The problem of IMU position estimation can be defined as follows (see Figure 4.8) [124]: Suppose two IMUs,  $A$  and  $B$ , are mounted on two segments connected via a joint  $m$ . Using measurement sequences from  $A$  and  $B$ , the goal is to determine the two IMUs' positions,  $l_{mS}$ ,  $S \in \{A, B\}$ , relative to the joint  $m$ . More precisely,  $l_{mS}$  refers to the vector from the joint center to the IMU center, specified in the local coordinate frame of the IMU. Consider, for instance, the case where  $m$  is the knee joint. Then, IMU  $A$  is placed on the upper leg segment, IMU  $B$  is placed on the lower leg segment, and the goal is to derive the two vectors from the knee joint center to the IMUs in their respective coordinate frames.

For the above problem, an implicit, stochastic measurement model for the timestamp  $i$  can be formulated as:

$$0 = h(x_m, z_{mi}) + e_{mi}, \quad (4.8a)$$

where

$$z_{mi} = [a_{Ai}, a_{Bi}, \omega_{Ai}, \omega_{Bi}, \alpha_{Ai}, \alpha_{Bi}]^T \quad (4.8b)$$

$$x_m = [l_{mA}, l_{mB}]^T. \quad (4.8c)$$

Here,  $z_{mi}$  refers to the measurement vector at timestamp  $i \in 1 \dots k$ . This measurement vector includes 3D acceleration,  $a_{Si}$ , angular velocity,  $\omega_{Si}$ , and angular acceleration,  $\alpha_{Si}$ , of both IMUs,  $S = \{A, B\}$ . Note that  $\alpha_{Si}$  is assumed to be derived from  $\omega_{Si}$ , e.g. via a five-point stencil [81] or estimated together with orientation and angular velocity in an EKF, which is

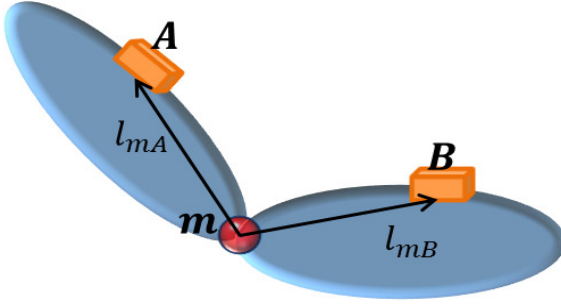


Figure 4.8.: Illustration of the IMU position estimation problem. IMUs  $A$  and  $B$  are mounted on the adjacent segments of the joint  $m$ .

described in detail in Chapter 5. The quantity  $x_m$  refers to the parameter vector comprising the IMU positions. Finally,  $e_{mi} \sim N(0, \Sigma)$  is assumed to be an additive Gaussian measurement noise.

For a given Equation (4.8), a point estimate of  $x_m$  can be obtained by maximizing the maximum likelihood function:

$$\max_x \prod_{i=1 \dots k} P(z_{mi} | x_m). \quad (4.9)$$

Using the logarithm formulation and then eliminating all constant terms from the optimization, this results in a weighted least-squares problem, which can be solved with standard techniques:

$$\min_x \sum_{i=1 \dots k} \|e_{mi}\|_{\Sigma}^2. \quad (4.10)$$

Considering a spheroidal joint, Seel *et al.* introduces the following deterministic measurement model for estimating the IMU positions [123]:

$$e_{mi} = \|a_{Ai} - \Gamma_{Ai}\| - \|a_{Bi} - \Gamma_{Bi}\|, \quad (4.11a)$$

where

$$\Gamma_{Si} = \omega_{Si} \times (\omega_{Si} \times l_{mS}) + \alpha_{Si} \times l_{mS}, \quad (4.11b)$$

and  $e_{mi}$  denotes the residual to be minimized. This model can be directly used in (4.10), even if the latter is reduced to a least-squares formulation due to its deterministic nature.

The following section presents a preliminary observability analysis of the optimization problem (4.10) in combination with the model (4.11), in which we identify major failure cases.

### 4.3.2. Observability analysis

The observability of the general optimization problem in (4.10) can be evaluated by computing the FIM, which can be defined in our setting as derived in Section 2.3.3.2:

$$FIM = J_h^T \Sigma^{-1} J_h. \quad (4.12)$$

Here,  $J_h$  denotes the Jacobian of the measurement model (4.8) in relation to the parameter vector  $x_m$ :

$$J_h = \begin{pmatrix} \frac{\partial e_{m1}}{\partial l_{mA}} & \frac{\partial e_{m1}}{\partial l_{mB}} \\ \vdots & \vdots \\ \frac{\partial e_{mk}}{\partial l_{mA}} & \frac{\partial e_{mk}}{\partial l_{mB}} \end{pmatrix}. \quad (4.13)$$

If  $J_h$  has the full column rank, then  $FIM$  has the full rank [148], which indicates observability.

Using the measurement model (4.11), the partial derivatives in (4.13) for the timestamp  $i$ :

$$\frac{\partial e_{mi}}{\partial l_{mS}} = -\frac{a'_{Si}{}^T}{\|a'_{Si}\|} ([\omega_{Si}]_{\times} [\omega_{Si}]_{\times} + [\alpha_{Si}]_{\times}), S \in \{A, B\}, \quad (4.14)$$

where

$$a'_{Ai} = a_{Ai} - \Gamma_{Ai}, \quad a'_{Bi} = -(a_{Bi} - \Gamma_{Bi}).$$

For simplicity, the timestamp subscript is omitted here, and the following notations are introduced:

$$[\omega_{Si}]_{\times} [\omega_{Si}]_{\times} := W_S = \begin{bmatrix} -(\omega_{Sz}^2 + \omega_{Sy}^2) & \omega_{Sx}\omega_{Sy} & \omega_{Sx}\omega_{Sz} \\ \omega_{Sx}\omega_{Sy} & -(\omega_{Sz}^2 + \omega_{Sx}^2) & \omega_{Sz}\omega_{Sy} \\ \omega_{Sx}\omega_{Sz} & \omega_{Sz}\omega_{Sy} & -(\omega_{Sy}^2 + \omega_{Sx}^2) \end{bmatrix} \quad (4.15a)$$

$$-\frac{a'_{Si}{}^T}{\|a'_{Si}\|} := [\hat{a}_{Sx}, \hat{a}_{Sy}, \hat{a}_{Sz}]^T. \quad (4.15b)$$

By substituting Equation (4.15) into (4.14), we obtain:

$$\frac{\partial e_{mi}}{\partial l_{mS}} = [C_{A1}, C_{A2}, C_{A3}, C_{B1}, C_{B2}, C_{B3}], \quad (4.16)$$

where

$$C_{S1} = \hat{a}_{Sx} W_{S11} + \hat{a}_{Sy} (W_{S12} + \alpha_{Sz}) + \hat{a}_{Sz} (W_{S13} - \alpha_{Sy}) \quad (4.17a)$$

$$C_{S2} = \hat{a}_{Sx} (W_{S21} - \alpha_{Sz}) + \hat{a}_{Sy} W_{S22} + \hat{a}_{Sz} (W_{S23} + \alpha_{Sx}) \quad (4.17b)$$

$$C_{S3} = \hat{a}_{Sx} (W_{S31} + \alpha_y) + \hat{a}_{Sy} (W_{S32} - \alpha_x) + \hat{a}_{Sz} (W_{S33}) \quad (4.17c)$$

with

$$S \in \{A, B\}$$

and  $W_{Spq}$ ,  $p, q \in \{1, 2, 3\}$  refers to the components of  $W_S$ .

Now, to analyze the observability of (4.10), one can examine the situations in which the components in (4.16) are dependent. Considering each IMU (the respective blocks of  $J_h$ ) separately, two cases leading to rank deficiency are:

1. if there is no rotation in at least two DOFs. For instance, assume  $\omega_{Sx} = \omega_{Sy} = 0$  for a sequence of measurements, and consequently  $\alpha_{Sx} = \alpha_{Sy} = 0$ , resulting in  $C_{S3} = 0$ . Then, the third column in the respective block and in the (measurement) rows of  $J_h$  is zero, which reduces the rank. This is the case with the knee joint, since the dominant rotation is flexion/extension, i.e. only in one DOF.
2. When rotation appears with the same angular velocity in three DOFs for a sequence of measurements. In this situation,  $\omega_{Sx} = \omega_{Sy} = \omega_{Sz}$  is in (4.17), which leads to in  $\alpha_{Sx} = \alpha_{Sy} = \alpha_{Sz}$ . By substituting these equalities, the columns in (4.16) are related by  $C_{S1} + C_{S2} + C_{S3} = 0$ .
3. In addition, when considering both IMUs, from (4.16), another case leading to rank deficiency is, when two IMUs rotate with the same angular velocities in all DOFs for a sequence of measurements.

In the case of the hip joint, it is indeed difficult to perform movements with sufficient but different angular velocities in all the DOFs of the pelvis, due to the limited movements of the pelvis. This was explained in detail in Section 2.2. In addition, as discussed in [17], the pelvis rotations are in-phase with the upper leg swings during the relatively high velocities. The similar movements are possible in the calibration phase, as it was visible in our experiments. It is therefore difficult to avoid situations (2) and (3). Note that the movements on the two segments related to a joint should be simultaneous since, otherwise, situation (1) occurs.

### 4.3.3. Seel et al. method with correction using joint axes

As indicated in Section 4.3.1, Seel *et al.* propose a correction of the estimated positions of two IMUs  $B$  and  $C$  in the degenerate case (1) of a hinge joint  $n$  (see Figure 4.9) [124]. In this case, every point on the hinge joint axis  $r_n$  is a solution of (4.11). The correction of the estimated vectors,  $l_{nS}$ ,  $S \in \{B, C\}$  corresponds to a shift of the joint center,  $n$ , on the known joint rotation axes,  $r_{nS}$ ,  $S \in B, C$ , as represented in the coordinate frames of both IMUs. The shift computation is based on the assumption that the true joint center is the point on the joint axis that is closest to both IMUs. This can be formalized as:

$${}^S e_{nCoR} = \frac{1}{2}(r_{nB}^T \cdot l_{nB} + r_{nC}^T \cdot l_{nC})r_{nS}, \quad S \in \{B, C\}, \quad (4.18)$$

where  ${}^S e_{nCoR}$  denotes the shift of the joint center of rotation (COR) represented in the local coordinate frame of  $S$ . The left superscript indicates the latter. Moreover,  $r_{nS}$ ,  $S \in B, C$  are

assumed to be known by calibration [124]. The corrected IMU positions are then:

$$l'_{nB} = l_{nB} - {}^B e_{nC \circ R}, \quad l'_{nC} = l_{nC} - {}^C e_{nC \circ R}. \quad (4.19)$$

The above correction method was included in the experimental evaluation in Section 4.3.9.

#### 4.3.4. Proposed method

The previous section describes different cases of movements, which can lead to inaccurate results, when applying the IMU position calibration method of [124] to the hip and knee joint. Therefore, this section proposes a novel method, which improves upon the existing one through the following extensions:

The estimation of the positions  $x = [x_m, x_n]^T$  of the three IMUs  $S \in \{A, B, C\}$  (on the pelvis, upper leg, lower leg) with respect to the two joints  $m, n$  (hip, knee) (see Figure 4.9), from the IMU measurements  $z = [z_m, z_n]^T$  is modeled jointly in one optimization problem analogous to Equation (4.10), but with a new measurement model, which is introduced in the following.  $S = \{A, B, C\}$ ,  $z = \{z_m, z_n\}$ , and  $x = \{x_m, x_n\}$ , which are estimated with an estimator similar to Equation (4.10) reformulated in Equation (4.20).

$$\hat{x}^{LSE} = \arg \min_x (e_i^T \Sigma_z^{-1} e_i), \quad (4.20)$$

in which

$$e_i = \begin{bmatrix} e_{mi} \\ e_{ni} \\ e_{mni} \end{bmatrix}, \quad \Sigma_z = \begin{bmatrix} \Sigma_{z_m} & 0 \\ 0 & \Sigma_{z_n} \end{bmatrix}$$

The components in  $e_i$  will be explained in Sections 4.3.6 and 4.3.7. Although the contribution here focuses on IMU position calibration, since the joint rotation axes and a preliminary estimate of joint angles are critical for the proposed algorithm here, as well as in the following chapter, the next section describes a method for estimating such parameters.

#### 4.3.5. Joint Rotation Axis and Angle Estimation

Considering a hinge joint such as  $n$  (see Figure 4.9), the measurements of gyroscopes mounted on the two adjacent segments provide useful information to identify the joint axis  $\vec{r}_n$ . Since the rotation is limited to only one direction, i.e. the joint axis, any difference between the angular velocities of the two segments in the plane perpendicular to the rotation contrary to this limited degree of freedom. It is also obvious that the difference between the angular velocities of the segments in the direction of the joint axis is the joint angular velocity. These facts are defined in the Equations (4.21) and (4.22) for each timestamp  $i$  during the rotation.

$$\|\vec{\omega}_{Bi} \times {}^B \vec{r}_n\| - \|\vec{\omega}_{Ci} \times {}^C \vec{r}_n\| = 0 \quad (4.21)$$

$$\dot{\theta}_n = \vec{\omega}_{Bi} \cdot {}^B \vec{r}_n - \vec{\omega}_{Ci} \cdot {}^C \vec{r}_n \quad (4.22)$$



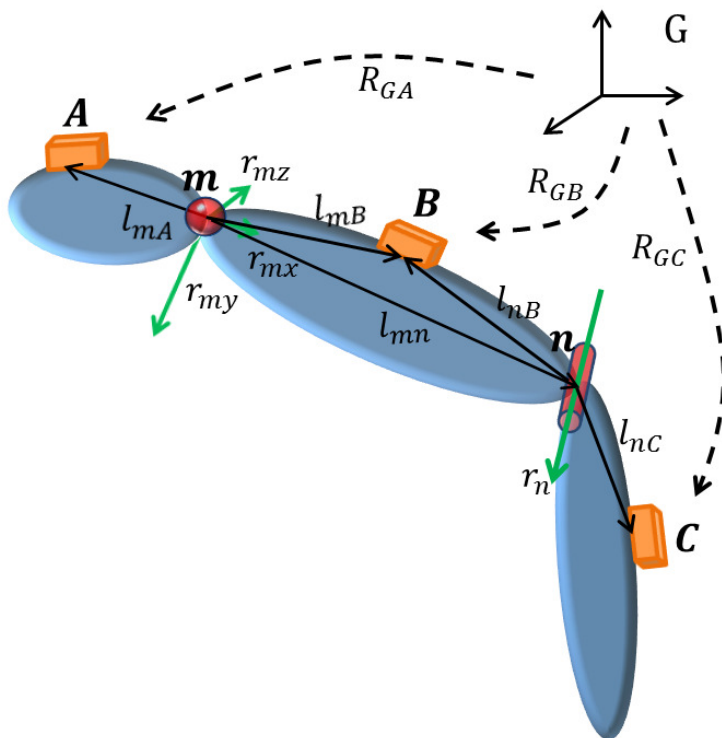


Figure 4.9.: Illustration of the IMU position estimation problem specifically addressing the lower body. The spheroidal joint  $n$  refers to the hip (three rotation axes:  $r_{mx}$ ,  $r_{my}$ , and  $r_{mz}$ ), and the hinge joint  $n$  refers to the knee (one rotation axis:  $r_n$ ). The two joints are linked via the upper leg segment, with a fixed length of  $l_{mn}$ . The IMUs  $A$ ,  $B$ ,  $C$  are mounted on the segments connected through the hip and knee joints. They are placed on the pelvis, upper leg, and lower leg, respectively. The quantities  $l_{mA}$ ,  $l_{mB}$ ,  $l_{nB}$ ,  $l_{nC}$  are the IMU position vectors to be estimated.  $R_{GA}$ ,  $R_{GB}$ ,  $R_{GC}$  are the orientations of the IMU with respect to the global coordinate frame  $G$ .

Thus, in an optimization problem with Equation (4.21) as a cost function, the joint axis can be estimated using a set of measurements from two gyroscopes on the segments of a joint. The change in joint angle is obtained from the integration of (4.22). Though these facts are explained for the knee joint, the same could be true for hip if, during the Body-IMU calibration, movements on the joint are limited to only one of flexion/extension, abduction/adduction or internal/external rotations for the respective DOF.

#### 4.3.6. Proposed measurement model

First, instead of considering only the lengths of the acceleration vectors in Equation (4.11), the proposed stochastic measurement model takes into account the relative orientations of the IMUs, leading to:

$$0 = a'_{Ai} + R_{ABi}a'_{Bi} + e_{mi} \quad (4.23a)$$

$$0 = a'_{Ci} + R_{CBi}a'_{Bi} + e_{ni}, \quad (4.23b)$$

where  $[e_{mi}, e_{ni}]^T \sim N(0, \Sigma)$  and the relative rotation  $R_{YX}$  from  $X$  to  $Y$  can be obtained as  $R_{YX} = R_{GY}^T R_{GX}$ . Here,  $R_{SG}, S \in \{X, Y\}$  is the orientation of IMU  $S$  with respect to a fixed global frame  $G$ , which is typically aligned with gravity and magnetic north. The global orientations are estimated using an EKF (see Chapter 5). However, since the movements required for the calibration could be defined as specific rotations in each DOF of each joint, an alternative to calculating the relative rotation  $R_{AB}$  at the timestamp  $i$  is to apply the method in Section 4.3.5 and the first estimated orientations of the two adjacent segments in one of the following equations:

$$R_{A_i B_1} = R_{A_1 A_i}^T R_{A_1 G} R_{B_1 G}^T \quad (4.24a)$$

$$R_{A_1 B_i} = R_{A_1 G} R_{B_1 G}^T R_{B_i B_1}^T, \quad (4.24b)$$

where  $R_{S_1 S_i} = Rot(\theta), S \in \{A, B\}$  and  $\theta$  is the change in the joint angle, which can be calculated from the method in Section 4.3.5. The same approach can be used to calculate the relative rotation  $R_{BC}$ . This is a preliminary estimate of joint angle as it exhibits a slow drift caused by integration of bias inherent in gyroscope measurements. However, the accuracy is sufficient for the current estimation problem compared to using the global orientations, as shown in the experimental results, Section 4.3.9.2.

#### 4.3.7. Constraints of three connected segments

The hip and knee are considered together in an optimization problem. This allows the extension of the measurement models in (4.23) with additional constraints modeling the fact that these joints,  $m, n$  in Figure 4.9, are linked via the upper leg segment  $l_{mn}$ . We assume the flexion/extension joint axes of the hip and knee,  $r_{my}$  and  $r_n$ , as being approximately coplanar. Moreover, they intersect with each other due to the natural misalignment of knee joint axis and the mechanical axis of the lower body, as described in Section 2.2. In Figure 4.10 (upper), the geometry is illustrated for an ideal coplanar case with intersecting axes, where the latter span

the plane  $P_1$  with the normal vector  $n_{P1}$ . Furthermore,  $l_{mB}$  and  $l_{nB}$  are, by definition, coplanar, spanning the plane  $P_2$  with the normal vector  $n_{P2}$ . Assuming that  $r_{my}$  and  $r_n$  are not parallel, the normal vectors can be obtained using cross products:

$$n_{P1} = r_{my} \times r_n \quad (4.25a)$$

$$n_{P2} = l_{mB} \times l_{nB}. \quad (4.25b)$$

As is visible in the figure, in the ideal case,  $P_1$  and  $P_2$  intersect at a line  $l_{P12} := n_{P1} \times n_{P2}$ , which is parallel to  $l_{mn} = l_{mB} - l_{nB}$ . Moreover,  $n_{P1}$ , which is perpendicular to  $l_{P12}$ , is also perpendicular to  $l_{mn}$ . These facts can be formalized, which leads to the following constraints:

$$0 = (l_{mn} \times l_{P12}) + e_{mn1} \quad (4.26a)$$

$$0 = (n_{P1}^T \cdot l_{mn}) + e_{mn2}, \quad (4.26b)$$

where  $e_{mn1}$  and  $e_{mn2}$  account for the fact that the assumed coplanarity of  $r_{my}$ ,  $r_n$ , and  $l_{mn}$  is an approximation (see Figure 4.10). In a real setup, For the case that  $r_{my}$  and  $r_n$  are skew, see Figure 4.10(lower), we can still define a plane consisting of one of them and a vector parallel to the other, which is coplanar with the first one. Since  $r_{my}$  and  $r_n$  are pointing almost in the same direction, the new plane has a very small angle, with  $l_{mn}$ . By an approximation, the same constraints in Equation (4.26) can be applied.

### 4.3.8. Observability analysis of proposed method

Note that when combining (4.23) with (4.26), the respective Jacobian for one timestep  $i$  is:

$$J_{hi} = \begin{bmatrix} \frac{\partial e_{mi}}{\partial l_{mA}} & \frac{\partial e_{mi}}{\partial l_{mB}} & 0_{3 \times 3} & 0_{3 \times 3} \\ 0_{3 \times 3} & 0_{3 \times 3} & \frac{\partial e_{ni}}{\partial l_{nB}} & \frac{\partial e_{ni}}{\partial l_{nC}} \\ 0_{3 \times 3} & \frac{\partial e_{mn1i}}{\partial l_{mB}} & \frac{\partial e_{mn1i}}{\partial l_{nB}} & 0_{3 \times 3} \\ 0_{1 \times 3} & \frac{\partial e_{mn2i}}{\partial l_{mB}} & \frac{\partial e_{mn2i}}{\partial l_{nB}} & 0_{1 \times 3} \end{bmatrix} \quad (4.27a)$$

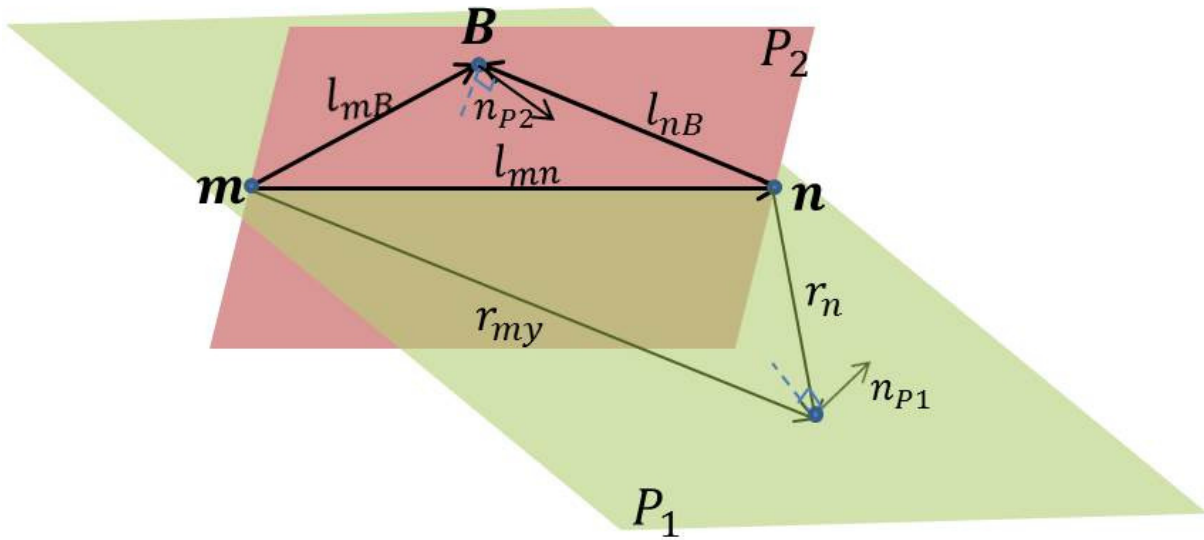
where

$$\frac{\partial e_{mn1i}}{\partial l_{mB}} = [l_{P12}]_{\times}^T + l_{mn} \times ([l_{nB}]_{\times}^T n_{P2}), \quad (4.27b)$$

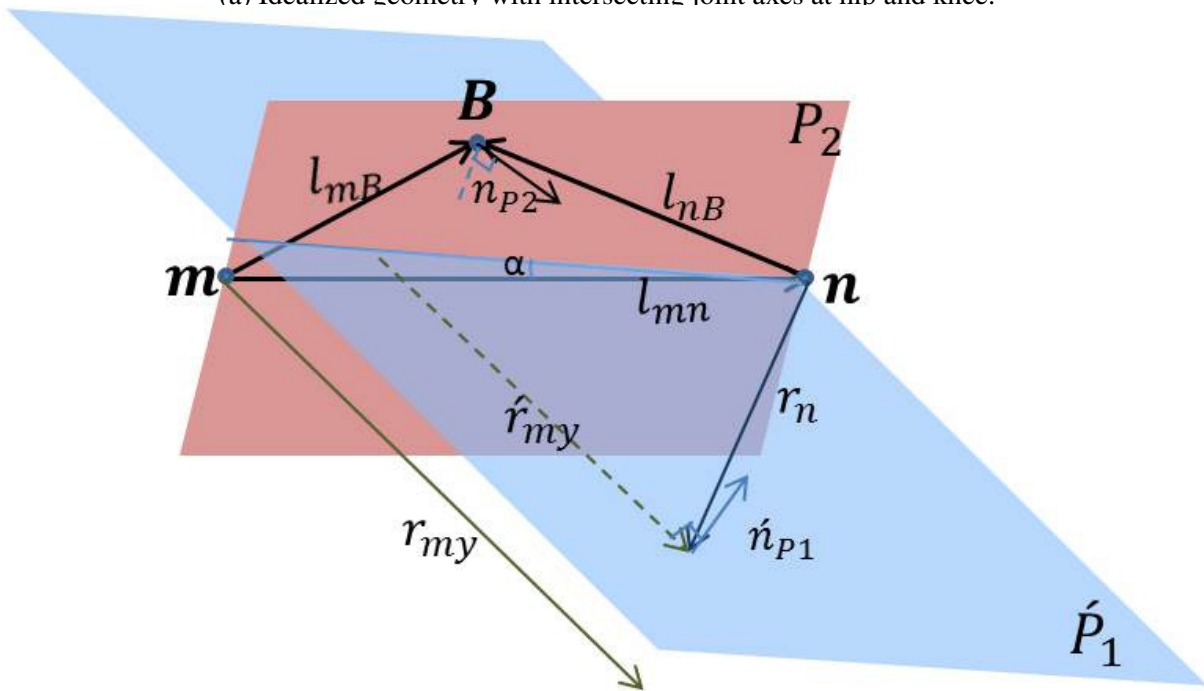
$$\frac{\partial e_{mn1i}}{\partial l_{nB}} = -[l_{P12}]_{\times}^T + l_{mn} \times ([l_{mB}]_{\times}^T n_{P2}), \quad (4.27c)$$

$$\frac{\partial e_{mn2i}}{\partial l_{mB}} = n_{P1}, \quad (4.27d)$$

$$\frac{\partial e_{mn2i}}{\partial l_{nB}} = -n_{P1} \quad (4.27e)$$



(a) Idealized geometry with intersecting joint axes at hip and knee.



(b) Realistic geometry with skew joint axes.

Figure 4.10.: Illustration of the constraints formulated in (4.26): The upper figure shows the idealized geometry, which is the basis for the constraints. It approximates the more realistic setup in the lower figure with skew joint axes, leading to the plane  $\hat{P}_1$ . The latter can be assumed to have a small angle  $\alpha$  with respect to the ideal plane  $P_1$ .

and  $\frac{\partial e_{ni}}{\partial l_{nS}}$  is computed similarly to (4.14). When considering the second and third block of  $J_{hi}$ , it can be seen that the rank depends is not only on the angular velocities but also on the relative position vectors, as well as the joint rotation axes. This results in a more complex expression, which is difficult to simplify. The rank of the first and last three columns can still be reduced, as discussed in Section 4.3.2. However, by incorporating the constraint on  $l_{mB}$ , both the error  $e_{mi}$  and the estimation error of  $l_{mA}$  are assumed to be reduced.

Figure 4.11 illustrates the data flow between different components of the proposed method.

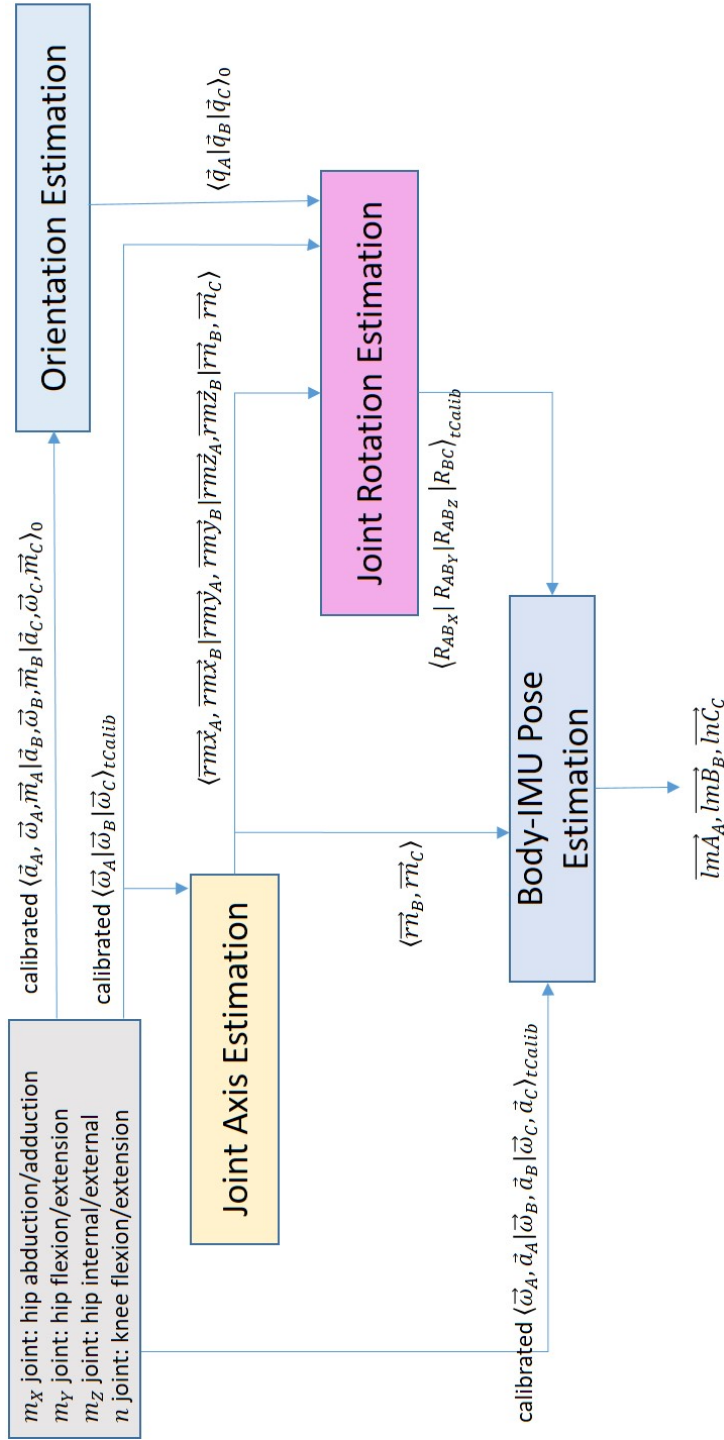


Figure 4.11.: The proposed autocalibration method.

	Type 1	Type 2
rad/s	[12, 13, 23]	[12, 13, 23]
A	[0.56, 0.51, 0.13]	[3.45, 5.43, 1.67]
B	[0.8, 0.53, 2.6]	[3.62, 6.05, 7.29]
C	[3.18, 1.56, 3.7]	[7.89, 10.94, 13.38]

Table 4.1.: The angular velocity variations for the simulated IMU measurements: 12 represents the variation between the first and the second DOF for each IMU A, B, C. Each number expresses the mean of squared differences between the simulated angular velocities for all the timesteps.

### 4.3.9. Experimental results

#### 4.3.9.1. Synthetic data

Different IMU position calibration methods (Seel *et al.* and the proposed one) were first evaluated using noisy synthetic measurements simulated at  $100Hz$  for setup, as illustrated in Figure 4.9. To obtain sufficient variations of the input data for the optimization problem, the measurements were downsampled to  $10Hz$ . The simulator output comprises a 3D accelerometer, gyroscope, and magnetometer measurements as well as the global orientations of each segment with respect to a fixed reference frame  $G$ . These values are calculated based on the inputs to the simulator, which include joint angles (generated from sine functions with different scales in each DOF), IMU to body poses, and also measurement noise specifications comparable to those of the IMUs used in the real data tests listed below.

To evaluate the accuracy and robustness of different methods for different types of movements, two sets of joint angle sequences were simulated, each with 100 randomly generated IMU to body poses: Type 1 provides low variations among the DOFs of each segment, whereas the knee joint is modeled with one DOF. This resembles a natural calibration movement. Type 2 provides high variations among the DOFs and additionally models both joints with three DOFs. Hence, the type 1 set provides more realistic but suboptimal movement conditions, whereas the type 2 set is expected to work well with both calibration methods. In order to extract the joint rotation axes required in (4.25), the movements, in which each segment rotates in all possible DOFs separately, were produced. Further details about the simulated joint trajectories in relation to the resulting angular velocity variations are given in Table 4.1.

The proposed method and the method of Seel *et al.* were implemented in Matlab using *lsqnonlin* with the LMA. In the following, the behavior of these methods is evaluated through several experiments.

The effect of introducing only relative IMU orientations, as formalized in Equation (4.23) without coupling, the two estimation problems are illustrated in Figure 4.12, where the root mean squared error (RMSE) for the estimated IMU positions is provided for ten different mounting orientations using type 2 trajectories. This shows already an improvement of the proposed method concerning accuracy and robustness under optimal movement conditions.

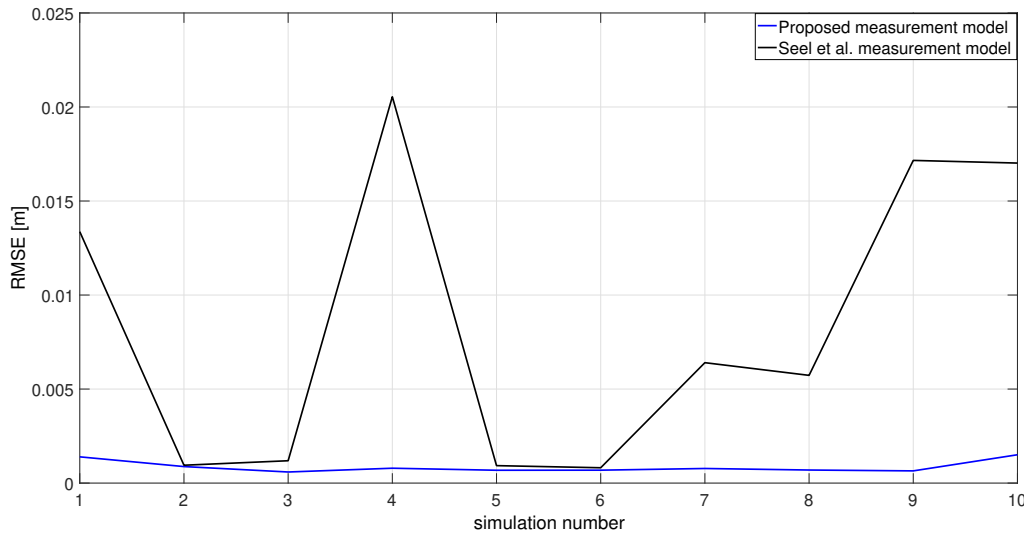


Figure 4.12.: RMSE for ten different IMU mounting orientations when applying the measurement model defined in (4.23) to type 2 movements.

Figure 4.13 illustrates the RMSE when applying the different calibration methods to the two different types of movements. Here, the proposed method also includes the constraint introduced in Section 4.3.7. The results show that higher motion variations during calibration improve the performance of both algorithms. However, with fewer variations, our proposed method outperforms the ones of Seel *et al.* As the correction related to that method which is described in Section 4.3.3 resulted worse than the original in some cases, especially in the type 2 movements; they both are presented in Figure 4.13.

Moreover, the convergence of both calibration methods was tested using 100 random initial values. Figure 4.14 presents the results of this test for measurements simulated from one IMU to body configuration. This shows that the two methods are generally not sensitive to the initial values. Nevertheless, for type 2 trajectories, both methods converge to similar results, with less than 1 *cm* error. However, our proposed method converges faster. For suboptimal type 1 trajectories, the method of Seel *et al.* converges with a large error of 61 *cm*, while our proposed method converges with only 3 *cm* error.

#### 4.3.9.2. Real data

To evaluate the proposed method on real measurements, a dataset was recorded from 7 subjects, 2 women and 5 men, who each performed 3 trials using a prototype wearable system described in Chapter 3 and an optical reference system, the NaturalPoint OptiTrack system with 12 Prime 13 cameras, operated with Motive software [95]. The experimental setup is shown in Figure 4.15.

To obtain the IMU poses, each IMU was rigidly connected to a rigid body marker. The IMUs were interconnected via textile cables. In order to reduce artifacts due to movement of the garment, the IMU-marker-sets were strapped firmly on the pelvis and one leg. We also used straps



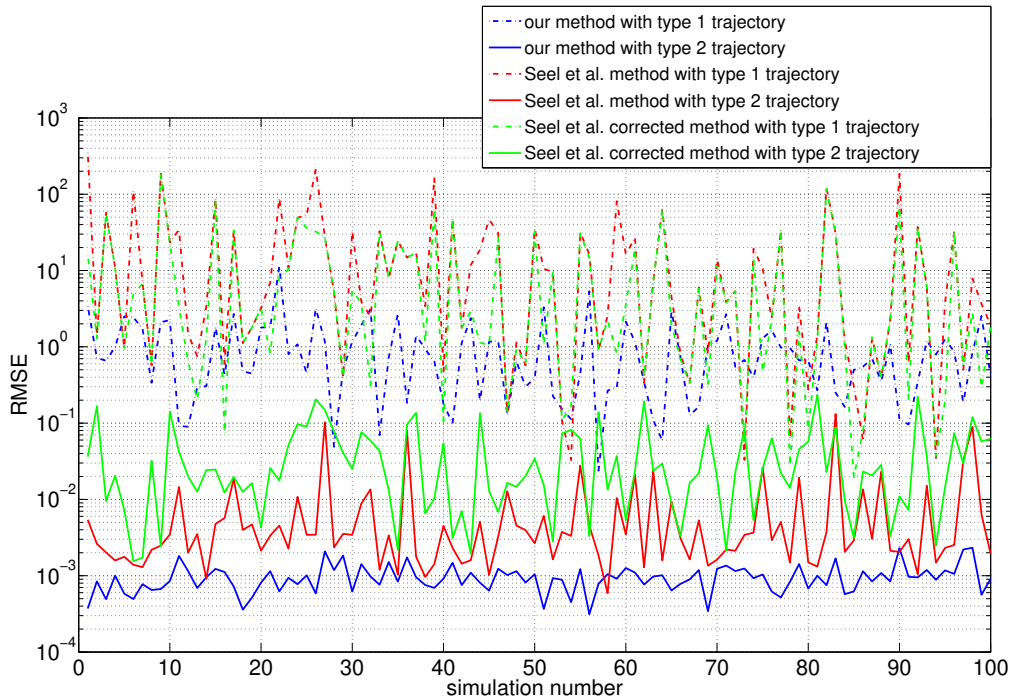


Figure 4.13.: RMSE for 100 different IMU to body configurations when using the measurement model defined in (4.23) and the additional constraint in (4.26).

to attach marker clusters on anatomical landmarks around the hip and knee joints, from which we determined the joint CoRs.

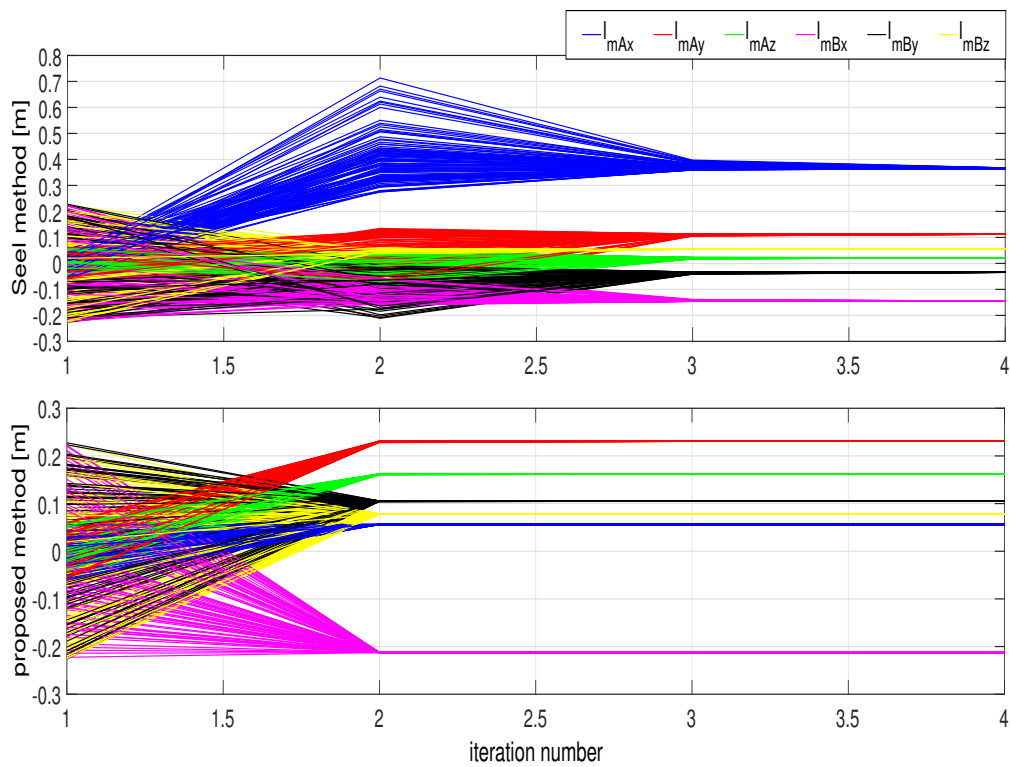
In each trial, the subjects performed movements of types A and B. In order to assess the repeatability of the process, each subject carried out three trials. Data is captured in both optical systems and IMUs with a frequency of  $50\text{Hz}$ . The IMU measurements were then downsampled to  $5\text{Hz}$  to be used for optimization in both calibration methods.

A hand-eye calibration was performed to transform the coordinates of the optical system into the IMU coordinates. Note that errors due to marker positioning are present, however, similarly for all the tested methods. The data from type B movements was first used to estimate the axes of the joints by applying the method described in Section 4.3.5.

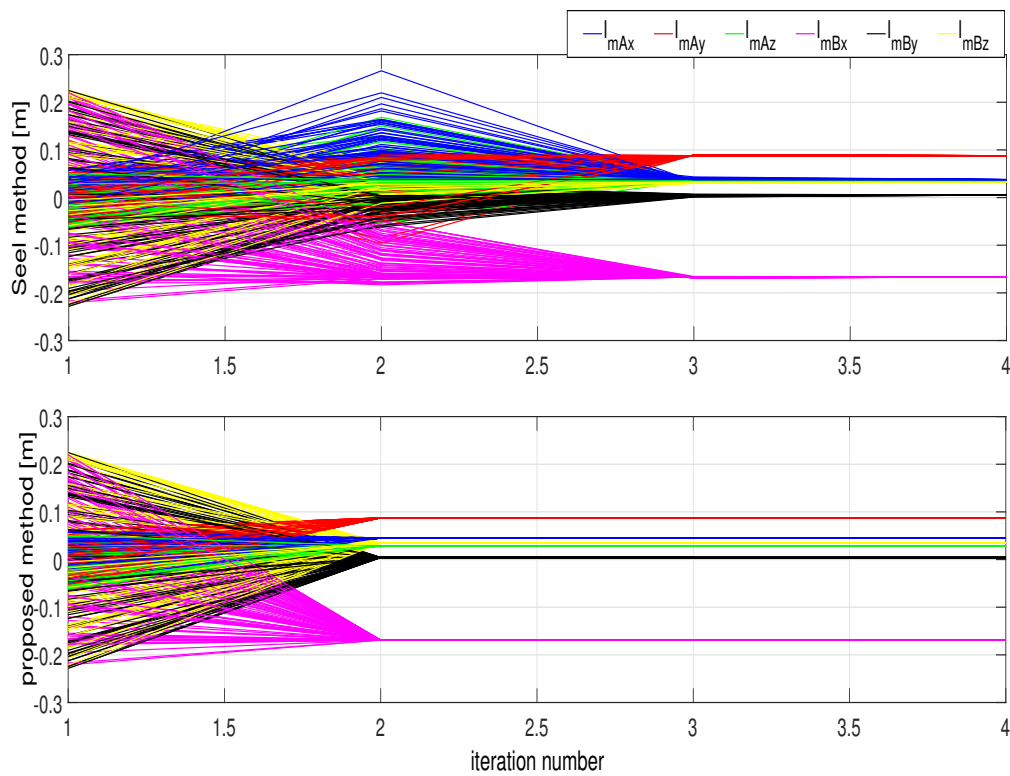
The calibration algorithms were applied to both types of data. The the process for each one is described below:

#### A. Calibration with random movements in all directions

The variations of the resulting angular velocity for the random movements in all the trials are presented in Tables 4.2, 4.3, and 4.4, and show that the real data correspond to simulated type 1 movements for IMU A, which verifies the simulation of suboptimal movements of pelvis. For IMUs B and C, however, the variations are higher and thus more similar to type 2. These variations and their relation to the observability conditions are analysed in detail in Section 4.3.9.4.



(a) Type 1 trajectory



(b) Type 2 trajectory

Figure 4.14.: Convergence test with 100 random initial values for the IMU position. In this test the true value of  $l_{m_A}$  is  $[0.05, 0.09, 0.03]$  and the true value of  $l_{m_B}$  is  $[-0.17, 0.004, 0.03]$ .



Figure 4.15.: Test setup. The red arrows show three IMUs which are mounted on 1.pelvis (not visible), 2.upper leg and 3.lower leg

The global IMU orientations required in Equation (4.23) have been calculated using the method described in Section 5.1.2. The estimated IMU position vectors were then compared with the reference vectors calculated from the positions of the optical markers. Figure 4.16 illustrates the overall RMSE in all the four segments for all trials when applying the different calibration methods to the real measurements. It shows that the proposed method provides more accurate or comparable results in 80% of the trials, while a slightly worse performance can be observed in four of the trials. The average error over all trials is  $16.9 \pm 0.8\text{cm}$  (mean  $\pm$  SD) for the proposed method, which is lower than that of the Seel *et al.* method with an error of  $18.13 \pm 0.7\text{cm}$ .

A more detailed evaluation can be made on the basis of the error in relation to each segment. This is shown in Tables 4.5 and 4.6. It can be observed that the errors of both methods in segments  $l_{mA}$  and  $l_{mB}$  are higher than the ones in  $l_{nB}$  and  $l_{nC}$ , as the movements of these segments around the hip joint are more limited than the ones around the knee. This was theoretically proven in the Observability analysis Section 4.3.2, conditions 2 and 3, which refer to the angular velocity variation (see Table 4.1). Nevertheless, due to additional constraints, the proposed method performs better; the average error over all the trials for  $l_{mA}$  and  $l_{mB}$  in the Seel *et al.* method are respectively  $17.1 \pm 1.7$  and  $26.0 \pm 1.6\text{cm}$ , while these errors are  $15.4 \pm 1.4$  and  $24.5 \pm 1.9\text{cm}$ , in the proposed method.

On the other hand, the errors in Seel *et al.* method related to knee adjacent segments  $l_{nB}$  and  $l_{nC}$  are  $12.6 \pm 1.4$ ,  $11.5 \pm 1.5\text{cm}$ , and in the proposed method,  $10.7 \pm 1.7$ ,  $12.1 \pm 1.5\text{cm}$ , which are much better than those for the adjacent segments of the hip.

	subj. 1	subj. 2	subj. 3	subj. 4	subj. 5	subj. 6	subj. 7
rad/s	[12, 13, 23]	[12, 13, 23]	[12, 13, 23]	[12, 13, 23]	[12, 13, 23]	[12, 13, 23]	[12, 13, 23]
A	[2.6, 1.1, 3.3]	[3.7, 1.8, 4.5]	[1.5, 0.7, 0.6]	[2.5, 1.3, 1.1]	[3.2, 1.6, 3.8]	[0.7, 0.4, 1.2]	[1.3, 1.7, 1.5]
B	[4.2, 2.1, 3.4]	[4.9, 2.1, 2.8]	[6.3, 2.9, 2.2]	[5.8, 2.6, 7.9]	[15.4, 6.9, 8.1]	[3.8, 2.2, 2.4]	[9.6, 4.8, 3.9]
C	[6.7, 4.2, 10.5]	[5.5, 8.8, 12.6]	[6.5, 8.1, 5.9]	[15.1, 10.5, 8.4]	[14.4, 12.1, 10.2]	[3.9, 4.7, 4.1]	[10.4, 4.5, 14.1]

Table 4.2.: The angular velocity variations for the movements in the first calibration trial. See Table 4.1 for more details.

	subj. 1	subj. 2	subj. 3	subj. 4	subj. 5	subj. 6	subj. 7
rad/s	[12, 13, 23]	[12, 13, 23]	[12, 13, 23]	[12, 13, 23]	[12, 13, 23]	[12, 13, 23]	[12, 13, 23]
A	[2.8, 1.5, 3.9]	[1.8, 1.6, 1.2]	[3.0, 0.8, 1.5]	[0.7, 0.9, 1.1]	[0.5, 0.2, 0.6]	[1.0, 1.1, 0.7]	[2.5, 2.4, 1.3]
B	[4.9, 1.4, 2.9]	[17.7, 15.0, 2.7]	[4.6, 3.0, 1.8]	[4.2, 3.1, 4.6]	[2.8, 1.2, 2.3]	[8.3, 5.0, 4.4]	[10.0, 6.6, 4.2]
C	[5.4, 5.1, 10.6]	[22.5, 0.1, 6.4]	[14.5, 10.7, 8.7]	[3.2, 2.6, 3.2]	[2.0, 4.0, 2.6]	[3.4, 5.0, 5.4]	[9.2, 3.2, 10.0]

Table 4.3.: The angular velocity variations for the movements in the second calibration trial. See Table 4.1 for more details.

	subj. 1	subj. 2	subj. 3	subj. 4	subj. 5	subj. 6	subj. 7
rad/s	[12, 13, 23]	[12, 13, 23]	[12, 13, 23]	[12, 13, 23]	[12, 13, 23]	[12, 13, 23]	[12, 13, 23]
A	[2.6, 1.5, 2.9]	[1.9, 2.6, 1.3]	[4.5, 1.2, 1.5]	[1.8, 0.8, 2.4]	[0.5, 0.4, 0.6]	[0.8, 1.2, 1.9]	[2.2, 0.8, 2.3]
B	[3.9, 1.6, 2.8]	[14.3, 6.1, 4.5]	[11.0, 4.4, 14.8]	[9.7, 2.7, 6.2]	[2.8, 3.5, 1.7]	[9.1, 9.6, 2.9]	[5.4, 3.6, 5.1]
C	[5.1, 7.1, 11.2]	[2.2, 6.7, 4.7]	[11.9, 15.1, 13.0]	[10.3, 9.5, 5.6]	[3.7, 4.4, 3.2]	[10.3, 5.2, 3.5]	[6.9, 10.0, 6.0]

Table 4.4.: The angular velocity variations for the movements in the third calibration trial. See Table 4.1 for more details.

### B. Calibration with separate movements on each DOF

To estimate the relative orientations of the segments here, the method in Section 4.3.5 is used. Figure 4.17 illustrates the overall RMSE in all the four segments for all trials, showing that the proposed method gives more accurate results with an average error of  $15.1 \pm 0.6 \text{ cm}$ . The average error for the segment  $l_{mB}$  is  $18.7 \pm 2.0 \text{ cm}$ , which is  $6 \text{ cm}$  less than in the first experiment. This error for other segments differs only by about  $1 \text{ cm}$  when comparing the experiments with type A and type B movements. The detailed result is presented for the Seel *et al.* method in Table 4.7 and the proposed method in Table 4.8.

The results of the above experiments show that the proposed method performs better in experiments with type B movement, while method proposed by Seel *et al.* performs worse than with type A. This proves experimentally the first condition of observability, which is discussed in Section 4.3.2. Moreover, during the random movements experiment, the subjects have performed fast and hardly controlled movements to excite all the segments simultaneously. This led to a high deviation of accelerometer measurements from gravity (see Figure 4.18). In the orientation estimation filters (see Section 5.1.2), these measurements are usually considered as outliers, and the estimated orientation in the presence of such measurements is prone to error. This results in a higher error in the proposed method when such measurements are used as input. However, this is not the problem for the proposed relative orientation estimation method in Section 4.3.6 since the accelerometer measurements are not necessary. In addition, because the subjects concentrate on only one DOF, they perform more controlled movements. Therefore, the assumption of the hinge joint type in Section 4.3.6 is relatively accurate.

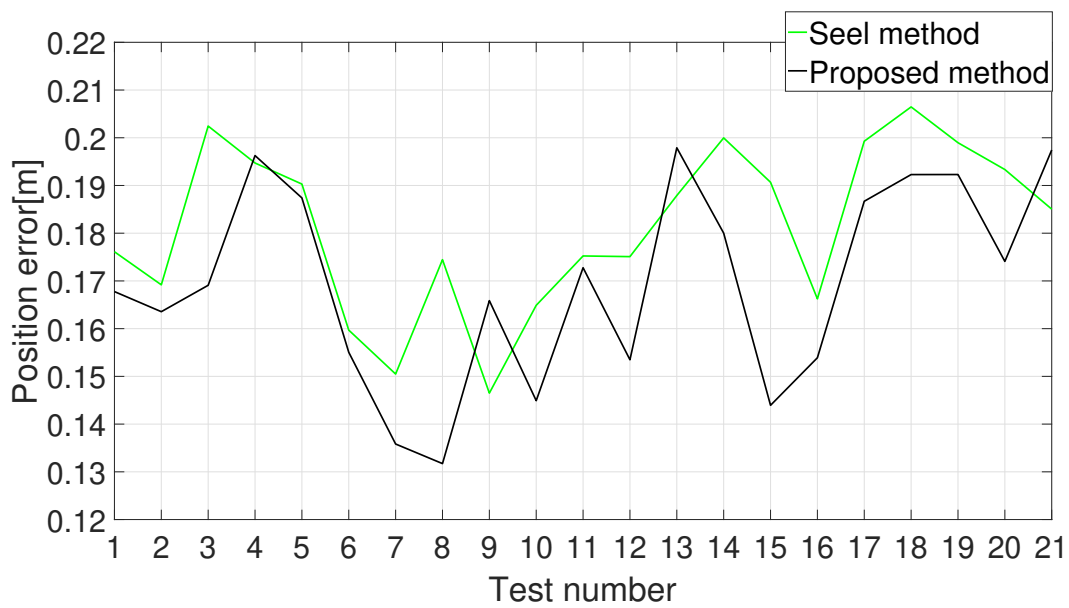


Figure 4.16.: Results on real measurements from random movements: RMSE of the Body-IMU calibration using Seel *et al.* and the proposed method, with respect to optical tracker.

In the diagram test number of all the trials are ordered from 1 to 21 which means the first 3 are related to the trials performed by subject 1, the second 3 are related to subject 2, and so on

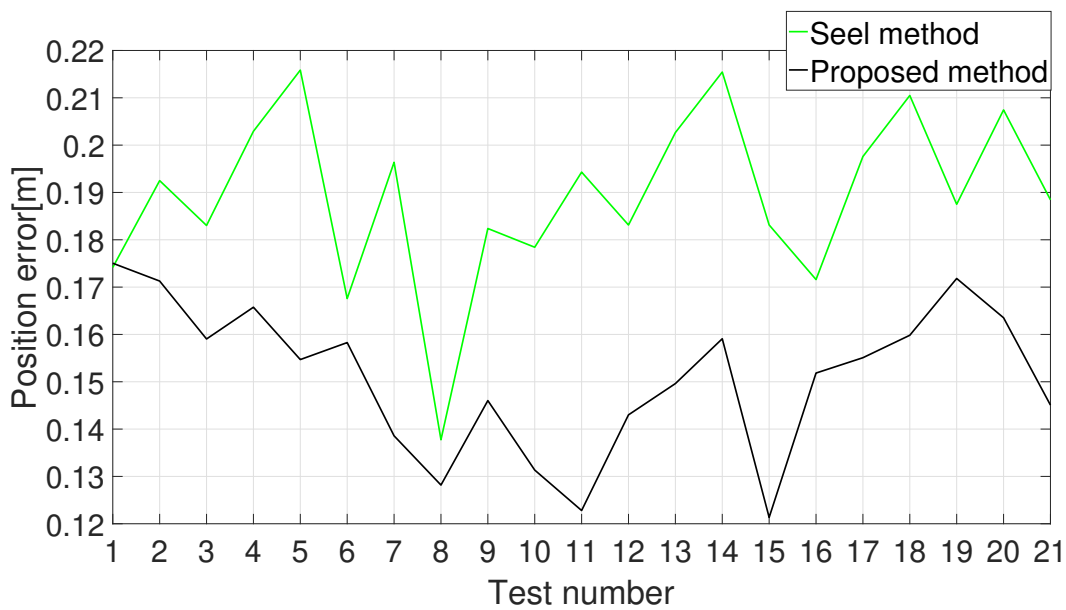


Figure 4.17.: Results on real measurements from the movements on each DOF separately: RMSE of the body-IMU calibration using Seel *et al.* and the proposed method, with respect to optical tracker.

In the diagram test number of all the trials are ordered from 1 to 21 which means the first 3 are related to the trials performed by subject 1, the second 3 are related to subject 2, and so on.



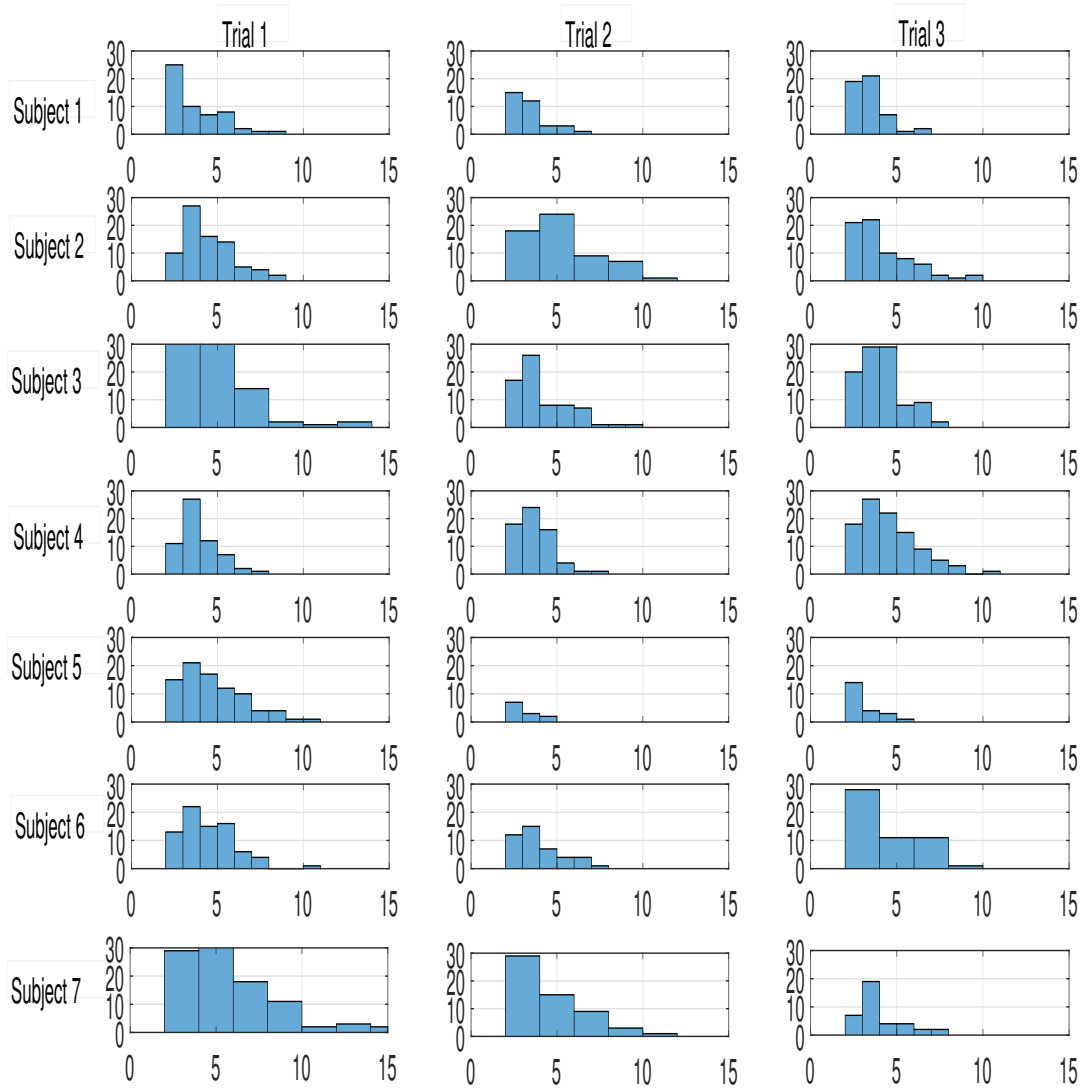


Figure 4.18.: Histogram of the accelerometer measurements which have the vector norm deviation higher than  $2.5m/s^2$  in comparison to gravity vector. The average capture time duration was approximately 10 seconds which equals to 500 samples in each trial.

	subj. 1	subj. 2	subj. 3	subj. 4	subj. 5	subj. 6	subj. 7
$l_{mA}$	17.88 ± 3.45	18.22 ± 5.35	13.28 ± 5.98	14.8 ± 2.84	19.84 ± 4.07	19.61 ± 2.32	16.49 ± 1.56
$l_{mB}$	25.29 ± 2.99	25.44 ± 5.87	22.45 ± 2.18	25.7 ± 1.13	26.28 ± 2.9	26.19 ± 2.71	31.31 ± 2.57
$l_{nB}$	15.86 ± 4.36	12.91 ± 3.93	11.12 ± 2.19	11.58 ± 2.29	13.66 ± 5.58	12.68 ± 1.11	10.94 ± 1.64
$l_{nC}$	9.65 ± 2.92	10.88 ± 1.83	12.05 ± 3.43	11.88 ± 4.3	12.82 ± 3.58	14.36 ± 4.79	9.30 ± 4.33

Table 4.5.: The error (mean ± SD) in position of each joint  $m, n$  with respect to each IMU  $A, B, C$  estimated by Seel *et al.* method using type A movements

	subj. 1	subj. 2	subj. 3	subj. 4	subj. 5	subj. 6	subj. 7
$l_{mA}$	12.5 ± 3.37	18.57 ± 4.3	15.6 ± 1.19	15.99 ± 2.14	15.02 ± 3.31	16.89 ± 0.7	13.68 ± 5.1
$l_{mB}$	24.39 ± 0.9	22.28 ± 4.93	19.72 ± 2.58	23.34 ± 2.81	25.92 ± 3.97	24.8 ± 3.16	31.18 ± 3.79
$l_{nB}$	9.98 ± 6.37	16.12 ± 0.52	10.26 ± 3.33	9.35 ± 2.01	12.49 ± 4.62	10.12 ± 1.85	7.23 ± 3.87
$l_{nC}$	14.86 ± 0.47	12.85 ± 1.57	9.5 ± 1.34	9.48 ± 1.15	11.54 ± 2.86	15.24 ± 5.94	11.86 ± 5.23

Table 4.6.: The error (mean ± SD) in position of each joint  $m, n$  with respect to each IMU  $A, B, C$  estimated by the proposed method using type A movements

	subj. 1	subj. 2	subj. 3	subj. 4	subj. 5	subj. 6	subj. 7
$l_{mA}$	15.27±1.86	23.36±3.32	17.92±7.58	16.79±4.29	21.47±4	18.73±3.92	16.72±2.1
$l_{mB}$	26.4±1.78	25.81±6.2	23.26±3.34	28.22±2.67	28.41±4.34	27.59±1.29	31.83±1.47
$l_{nB}$	17.17±2.38	13.19±3.13	11.49±2.24	10.48±2.42	11.83±5.45	12.01±1	9.58±0.4
$l_{nC}$	10.42±1.64	10.39±2.48	12.19±3.65	11.94±5.01	10.64±7.32	14.69±4.82	10.4±4.82

Table 4.7.: The error (mean±SD) in position of each joint  $m, n$  with respect to each IMU  $A, B, C$  estimated by Seel *et al.* method using type B movements

	subj. 1	subj. 2	subj. 3	subj. 4	subj. 5	subj. 6	subj. 7
$l_{mA}$	23.13±3.26	18.18±3.53	14.12±1.69	14±3.07	13.51±4.07	17.33±0.82	15.2±0.73
$l_{mB}$	14.26±0.87	17.03±4.98	19.69±3.04	18.42±2.88	16.49±7.61	20.21±2.23	24.79±4.37
$l_{nB}$	13.5±4.93	14.66±3.5	7.86±1.55	6.4±2.65	13.89±5.54	8.2±1.88	3.61±1.92
$l_{nC}$	13.72±0.22	11.71±3.23	9.93±0.93	10.17±2.51	8.88±5.49	13.34±3.14	11.94±3.86

Table 4.8.: The error (mean±SD) in position of each joint  $m, n$  with respect to each IMU  $A, B, C$  estimated by proposed method using type B movements

### 4.3.9.3. Repeatability

Repeatability was evaluated by considering three repetitions of calibration movements for each subject and the resulting SD as shown in Tables 4.5 to 4.8. The average SD over all subjects and for movements of types A and B are  $2.9\text{cm}$  and  $3.1\text{cm}$ , respectively, when using the proposed method. These values, when using the Seel *et al.* method, are  $3.27\text{cm}$  and  $3.38\text{cm}$  for type A and B movements, respectively. This shows slightly better repeatability of the proposed method.

### 4.3.9.4. Evaluation of observability conditions over experimental trials

Figure 4.19 represents the percentage of the measurements captured during each trial with random movements having the observability conditions 1, 2, or 3 or all together. The criteria are determined on the basis of the measured angular velocity and a threshold value of  $0.5\text{ radians}$ . The threshold is chosen relatively low so that the average number of limited movements of the segments around the hip can be considered useful measurements. Due to the noise inherited in the sensor data, it is difficult to determine exactly what percentage of the data could contribute to a better estimation of IMU positions under such conditions. Nevertheless, a rough evaluation is still possible. Here, this evaluation is carried out under the assumption of an upper threshold of 10% for the worst data condition and a lower threshold of 20% for the best data condition.

Taking into account the Figure 4.16 and the result of the Seel *et al.* method, it can be observed that the trials 1-5, 11, 14-16, which contain less than 10 percent of data with all the criteria, resulted in a relatively high error ( $> 17\text{cm}$ ), while trials 6 and 9 contained more than 20 percent of data where all criteria led to relatively small errors ( $< 16\text{cm}$ ). There are, however, two exceptions: trial 18 with a higher percentage of the proper data yielded the worst error, and trial 7 with not a high percentage of proper data yielded a better error similar to trials 6 and 9. Overall, this evaluation could be used to establish a primary method for verifying the data quality for body-IMU calibration, either during or after measurement acquisition. For this evaluation, the result of the Seel *et al.* method is used because according to the previous section, it is more sensitive to the input data. However, such a quality verification could also improve the optimization problem in the proposed method, when using the measurements of random movements.

## 4.4. Conclusion

This chapter presented the calibration process required for a suit to track the lower body movements.

The beginning is the IMU calibration, which includes two separate processes of inertial and magnetic sensors calibration. For the latter, a complete magnetometer calibration method was presented and evaluated. The method requires no any external equipment or precise information about the local magnetic field and provides an in-field and practical calibration procedure for end-users to be applied after installation. The proposed method obtains biases, scale factors, and non-orthogonality parameters in solving a geometric ellipsoid fitting problem, using only the fact that the magnitude of the true Earth magnetic field vector, measured in an orthogonal coordinate, is always constant. This leads to the optimal estimate of the calibration parameters.

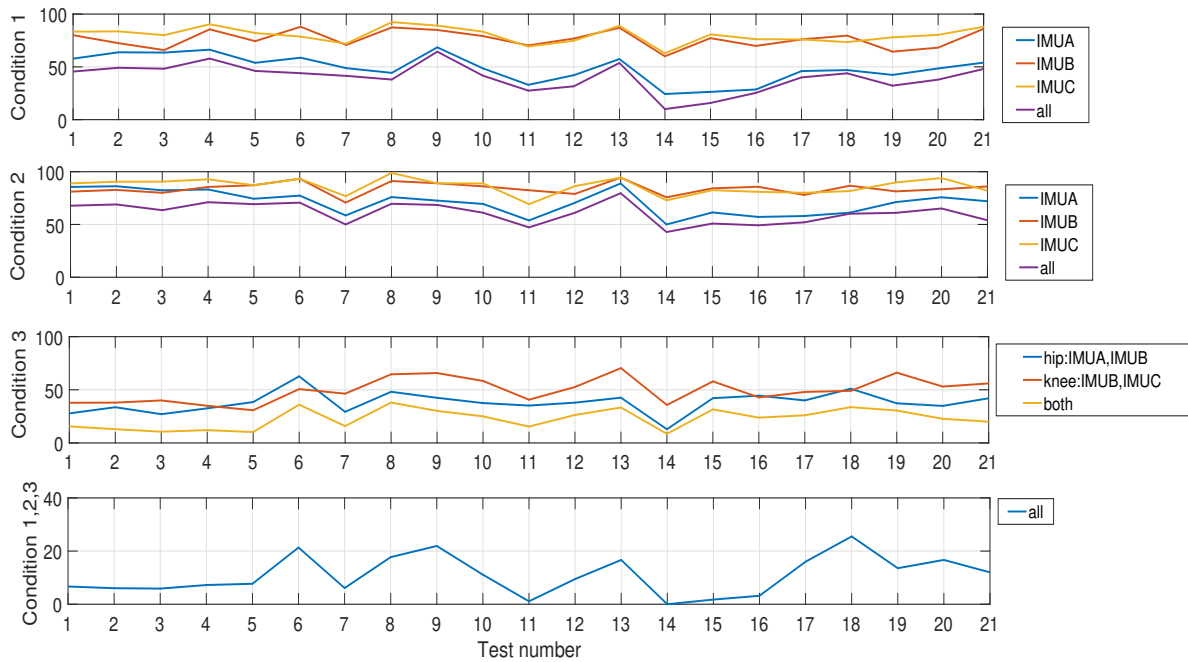


Figure 4.19.: The percentage of measurements with observability criteria. The criteria were detected based on the measured angular velocity and threshold of 0.5 radian.

During the design process, special attention was paid to choose an optimization tool, which is insensitive to a perturbed initial guess, which can be the result of applying suboptimal ellipsoid fitting on a set of noisy data.

For a complete magnetometer calibration procedure, so that this sensor can be used with the inertial sensors in an IMU, an alignment procedure has been proposed, which is based on the fact that in a homogeneous field, the inclination is always constant. Hence, there is no need for external heading information. The calibration parameters obtained were evaluated in different test scenarios demonstrating in most cases, higher precision in comparison with the calibration method included in the SDKs of the two available commercial IMUs. Additionally, the repeatability of the proposed method was investigated in terms of the variation in the estimated bias parameters, when performing multiple calibrations. The results indicate that in a homogeneous magnetic field, different ways of data capturing lead to the same bias calibration results. These evaluations also provide indications for online filtering and outlier rejection of the magnetometer measurements in a motion tracking scenario, which is the subject of the next chapter.

Furthermore, this chapter presents a novel and practical IMU to body position autocalibration method, specifically developed for the lower body. In this work, first, a theoretical analysis of an existing position calibration method is performed, showing its limited applicability for the hip and knee joints. Based on this, a method is proposed to simultaneously estimate the positions of three IMUs (mounted on the pelvis, upper leg, lower leg) relative to these joints. Finally, an experimental evaluation is performed based on simulated and real data. The presented method shows a significant improvement in terms of accuracy and robustness compared to a previous

method, especially when it comes to suboptimal (low variation) movements during calibration. This was also confirmed by extensive tests with real data and different types of movements.

It is also shown that for random movements, the global IMU orientations are erroneous due to the presence of outliers, especially from accelerometer measurements. Therefore, a simple method of orientation tracking is proposed, which can be realized using only gyroscope measurements, while the subject performs movements separately around each DOF. This shows an overall improvement, specifically for the leg segments, which cannot provide enough useful movements for calibration.

In addition, a primary method is proposed to verify the quality of the recorded measurements for body-IMU calibration. This is based on the observability conditions and the result of the Seel *et al.* method in the experiments with type B movements, as this method is more sensitive to such conditions. This approach can give a rough indication during data acquisition whether the variation of movements is sufficient for an acceptable resulted accuracy when only random movements are possible. The approach is to be examined more closely in the future with more test subjects.

## 5. Lower Body Motion Tracking

In order to provide biomechanical details of the lower body movements, an exercise monitoring application shall estimate hip and knee joint angles, as well as the position of the leg's segments. Here, these parameters are estimated with respect to an IMU mounted on a reference point on the body, i.e. pelvis. Therefore, tracking the orientation of an IMU mounted on the pelvis, here referred to as pelvis orientation, is critical during the exercise. This, as well, helps to identify the correct exercise (see Chapter 6).

This chapter explains two different approaches, which are used for real-time estimation of lower body motion during the strength exercise.

The first is orientation estimation, which is used to estimate both pelvis orientation and the global IMU orientations in the proposed Body-IMU calibration algorithm of Chapter 4. This approach is explained and evaluated in Section 5.1.

The second is the leg pose estimation, which provides knee and hip joint angles, and the position of the IMUs mounted on the leg's segments, here referred to as leg's segment position. These parameters are all estimated with respect to the coordinate frame of IMU mounted on the pelvis. In this approach, body-IMU calibration parameters, along with the kinematic constraints at joints, are incorporated in tracking the movements of the leg. Although this algorithm was proposed for leg movements, any other combination of two joints with similar characteristics, i.e. a socket-ball connected to a hinge joint, can be tracked using this method. The leg pose estimation approach and its evaluation for two strength exercises are described in Section 5.2.

### 5.1. Orientation estimation

The orientation of IMU is estimated as a quaternion (see Appendix C), which defines a rotation from a global frame  $G$  to the sensors' fixed frame  $S$ . As shown in Figure 5.1, the global frame is defined relative to the earth magnetic field and gravity reference vectors, which can be measured using magnetometer and accelerometer.

In this work, two approaches are implemented and compared. The first estimator is based on a common sensor fusion approach in the literature, where the zero angular acceleration is assumed [46, 74]. The second estimator contains an extended state vector, which provides the estimation of angular acceleration and magnetic field bias.

#### 5.1.1. Common Estimator

In this approach, the orientation and angular velocities,  $\vec{x} = [\vec{q}_{SG}, {}^S\vec{\omega}_{GS}]$  are estimated as states of an EKF. The following explains the process model and measurement models of the filter.

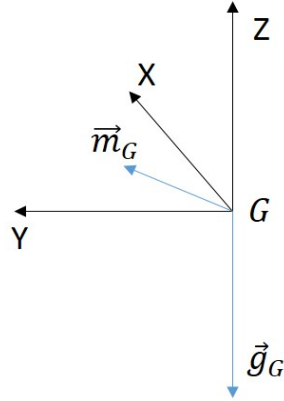


Figure 5.1.: The global coordinate system with respect to reference vectors i.e. gravity,  $\vec{g}_G$ , measured by accelerometer and earth magnetic field,  $\vec{m}_G$ , measured by magnetometer.

**Process model:** The time-continuous process model is the following:

$$\dot{\vec{q}}_{SG} = \Omega(-{}^S\vec{\omega}_{GS})\vec{q}_{SG} \quad (5.1a)$$

$${}^S\dot{\vec{\omega}}_{GS} = \vec{w}_\omega, \quad (5.1b)$$

where the angular velocity is modeled by a random-walk process with a zero-mean white Gaussian noise  $\vec{w}_\omega$ , with the covariance of  $Q_\omega$ . The discrete form of the above formulation is obtained by integration in the duration from  $t_{k-1}$  to  $t_k$  i.e.  $\Delta t$ . Equation (5.2) shows this formulation, which is used in the EKF prediction stage.

$$\vec{q}_k = (I_{4 \times 4} \cos(|\vec{u}_{k-1}|/2) + \Omega(\vec{\omega}_{k-1}) \frac{\sin(|\vec{u}_{k-1}|/2)}{|\vec{u}_{k-1}|/2}) \vec{q}_{k-1} \quad (5.2a)$$

$$\vec{\omega}_k = \vec{\omega}_{k-1}, \quad (5.2b)$$

where the suffices indicating coordinates are removed for brevity.  $u_{k-1}$  is the integration of angular velocity over  $\Delta t$ . This can be approximated by  $\omega_{k-1} \Delta t$  assuming the angular velocity is constant during this time.

**Accelerometer measurement model:**

$${}^S\tilde{\vec{a}} = -R_{SG}\vec{g}_G + \vec{v}_a \quad (5.3)$$

Note that in this model, the body acceleration is considered in the measurement noise.

**Gyroscope measurement model:**

$${}^S\tilde{\vec{\omega}} = {}^S\vec{\omega}_{GS} + \vec{v}_g \quad (5.4)$$

**Magnetometer measurement model:**



For magnetometer there are many different approaches are proposed in the literature to deal with the error due to magnetic disturbances. In this work the focus is on estimating such errors in the process model. Therefore instead of a comparative study of different measurement models only one model in 5.5 is used for both Estimator 1 and 2.

$${}^S\tilde{\vec{m}} = R_{SG} \vec{m}_{ref} + \vec{v}_m \quad (5.5)$$

In the above models  $\vec{v}_a, \vec{v}_g, \vec{v}_m$ , are the zero-mean Gaussian white noise vectors with the covariances of  $R_a, R_g, R_m$ , defined respectively for accelerometer, gyroscope, and magnetometer measurements.

#### 5.1.1.1. Outlier rejection

The outliers of accelerometer and magnetometer are detected using the thresholds on the norm of these vectors,  $acc_{th}, mag_{th}$ . In the case of outliers, the related measurement noise covariances are increased so that the correction of the measured outlier does not corrupt the estimation.

### 5.1.2. Extended Estimator

In the common estimator, the angular acceleration was assumed to be zero, which is not the case during intensive movements. Therefore, in the extended estimator, the angular acceleration is realized using a random walk model:

$$\vec{\alpha}_k = \dot{\vec{\omega}}_{k-1} \quad (5.6a)$$

$$\vec{\omega}_k = \vec{\alpha}_{k-1} \Delta t + \vec{\omega}_{k-1} \quad (5.6b)$$

The integration of quaternion with non zero angular acceleration is explained in Appendix C.

Additionally, the state vector is extended to include the magnetic field disturbances as an additive bias. This is modeled as a first-order GM process.

$$\dot{b}_m = -\mu b_m + w_m, \quad (5.7)$$

where  $\mu$  is the inverse of time constant of the process.

In every filter time update, this bias, i.e. magnetic disturbance, is predicted using the following equation:

$$b_{m_k} = b_{m_{k-1}} \exp(-\mu \Delta t) \quad (5.8)$$

Before each magnetometer measurement correction, the estimated bias is subtracted from the measurements.

### 5.1.3. Experimental results

With the setup, similar to what is described in Section 4.3.9.2 and shown in Figure 4.15, the orientation of IMU mounted on the pelvis is captured by both smart suit and optical system.

Parameter	Value
$R_a$	$10^{-3}I_{3 \times 3}$
$R_g$	$10^{-4}I_{3 \times 3}$
$R_g$	$10^{-3}I_{3 \times 3}$
$Q_{b_m}$	$10^{-4}I_{3 \times 3}$
$Q_\omega$	$5 \times 10^{-5}I_{3 \times 3}$
$\mu$	20
$acc_{th}$	$0.25 \times 9.8m/s^2$
$mag_{th}$	0.25

Table 5.1.: Values of the parameters which are used in the EKF's for orientation estimation

This experiment was carried out with 7 subjects each performing the squat exercise.

Both orientation estimators are implemented in Matlab. The initial orientations are estimated using the first accelerometer and magnetometer measurements and applying TRIAD algorithm [129]. In order not to be dependent on the local magnetic field information,  $m_{ref}$  in Equation 5.5 is estimated using a moving average filtering of the magnetometer measurements.

Here the covariance of the related outlier is multiplied by  $10^3$ . Table 5.1 presents the value of other parameters, which are required for both filters.

Figure 5.2 shows the estimated angular acceleration using the extended estimator and angular acceleration computed from the numerical differentiation of angular velocity. The result indicates that the estimated angular acceleration has less noise in comparison to the numerically computed version.

Figure 5.3 shows the comparison of the measured magnetic field versus the corrected magnetic field from the experiments with different subjects. Primarily, it illustrates the deviation of the vector norm from the mean for measured and corrected, which here is considered to be the reference magnetic field.

The orientations from IMU and optical system, are estimated as quaternions and for better understanding are converted to Euler angles. The error of both estimators is calculated with respect to optical results and illustrated in Figure 5.4. This figure shows that the extended estimator has an overall better result in comparison to the common version. The overall error for all the subjects with the new estimator is 7.4 degrees, while this error with the common estimator is 10.1 degrees.

The comparison of error from the extended estimator with an optical tracker is shown in Figure 5.5 for a representative experiment.

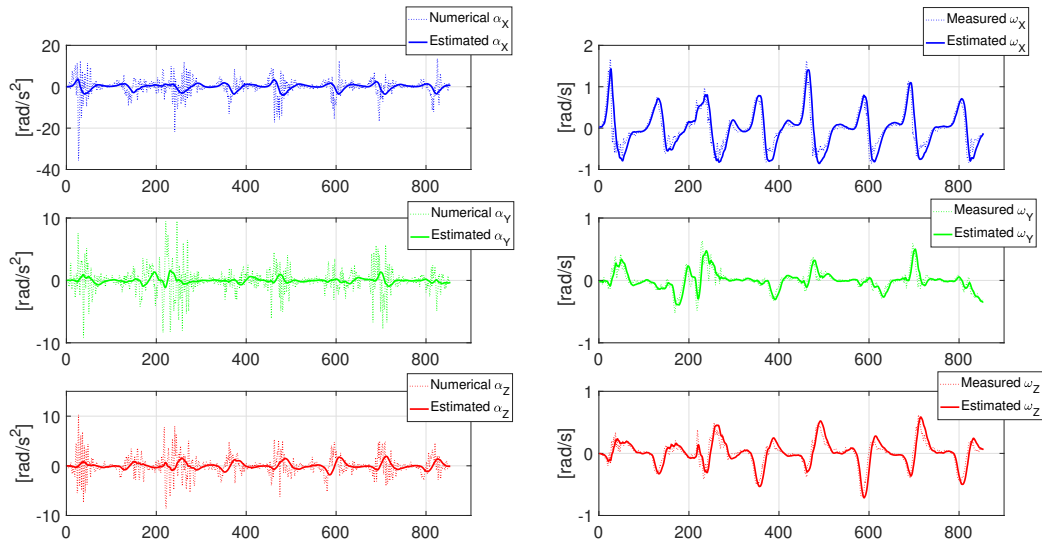


Figure 5.2.: The estimate versus numerically computed angular acceleration from a representative experiment where a subject performing the squat exercise.

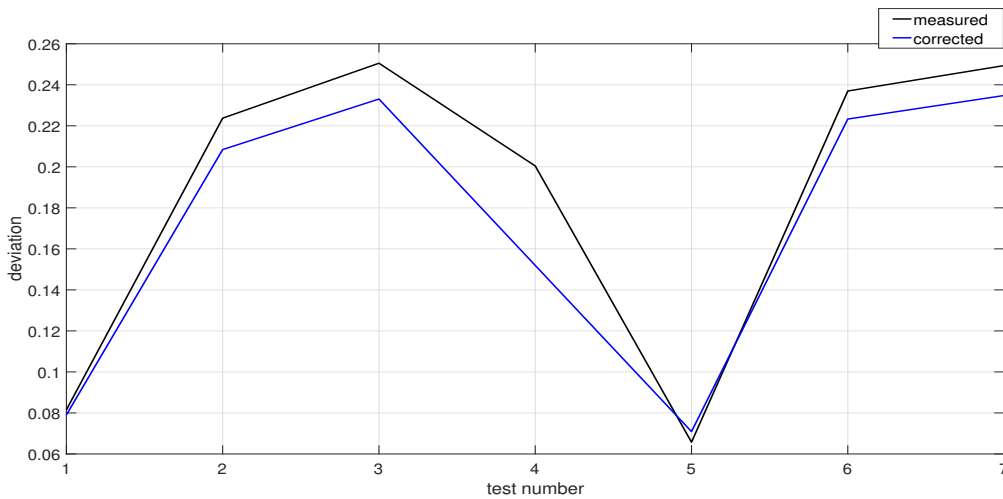


Figure 5.3.: The estimated versus measured magnetic field from result of the tests with 7 subjects performing the squat exercise. Note that the calibrated magnetometer measurements, according to the proposed method in Section 4.2 are supposed to be mapped to a unit sphere, therefore the deviation here has no unit.

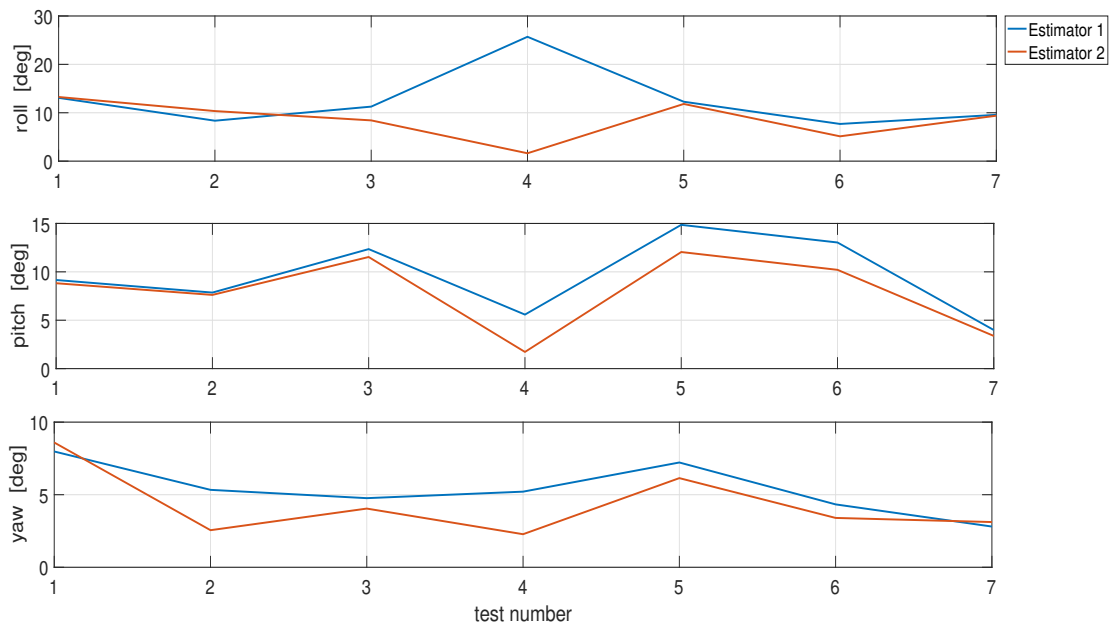


Figure 5.4.: The comparison of error from the common estimator with the extended estimator from result of the tests with 7 subjects performing the squat exercise.

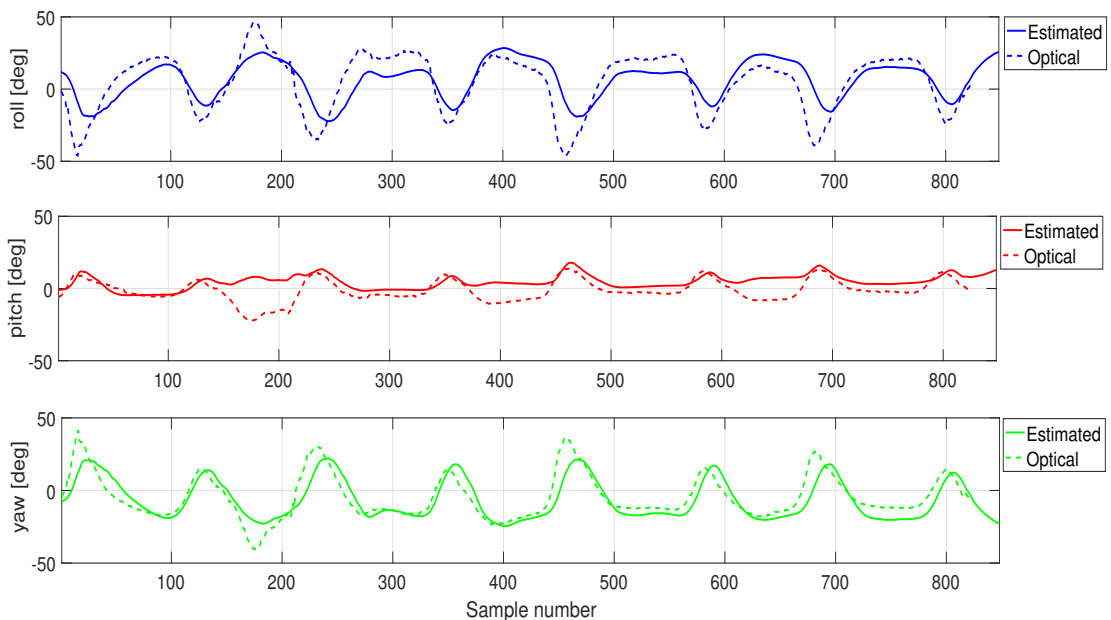


Figure 5.5.: The comparison of error of the extended estimator with optical tracker in a representative experiment where a subject performing the squat exercise.

## 5.2. Pose Estimation

In this work, an EKF is designed, which deduces leg pose from the IMU measurements, the estimated joint axes, and IMU positions. The two latter are obtained from the Body-IMU calibration method in Chapter 4.

For this estimation, the assumptions are (*c.f.* Figure 5.6):

- (1) a simple biomechanical model for leg, with rigid segments connected via frictionless joints: hip( $m$ ) with 3 DOF, knee( $n$ ) with one DOF
- (2) at least one IMU sitting on each rigid segment that should be tracked,  $A$  on the pelvis,  $B$  on the upper leg,  $C$  on the lower leg
- (3) forward kinematics equations
- (4) constant acceleration in the integration duration.

The state vector is presented in Equation (5.9), which includes the velocities,  $\vec{v}$ , and positions,  $\vec{p}$ , of the upper and lower segments in addition to the hip rotation quaternion and the knee joint angle, all of which are resolved in the pelvis IMU coordinate frame:

$$\vec{x} = [{}^A\vec{v}_B \quad {}^A\vec{v}_C \quad {}^A\vec{p}_B \quad {}^A\vec{p}_C \quad \vec{q}_{hip} \quad \vec{\theta}_{knee}] \quad (5.9)$$

### 5.2.1. Kinematic Process Model

The kinematic process model is defined in Equation (5.10) (tilde superscripts indicate the measurements, and the vector arrows are removed for simplicity).

$${}^A v_{B_k} = {}^A v_{B_{k-1}} + {}^A \tilde{a}_{B_{k-1}} \Delta t \quad (5.10a)$$

$${}^A v_{C_k} = {}^A v_{C_{k-1}} + {}^A \tilde{a}_{C_{k-1}} \Delta t \quad (5.10b)$$

$${}^A p_{B_k} = {}^A p_{B_{k-1}} + {}^A v_{B_{k-1}} \Delta t + \frac{{}^A \tilde{a}_{B_{k-1}} \Delta t^2}{2} \quad (5.10c)$$

$${}^A p_{C_k} = {}^A p_{C_{k-1}} + {}^A v_{C_{k-1}} \Delta t + \frac{{}^A \tilde{a}_{C_{k-1}} \Delta t^2}{2} \quad (5.10d)$$

$$q_{AB_k} = \exp(R_{AB_{k-1}} \tilde{\omega}_{B_{k-1}} - \tilde{\omega}_{A_{k-1}}) \otimes q_{AB_{k-1}} \quad (5.10e)$$

$$\theta_{BC_k} = \theta_{BC_{k-1}} + \Delta t (\tilde{\omega}_C \cdot {}^C r_n - \tilde{\omega}_B \cdot {}^B r_n) \quad (5.10f)$$

,where

$${}^A \tilde{a}_{B_{k-1}} = R_{AB_{k-1}} \tilde{a}_{B_{k-1}} - \tilde{a}_{A_{k-1}} \quad (5.11a)$$

$${}^A \tilde{a}_{C_{k-1}} = R_{AB_{k-1}} R_{BC_{k-1}} \tilde{a}_{C_{k-1}} - \tilde{a}_{A_{k-1}} \quad (5.11b)$$

where accelerometer and gyroscope measurements,  $\tilde{a}$  and  $\tilde{\omega}$ , are included as the control inputs. The knee joint angle is predicted based on the model, which is described in Section 4.3.5 in the previous Chapter.

In every prediction step of  $k$ ,  $R_{AB}$  is calculated from  $q_{AB}$ , which is the hip joint rotation, using the quaternion to rotation matrix conversion (Appendix C.3.1) and  $R_{BC}$  is calculated from  $\vec{\theta}_{BC}$

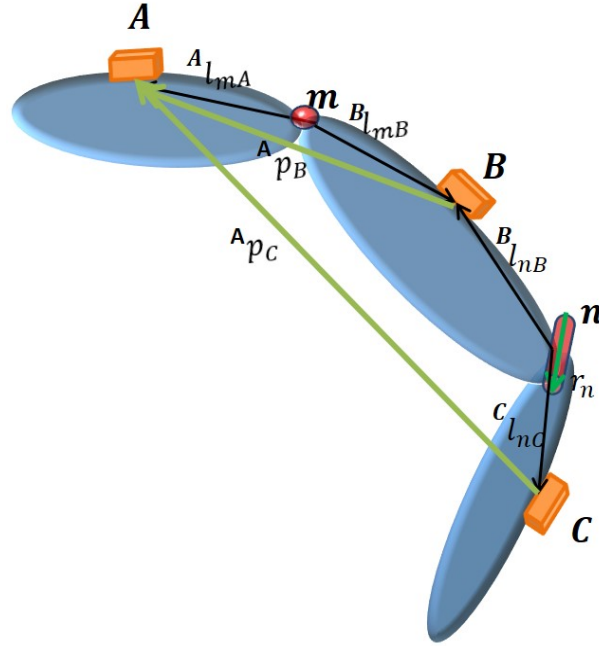


Figure 5.6.: Illustration of the leg segment positions,  ${}^A\vec{p}_B$ ,  ${}^A\vec{p}_C$ , as are defined by the position of IMUs mounted on the upper segment, IMU  $B$ , and lower segment, IMU  $C$  with respect to the coordinate frame of IMU  $A$  mounted on the pelvis. The spheroidal joint  $m$  refers to the hip, and the hinge joint  $n$  refers to the knee (one rotation axis:  $r_n$ ). The two joints are linked via the upper leg segment. The quantities  $l_{mA}, l_{mB}, l_{nB}, l_{nC}$  are the IMU position vectors with respect to joints which are estimated based on the proposed method in Section 4.3.4

and  ${}^B r_n$  using the axis angle to rotation matrix conversion (Appendix C.2).  $\Delta t$  is the sampling time, in other words, the duration between two prediction steps of  $k$  and  $k - 1$ .

### 5.2.2. Observation Model

The observation model is defined based on assumption 1: the segments pelvis and upper leg connected in hip joint, Equation (5.12b), and upper and lower legs connected in the knee joint, Equation (5.12a):

$${}^A\vec{p}_{B_k} = -R_{AB} {}^B\vec{l}_{mB} + {}^A\vec{l}_{mA} \quad (5.12a)$$

$${}^A\vec{p}_{C_k} = -R_{AB}(R_{BC} {}^C\vec{l}_{nC} - {}^B\vec{l}_{nB} + {}^B\vec{l}_{mB}) + {}^A\vec{l}_{mA} \quad (5.12b)$$

### 5.2.3. Experimental Results

The experiment setup is similar to what is described in Section 4.3.9.2. The pose estimation algorithm is implemented in Matlab and evaluated for the leg movements in strength exercises.

Parameter	Value
$R_a$	$10^{-4}I_{3 \times 3}$
$R_g$	$10^{-4}I_{3 \times 3}$
$R_l$	$10^{-8}I_{3 \times 3}$
$Q_v$	$10^2I_{3 \times 3}$

Table 5.2.: Values of the parameters which are used in the EKF for pose estimation

The state vector is initialized, using the Equations (5.12a) and (5.12a) and the initial global orientations, using the orientation estimator explained in Section 5.1.2. The IMU positions and joint axes are obtained from algorithms explained in Chapter 4. Table 5.2 shows the values of noise covariances, which are used in the filter.

### 5.2.3.1. Joint Angles

The precision of the estimated joint angle evaluated using the optical tracking system [95] as the ground truth. In order to estimate the joint angle in the optical system from the marker positions accurately, an experimental setup was created for a subject, by mounting two markers on each leg segment, as shown in Figure 5.7. The subject performed a simple knee flexion/extension and hip abduction. In optical tracking one vector, which is the subtraction of two single marker positions is assumed on each leg segment. The knee joint angle is obtained from the angle between vectors related to upper and lower legs. The right hip joint angle is obtained from the angle between the left and right upper legs. The result of knee flexion/extension is evaluated in the sagittal plane and shown in Figure 5.8.

The error for the right and left knee are  $6.65 \pm 6.26$  and  $4.46 \pm 3.93$  (*mean*  $\pm$  *SD*) degrees, respectively.

The result of hip abduction is evaluated in the frontal plane and shown in Figure 5.9. The error in this test is  $4.90 \pm 3.66$ (*mean*  $\pm$  *SD*) degrees.

under comparable conditions, however, leave room for improvement. The higher error observed for the right joint could result from magnetic disturbances generated by the controller, battery or smartphone, or could be the result of soft tissue artifacts. This will be further investigated as part of our future work.

### 5.2.3.2. Segment Position

With the setup shown in Figure 4.15, the positions of IMUs mounted on the leg segments are captured by both smart suit and optical system. This experiment was carried out with 7 subjects each performing squat and hip abduction/adduction exercises.

The results for squat exercise are presented in Table 5.3. The average error for all subjects in the estimation of  $P_C$  is  $9.68cm$ , which is higher than  $P_B$ , with an error of  $7.66cm$ . The reason for this is that the error of  $P_C$  contains errors related to the knee joint angle plus the error of IMU position in particular  $l_{nC}$ . Figure 5.11 shows the estimated positions of leg segments in squat exercise for one representative subject using the proposed approach and optical tracker.

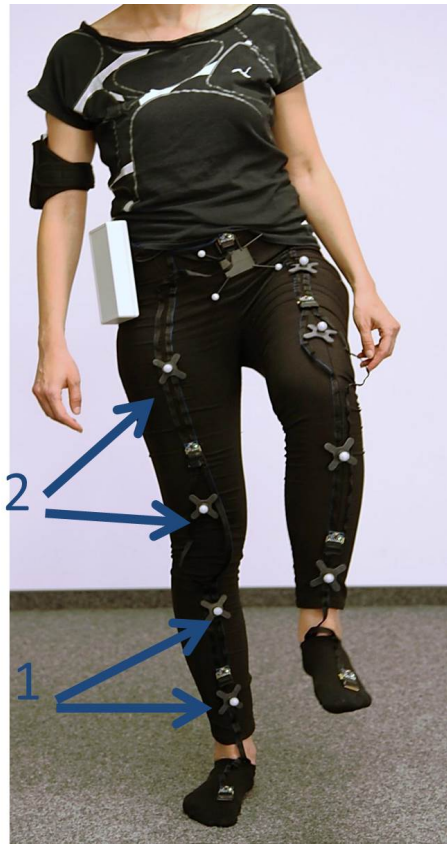


Figure 5.7.: Setup for joint angle estimation evaluation. In order to simplify two single markers, shown with arrows, are placed on each segment.



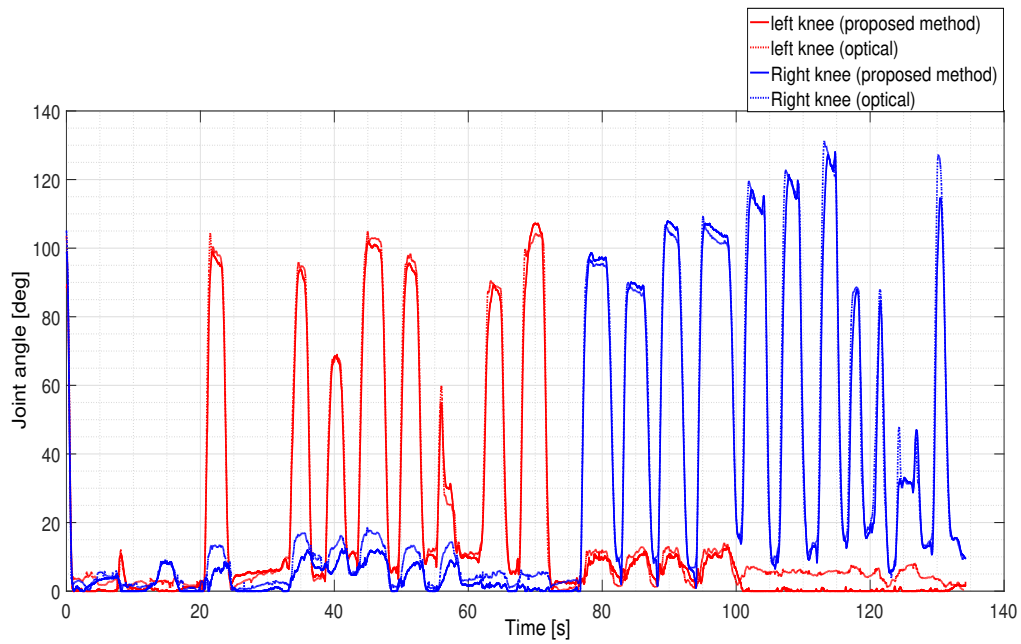


Figure 5.8.: Comparison of the knee joint angle as estimated using the proposed pose estimation method with the optical tracker result.

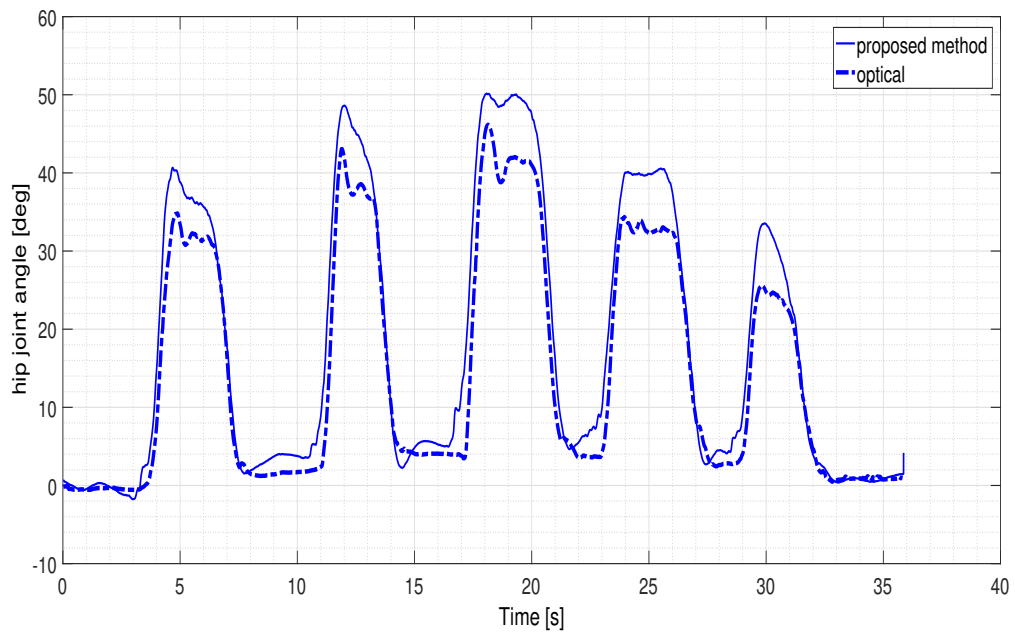


Figure 5.9.: Comparison of the hip joint angle as estimated using the proposed pose estimation method with the optical tracker result.

Squat						
cm	$P_B$			$P_C$		
	[RMS,	STD,	Max]	[RMS,	STD,	Max]
subj. 1	[8.47,	10.02,	4.10]	[8.98,	8.43,	36.16]
subj. 2	[7.72,	5.13,	16.53]	[7.69,	3.87,	14.20]
subj. 3	[6.05,	4.44,	15.30]	[9.12,	5.49,	17.68]
subj. 4	[6.57,	4.93,	19.92]	[7.51,	6.14,	24.64]
subj. 5	[8.91,	5.10,	18.02]	[7.84,	4.14,	16.96]
subj. 6	[7.20,	4.03,	13.73]	[5.47,	3.55,	12.84]
subj. 7	[6.40,	4.65,	15.27]	[7.42,	5.15,	18.53]

Table 5.3.: Error of estimated upper and lower segments positions using the proposed method for squat exercise.

Abd/Adduction						
cm	$P_B$			$P_C$		
	[RMS,	STD,	Max]	[RMS,	STD,	Max, RMS]
subj. 1	[5.19,	3.38,	10.57]	[ 10.53,	6.91,	21.40]
subj. 2	[4.83,	2.97,	25.61]	[ 9.96,	6.14,	24.84]
subj. 3	[4.60,	1.99,	8.52]	[ 10.63,	5.66,	21.18]
subj. 4	[7.16,	3.87,	13.84]	[ 12.31,	7.14,	24.65]
subj. 5	[6.10,	3.64,	12.40]	[12.43,	8.58,	27.58]
subj. 6	[7.74,	4.58,	15.56]	[16.28,	11.0,	34.62]
subj. 7	[8.09,	5.95,	19.45]	[ 16.33,	12.84,	42.45]

Table 5.4.: Error of estimated upper and lower segments positions using the proposed method for abduction and adduction exercise

The results for abduction/adduction exercise are presented in Table 5.4. The average error for all subjects in the estimation of  $P_C$  is  $12.63cm$  which is more than twice of  $P_B$  with the error of  $6.24cm$ . An accumulated error from the knee joint angle and the IMU position causes this higher error, as was described for the squat exercise.

The errors in segment position estimation for squat exercise are also compared, when using different body-IMU calibration approaches, in Figure 5.10. As was expected from the evaluation of Chapter 4, the proposed calibration method has led to a better result for the estimation of segment positions.

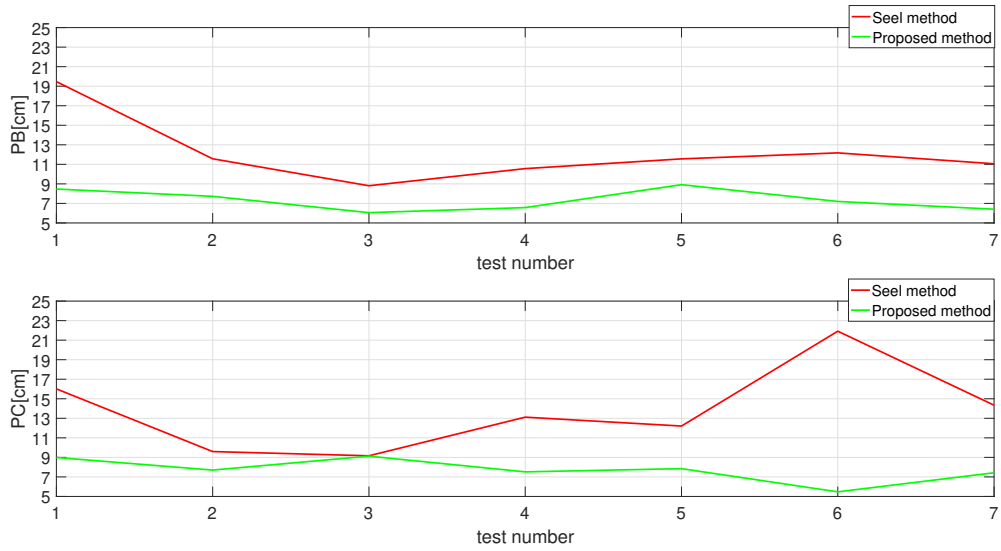


Figure 5.10.: Comparison of segment position error when using body-IMU calibration methods in [124] (red) and the proposed method in Section 4.3.4 (green)

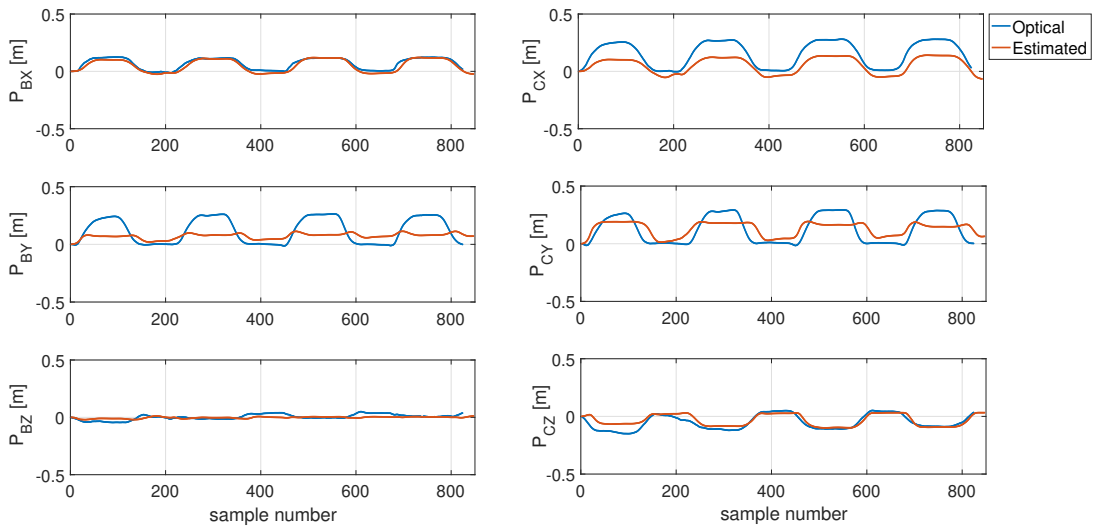


Figure 5.11.: The estimated positions of IMUs mounted on upper and lower leg,  $P_B$ ,  $P_C$ , using IMU measurements and proposed method versus optical tracker from a representative experiment

### 5.3. Conclusion

This chapter explains two approaches for real-time estimation of orientation and lower body motion. These approaches provide the orientation of pelvis, which is considered as the body coordinate reference point, hip and knee joint angles, and leg segment positions, all with respect to pelvis. Using such information, the critical measures for monitoring the strength exercises, such as ROM and the posture imbalances, can be determined. Moreover, they can be applied in the exercise identification process. Additionally, joint angles and segment positions provide good visual feedback of the user's performance (Figure 3.7).

The proposed orientation estimator is based on an EKF with a state vector, including angular acceleration and magnetic disturbance offset. The result of this algorithm was evaluated and shown that in comparison with a common orientation estimator, it achieves better results when applying to the measurements of IMU mounted on the pelvis while performing the squat. In future work, the estimated magnetic disturbances can be further evaluated with a known source magnetic field. Moreover, the current approach can be extended using an adaptive tuning for the measurement noise in order to optimize the filtering in the presence of outliers.

The pose estimation approach is also based on an EKF, where only inertial measurements are contributing as control inputs in the estimation. This reduces the computational complexity as there is no observation model related to those measurements. Instead, the constraints, which are defined based on the assumption of connected segments at joints, by incorporating the body-IMU calibration parameters, comprise more simplified observation models. The evaluation of this approach shows relatively good results considering the dynamic of the performances.

Figure 5.12 presents the computational graph of the process in the current chapter, body motion tracking, in connection with the calibration process in the previous chapter, and exercise identification in the next chapter.

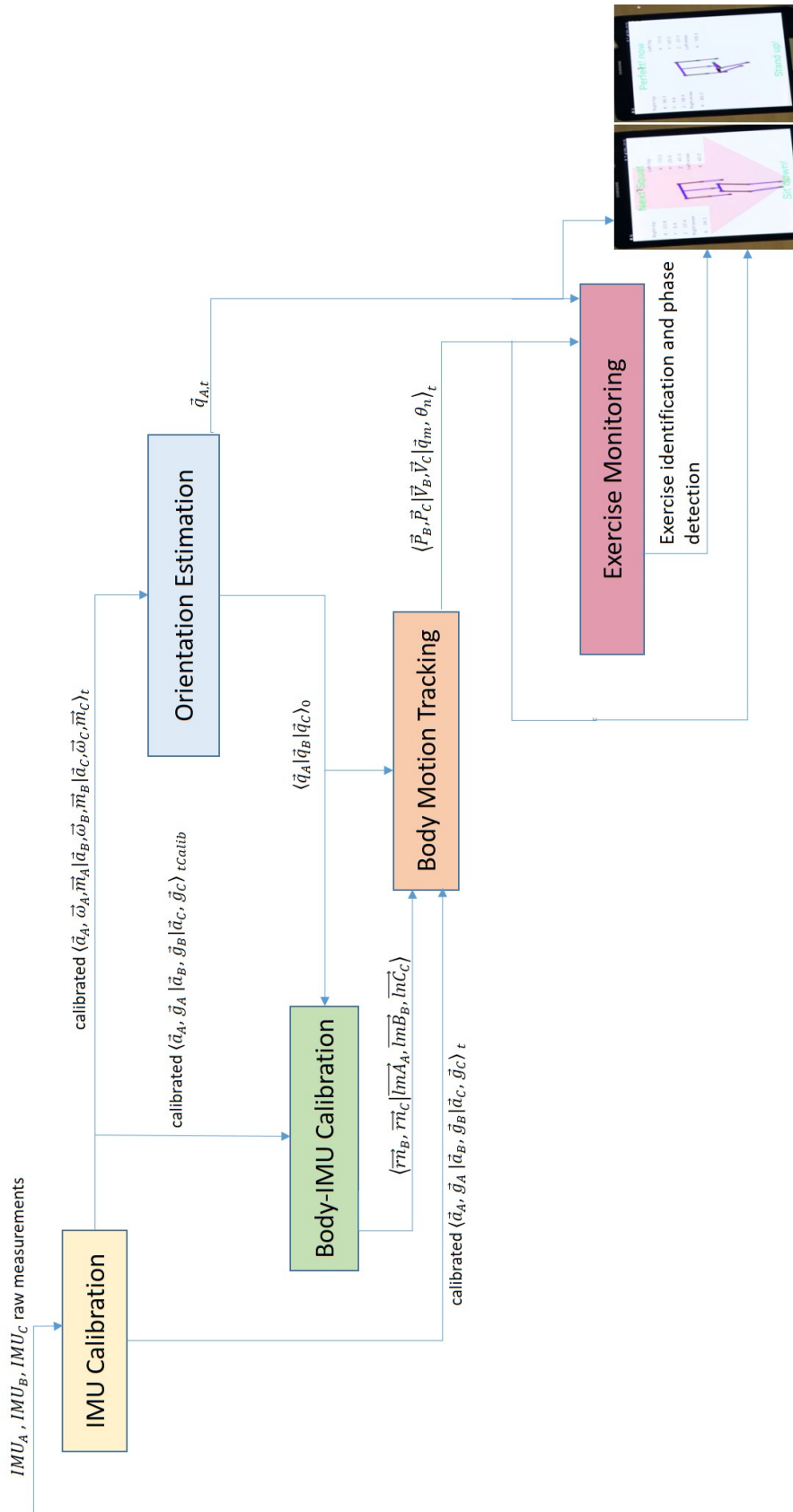


Figure 5.12.: the overall computational graph of the system



## 6. Exercise Identification

This chapter presents the process of exercise identification. The focus is on online template matching approaches based on Dynamic Time Warping (DTW). DTW is described in Section 6.1 in the offline form. Section 6.2 addresses challenges of online DTW-based approaches and describes four various methods in the related work for optimizing their performance. Section 6.3 presents the proposed method. Section 6.4 evaluates and compares the result of the formerly discussed methods, in the application of squat exercise identification using two different types of motion signals and in terms of accuracy and execution time.

### 6.1. Offline DTW

The DTW transformation calculates minimum distances between the two signal sequences, regardless of the difference in acceleration and deceleration. This means, this algorithm uses an elastic transformation of the time series to recognize similar shapes with different phases. If  $X = (x_1, \dots, x_n)$  is the source sequence and  $Y = (y_1, \dots, y_m)$  is the query sequence and  $X, Y \in \Phi$ , where  $\Phi$  is the feature space, the DTW transformation is  $d : \Phi \times \Phi \rightarrow \mathbb{R} \geq 0$ . The algorithm first builds up a local cost matrix  $C_l$ , which contains all the pairwise distances between the features in  $X$  and  $Y$  as follows:

$$C_l \in \mathbb{R}^{n \times m}, c_{i,j} = \|c_i - c_j\|, i \in 1, \dots, n, j \in 1, \dots, m, \quad (6.1)$$

where  $\| \cdot \|$  is the vector norm. The areas of the matrix with the minimum values define the warping path.

This method has a time complexity of  $O(n^2)$ . Therefore, it is efficient for a finite number of features in  $X$ . With increasing length of  $X$ , for example, in the case of a real time exercise identification process with a stream of features, the number of possible warping paths grows exponentially. Therefore, a dynamic programming approach is introduced to reduce complexity as follows:

$$dtw(i, j) = c_{i,j} + \min \begin{cases} dtw(i, j-1) \\ dtw(i-1, j) \\ dtw(i-1, j-1) \end{cases} \quad (6.2)$$

$$dtw(0, 0) = 0, dtw(i, 0) = dtw(0, j) = \infty$$

$$(i = 1, \dots, n; j = 1, \dots, m),$$

where  $c_{i,j}$  is defined in (6.1). This reduces the temporal and spatial complexity to  $O(mn)$ , which is still not applicable for online template matching of streaming data.

## 6.2. Online DTW

There are many different proposed methods for accelerating the DTW, such as lower bounding in [58], where the range of the search for the warping path is limited, or the early abandoning in [59] that consists of starting an incremental computation of DTW and stopping if it exceeds a lower bound. However, these methods can not solve the problem of template matching for on-line streaming. Rkthanmanon et al. in [102] propose UCR-DTW, combining eight techniques to accelerate DTW. The experimental results show that this method has a low computational time and high accuracy. However, it is assumed that the subsequence and query have the same length. Moreover, the combination of several techniques results in a complex structure. In [116] Sakurai et al. have introduced an efficient DTW-based method with a simple structure for monitoring the streaming subsequences, which reduces the temporal and spatial complexity to  $O(n)$ . This approach is discussed in detail in the next Section.

Other than accelerating and improving the storage requirement, there are some proposed methods to increase the accuracy while maintaining the time complexity, mostly based on the normalization idea; As described in [102] in the problem of identification of video images, the scale can change due to many factors, such as camera zooming, camera tilt angle, or for example, different clothing of the subject. Therefore, they should be normalized for a meaningful calculation of distances between the template and the video sequences. In the normalization process, the query and streaming subsequence are transformed into comparable ranges. Therefore, the different amplitude levels can not be mistaken with different structures. [43], [102] propose z-score normalization during online streaming based on SPRING using a fixed-length sliding window. As different sizes of the window can cause unwanted fluctuations, which affect the robustness of DTW against disturbances in the time axis, [152] proposes a dynamic z-score normalization. To solve the problem of z-score normalization, where z-score coefficient changes frequently in a data stream, [42] proposes an online min-max normalization for improving SPRING. However, none of these works directly considers higher data dimensions, which can highly degrade the optimization of accuracy and speed for online DTW-based approaches. In the current work, the proposed solutions in [43], [42], and [152] are discussed and evaluated for exercise identification with one-dimensional data from the knee joint angle. In addition, [43] and [152] are extended to consider higher data dimensions, as it is critical for such application.

Approximation based approaches, such as Piecewise Aggregated Approximation(PAA) [56], attempt to reduce the processing time by transforming the original sequence into a symbolic representation. In PAA, the equal-lengthed intervals of a sequence are approximated by their mean values. Based on PAA, iSax technique, one of the most powerful indexing techniques, was developed in [125] using Euclidean distances. It is shown that iSax is very accurate and fast. However, using Euclidean distance as the similarity measure makes it vulnerable in dealing with the time fluctuations. In this work, the concept of PAA is adopted and extended to other features besides mean value, in order to increase the efficiency of the online DTW-based approach in SPRING [116].



### 6.2.1. SPRING

SPRING introduces a new definition of the distance matrix, known as subsequence time warping matrix (STWM), where each cell contains  $d(t, i)$ , which is the best distance to match  $X[t]$  to  $Y[i]$ , along with the start position  $s(t, i)$ . In other words, the  $d(t, i)$  is the distance of a subsequence starting from  $s(t, i)$  to  $t$ . This leads to a reduction in the processing time and space required to store DTW matrix. In fact, only two arrays of length of the query,  $m$ , related to the distances and start points, should be stored and updated at every each sample arrival.

The distance in SPRING is calculated as follows:

$$\begin{aligned}
 d(t, i) &= \|x_t - y_i\| + d_{best}, \\
 d_{best} &= \min \begin{cases} d(t, i-1) \\ d(t-1, i) \\ d(t-1, i-1) \end{cases} \\
 d(t, 0) &= 0, d(0, i) = \infty \\
 (t &= 1, \dots, n; i = 1, \dots, m).
 \end{aligned} \tag{6.3}$$

Therefore, the starting points should be updated according to the new distance in Equation (6.4):

$$s(t, i) = \begin{cases} s(t, i-1) & (d(t, i-1) = d_{best}) \\ s(t-1, i) & (d(t, i-1) = d_{best}) \\ s(t-1, i-1) & (d(t-1, i-1) = d_{best}) \end{cases} \tag{6.4}$$

There are two different types of subsequent matching: best query and range query. While range query finds a local minimum, the best query, among all the possible subsequences, finds a subsequence with the shortest distance from a query  $Y$  starting at each sample received,  $X[t_s]$ .

For online streaming data with semi-infinite length, the range query is preferable to the best query. To avoid the heavily overlapping matched subsequences, SPRING proposes a modified range query called disjoint query with an additional condition such that among all the subsequences close enough to the query sequence,  $dtw(X[t_s : t_e], Y) < \epsilon_0$ , the algorithm reports only the local minimum; which means the distance is the smallest.

Therefore, after the operation in Equation 6.4 start and end time of a best-so-far found subsequence and its DTW distance to the query are updated respectively:  $t_s = s(t, m)$ ,  $t_e = t$ , and  $d_{min} = d(t, m)$ , when condition  $d(t, m) < d_{min} \wedge d(t, m) \leq \epsilon$  is true.

According to disjoint query, the matched subsequence at time  $t-1$  is reported at time  $t$  if none of the updated entries of  $d(t, k)$  with  $k = 1, \dots, m$  follows the previous condition, unless its start time is after previously detected end time, in that case, it possibly belongs to the next matching subsequence. The condition for reporting the matched subsequence can be summarized as:

$$d_{min} \leq \epsilon \wedge (\forall d(t, k) > d_{min} \vee s(t, m) > t_e) \tag{6.5}$$

Before the next search starts,  $d_{min}$  and all the entries of the list  $d$  whose starting time are before  $t_e$  are set to infinity, so that a currently matched subsequence is not considered in the next search. At the end of each time point, the old lists are substituted by the new lists. At each

time tick only two lists of size  $m$  have to be updated and only four lists need to be stored. SPRING has a simple structure and can be implemented with few lines of code. Moreover, query and subsequence from stream don't need to have a similar length, as is required for UCR-DTW [102]. In addition, this approach can be easily extended to multidimensional queries and subsequences. However, this increases the execution time, as shown in the experimental results in Section 6.4.

### 6.2.2. Normalization-supported SPRING(NSPRING)

To improve the accuracy of SPRING a normalization supported SPRING(NSPRING) is proposed in [43]. This approach is based on z-score normalization where  $x_t$  is normalized to  $x'_t$  according to Equation 6.6:

$$x'_t = \frac{x_t - \mu}{\sigma} \quad (6.6)$$

, where  $\mu = \frac{1}{m} \sum_{i=1}^m x_i$  is the mean value and  $\sigma^2 = \frac{1}{m} \sum_{i=1}^m x_i^2 - \mu^2$  is the variance of a sequence. To apply the normalization in the time series, the length of a subsequence must be known. This is not possible in SPRING, as the length of the subsequence is known when it is identified. In NSPRING, this length is assumed to be equal to the length of query.

In this method given a sequence of  $X = \{x_1, \dots, x_n\}$  and a query of  $Y = \{y_1, \dots, y_m\}$ , first, to calculate the intermediate z-normalization, a buffer stores the first  $m$  values arrived from  $X$ . Afterwards, two temporary variable,  $sum_1$  and  $sum_2$  are calculated:

$$sum_1 = x_{t'} + x_{t'+1} + \dots + x_t \quad (6.7a)$$

$$sum_2 = x_{t'}^2 + x_{t'+1}^2 + \dots + x_t^2 \quad (6.7b)$$

, where  $t' = t - m + 1$ , with  $x_{t'}$  and  $x_t$  as the first and the last value of the buffer. Each entry of STWM in NSPRING stores four values,  $d(t', k)$ ,  $s(t', k)$ ,  $M(t', k)$ , and  $SD(t', k)$  which are obtained in following:

$$d(t', i) = \left\| \frac{x_{t'} - M(t', i)}{SD(t', i)} - y_i \right\| + d_{best},$$

$$d_{best} = \min \begin{cases} d(t', i-1) \\ d(t'-1, i) \\ d(t'-1, i-1) \end{cases} \quad (6.8)$$

$$d(t', 0) = 0, d(0, i) = \infty$$

$$(t' = 1, \dots, n; i = 1, \dots, m).$$

$$s(t', i) = \begin{cases} s(t', i-1) & (d(t', i-1) = d_{best}) \\ s(t'-1, i) & (d(t', i-1) = d_{best}) \\ s(t'-1, i-1) & (d(t'-1, i-1) = d_{best}) \end{cases} \quad (6.9)$$

$$m(t', i) = \begin{cases} M(t', i-1) & (d(t', i-1) = d_{best}) \\ M(t'-1, i) & (d(t', i-1) = d_{best}) \\ M(t'-1, i-1) & (d(t'-1, i-1) = d_{best}) \end{cases} \quad (6.10)$$

$$SD(t', i) = \begin{cases} SD(t', i-1) & (d(t', i-1) = d_{best}) \\ SD(t'-1, i) & (d(t', i-1) = d_{best}) \\ SD(t'-1, i-1) & (d(t'-1, i-1) = d_{best}) \end{cases} \quad (6.11)$$

, where  $s(t', 0) = t'$ ,  $M(t', 0) = sum_1/m$  and  $SD(t', 0) = \sqrt{sum_2/m - m(t', i)^2}$ . It can be noticed that  $d(t', i)$  and  $s(t', i)$  are obtained similar to SPRING, Equations 6.4, 6.3, with a difference that  $x_{t'}$  is normalized before DTW distance calculation using the intermediate mean value and standard deviation stored in two lists of  $m$  and  $sd$ . Besides, at a current time point,  $t$ , these lists are updated for the arrived value in time point  $t'$ . This results in a delay of  $m = t' - t$  time points in reporting the matched subsequence, in comparison to SPRING which has only a negligible delay due to disjoint query. To maintain low temporal and spatial complexity, after the buffer is full, before inserting a new value, the old entry can be deleted from the buffer while updating  $sum_1$  and  $sum_2$ :

$$sum_1 = sum_1 - x_{t'} + x_t \quad (6.12a)$$

$$sum_2 = sum_2 - x_{t'}^2 + x_t^2. \quad (6.12b)$$

The conditions to find the minimum path and reporting the matched subsequence is similar to SPRING, as described in Section 6.2.1. This approach has similar time and space complexity as SPRING for one-dimensional data. However, it has an inherent delay. Moreover, for higher dimensions, more lists are required to be updated and stored at each time point which makes it inefficient for such applications.

### 6.2.3. Improved SPRING(ISPRING)

Since the incrementally computed z-score coefficients change by every new entry, the computational cost in NSPRING is high. Moreover, new z-score coefficients are not applied to the preceding time entries, which can lead to inaccuracy. Therefore, [42] proposes an improved SPRING(ISPRING) based on a min-max normalization, where  $x$  is normalized as follows:

$$x'_t = \frac{x_t - x_{min}}{x_{max} - x_{min}}. \quad (6.13)$$

In this method, when a new sample arrives, a monitoring window of size  $l$  checks if a new minimum or maximum value among all the window entries can be found. With a new min-max coefficient for normalization, all the time warping distances need to be calculated from the entries of the monitoring window i.e. entries from time  $t - l + 1$  to the current time  $t$ . Otherwise the algorithm only updates the entries of current list  $d(t, k)$  based on  $x'_t$ , which is normalized using the previous min-max coefficient. When a minimum distance as a candidate for a best-so-far subsequence is detected, the entries of the candidate subsequence from  $t_s$  to  $t_e$  is searched for the current min-max coefficient used for normalization. If it is not found, the distance needs to be corrected by expanding the subsequence backward and adding up the distances between the first entry of query and all the previous entries until the subsequence contains the min-max coefficient. This search can be left earlier as the distance exceeds the minimum criteria. Otherwise, the matched subsequence is reported.

In contrast to UCR [102], ISPRING finds the patterns whose lengths are different with those of query, and claimed to have better results. However in practice similar to z-score coefficient, the min-max coefficient is changing frequently, which results in higher computational cost. Moreover, this method does not adopt the disjoint query in SPRING, which results in reporting many overlapping subsequences, as presented in the experimental results. The extension of ISPRING to support multidimensional data is rather complicated, as the search for minimum and maximum values of each DOF directly influences the distance calculation.

#### 6.2.4. Dynamic Normalization based Real-time Pattern Matching (DNRTPM)

Normalization on the fixed-length sliding window causes unwanted structural distortions, which contradicts the natural robustness of DTW with respect to fluctuations in the time axis. To solve this problem, a dynamic z-score normalization approach is proposed in a recent work, [135]. This approach is based on the STWM concept in [116], where the z-score coefficient is calculated incrementally at each time point based on the current entry and the previous z-score coefficient. This results the standard deviation and mean value for the first entries of a candidate subsequence to be different than those of its last entries. To compensate for this, an amplification and a shifting factor are introduced:

$$\eta_k = \frac{\sigma_{t_s, t_e}}{\sigma_{t_s, k}}, \quad \delta_k = \frac{\mu_{t_s, k} - \mu_{t_s, t_e}}{\sigma_{t_s, t_e}}, \quad k = t_s, \dots, t_e \quad (6.14)$$

, where  $\sigma_{t_s, k}$  and  $\mu_{t_s, k}$  are standard deviation and mean value calculated incrementally, at time  $k$ , based on the entries from time  $t_s$  to  $k$ . According to the invariance properties, it is proved that these values are similar to the ones of the query for a candidate subsequence under one condition:

$$\frac{k' - t_s}{t_e - t_s} = \frac{k}{m - 1} \rightarrow \eta_k = \eta'_{k'}, \delta_k = \delta'_{k'} \quad (6.15)$$

, where  $\eta'_{k'}$  and  $\delta'_{k'}$  are the amplification and shifting factors of the subsequence, while  $\eta_k$  and  $\delta_k$  are those of the query. The mapping between  $k$  and  $k'$  is achieved through DTW itself as follows:

$$d(t, k) = \min \begin{cases} d'(t, k - 1) \\ d'(t - 1, k) \\ d'(t - 1, i - 1) \end{cases} \quad (6.16)$$

$$d'(i, j) = \left\| \frac{x'_{s(i, j), t} - y'_{0, k}}{\eta_k} \right\| + d(i, j)$$

$$i = t - 1, t; j = k - 1, k.$$

$$d(t, -1) = 0, d(-1, k) = \infty$$

$$(t = 0, \dots, n; i = 0, \dots, m)$$

, where  $x'_{s(i, j), t}$  is the z-score normalization of  $x_t$  on the subsequence of  $X[s(i, j) : t]$  and  $y'_{0, k}$  is  $k$ th normalized value of the query. Therefore, in each time point this method requires to

loop over all the values in the query three times for calculation of  $d'(i, j)$ , before updating the minimum distance. The list of start point is updated according to the position of minimum distance:

$$s(t, k) = \begin{cases} s(t-1, k) & (d(t, k) = d'(t-1, k)) \\ s(t, k-1) & (d(t, k) = d'(t, k-1)) \\ s(t-1, k-1) & (d(t, k) = d'(t-1, k-1)) \end{cases} \quad (6.17)$$

$$s(t, 0) = t; t = 0, \dots, n; k = 0, \dots, m-1.$$

The conditions for reporting a matching subsequence including disjoint query are similar to SPRING conditions.

As described above, this algorithm contains two extra loops of normalizations and distance calculations in order to apply the mapping required to optimize the normalization. Therefore, it has higher computational cost in comparison to SPRING.

## 6.3. Proposed method

In this work on the basis of SPRING a method is proposed to increase the temporal and spatial efficiency, while maintaining the accuracy, specifically for the application of exercise identification. As discussed in the previous sections, the proposed optimizations of online DTW-based approaches lack the consideration for multidimensional input data. This impedes applying such methods for strength exercise monitoring, where the motion signals, including multiple DOFs, define a correctly performed exercise. Therefore, the proposed method optimizes SPRING to support multidimensional data by exploiting the common characteristics of the motion signals based on two concepts of motion primitive detection and feature extraction. These concepts and the procedure of identification are explained in the following sections.

### 6.3.1. Motion primitive detection

Since a strength exercise usually contains a periodic pattern in which the velocity of movement increases and decreases sequentially, the Zero Velocity Crossing (ZVC) method is chosen to detect the motion primitives in both query and streaming signal. Therefore, a motion primitive is detected, where the sign of derivative is changing on the dominant DOF of motion signals, e.g. positions or joint angles. The derivative is calculated here, with a numerical differentiation over a sliding window. This causes a delay in reporting the identified movements i.e. half of the window length. However, to detect the motion primitives where the velocity changes abruptly, this window length needs to be small. Consequently, the delay is small as well. The dominant DOF is selected on each dataset by finding a dimension of the query signal, which has the highest standard deviation and thus the greatest variations. The detected motion primitives in a query of joint angles are presented in Figure 6.1, where the knee joint angle is a dominant DOF.

### 6.3.2. Feature extraction

The features including velocity, variance, and mean value are selected in this approach, Figure 6.1, as they define the movements by introducing the higher level information from the original motion signals. These features are calculated from each DOF of motion primitive. Therefore, for each motion primitive, tens of position or joint angle samples, as the input to the online identification algorithm, are reduced to three features in each dimension. This, as shown in the experimental results, has highly increased the speed of the identification algorithm while maintaining its accuracy.

### 6.3.3. Identification

The proposed identification method is described in Algorithm 1. Using the approach described in Section 6.3.1, the dominant DOF is determined from the query. This is used in the ZVC method to detect the motion primitives associated with each DOF (see Algorithm 2), both in the query and in the streaming motion signal. The features, including mean and variance are calculated incrementally and extracted after a motion primitive is detected. For velocity the incremental calculation is not applied, as the higher number of points involved in the numerical differentiation leads to less error [81]. For each motion primitive, all types of features from all DOFs generate a feature vector. This is achieved by Algorithms 3 and 4. The latter explains the velocity calculation in which one of the three different numerical differentiation techniques, i.e. five-point stencil, symmetric and Newton's quotient [81], are applied depending on number of sample points available. This number in the motion primitive detection is equal to the half of the length of sliding window and in the feature extraction is equal to the number of samples in each motion primitive. The feature vectors together with the timestamps of their associated motion primitives are used to calculate the distance required for DTW in SPRING approach (Section 6.2.1); In Equation 6.3,  $y_i$  and  $x_t$  can each be replaced by the feature vector of the motion primitive  $i$  in the query signal and of the motion primitive  $t$  in the streaming signal.

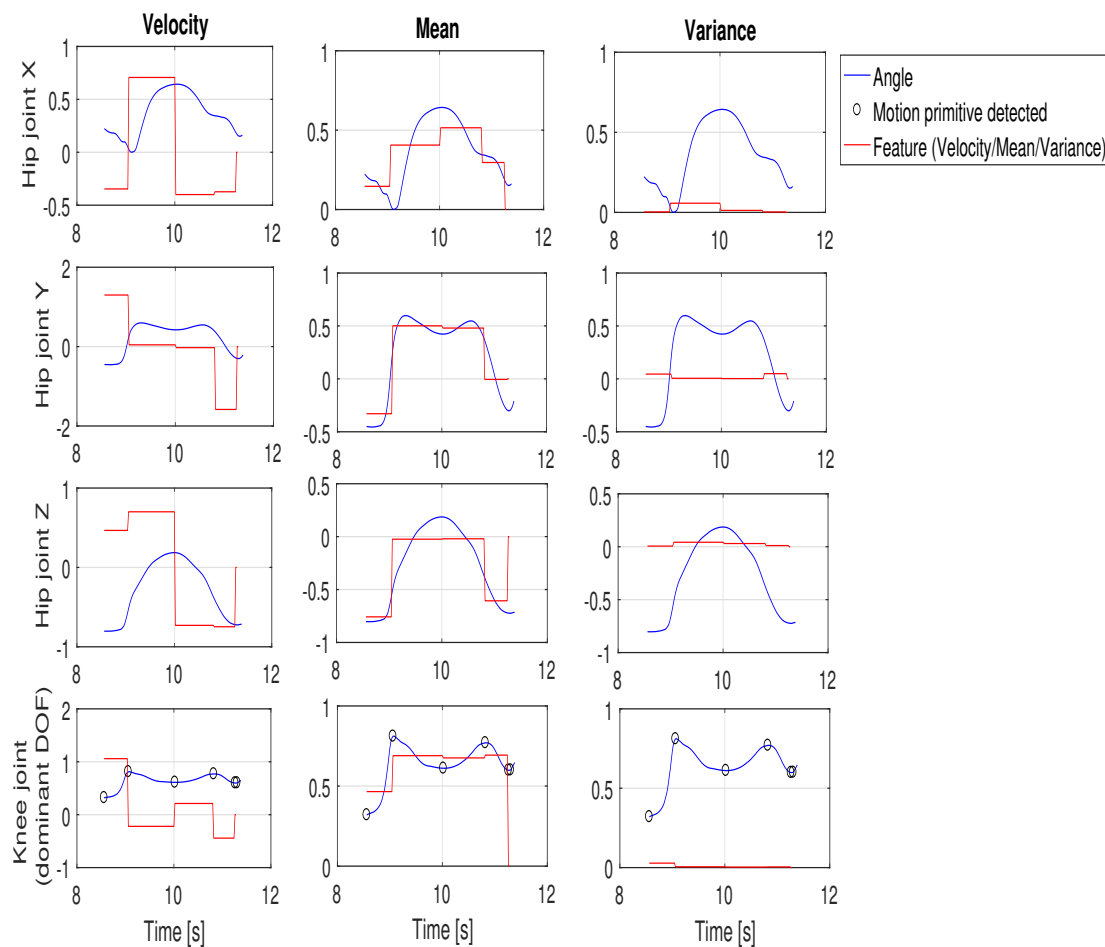


Figure 6.1.: Feature extraction of query signal using the proposed method. The query contains 4DOF joint angles captured during a squat exercise. Each DOF is defined by three different features: velocity, mean, and variance. These are correlated with each detected motion primitive. The detection motion primitives are presented by the black circle markers on the knee joint angle, as it has the highest variance and serves as a dominant DOF.

**Algorithm 1** Proposed Exercise Identifier**Initialization:**

determine the dominant degree of freedom,  $DOF_d$

set  $len$  to half of the length of sliding window rounded up, i.e.  $\text{ceiling}(WinLength/2)$

**Input:** a new value of  $x_t$

**Output:** start and stop points of a matched subsequence if any

```

1:  $sum1 = sum1 + x_t$ ;
2:  $sum2 = sum2 + x_t^2$ ;
3: Insert  $sum1$  in  $S1$ ;
4: Insert  $sum2$  in  $S2$ ;
5: Insert  $x_t$  in  $S$ ;
6: Insert  $t$  in  $T$ ;
7:  $ls = \text{length}(S)$ ;
8: if  $ls > len$  then
9:    $v_t = \text{CalculateVelocity}(S(ls - len : ls, DOF_d), T(ls - len : ls, DOF_d))$ ;
10:  Insert  $v_t$  into  $V$ ;
11: end if
12: if  $\text{length}(V) == len + 1$  then
13:   if  $\text{MotionPrimitiveDetected}(V(1), V(len + 1))$  then
14:      $\text{CurrentSpringTime} = T(ls - len)$ ;
15:      $f = \text{FeatureExtraction}(S, T, S1(ls - len), S2(ls - len), ls - len)$ ;
16:      $[F_{Matched}, t_{start}, t_{stop}, d_{min}] = \text{SPRING}(f, \text{CurrentSpringTime}, t_{start}, t_{stop}, d_{min})$ ;
17:     if  $F_{Matched}$  then
18:       return  $t_{start}, t_{stop}, d_{min}$ ;
19:     end if
20:      $S = S1(ls - len : ls)$ ;
21:      $S1 = S1(ls - len : ls) - S1(s - len - 1)$ ;
22:      $S2 = S2(ls - len : ls) - S2(s - len - 1)$ ;
23:      $sum1 = S1(len)$ ;
24:      $sum2 = S2(len)$ ;
25:      $V = V(len)$ ;
26:   else
27:     delete  $V(1)$  from  $V$ ;
28:   end if
29: end if

```

**Algorithm 2** MotionPrimitiveDetected

**Input:**  $V_{prev}, V_{current}$

**Output:** True if it is detected and False otherwise.

$\epsilon = 1e^{-5}$ ;

**return**  $(V_{prev} \leq \epsilon \text{ and } V_{current} \geq \epsilon) \text{ or } (V_{prev} \geq \epsilon \text{ and } V_{current} \leq \epsilon)$ ;



**Algorithm 3** FeatureExtraction**Input:**  $S, T, S1, S2, len_{average}$ **Output:** feature vector

- 1:  $f(1 : DataDimension) = calculateVelocity(S, T);$
- 2:  $Mean = S1/len_{average};$
- 3:  $f(DataDimension + 1 : 2 * DataDimension) = Mean;$
- 4:  $f(2 * DataDimension + 1 : 3 * DataDimension) = S2/len_{average} - Mean^2;$
- 5: **return**  $f;$

**Algorithm 4** CalculateVelocity**Input:**  $S, T$ **Output:** Average velocity of S.

- 1:  $ls = length(S);$
- 2: **for**  $i \leftarrow 1$  to  $DataDimension$  **do**
- 3:      $v(i) = 0, counter = 0;$
- 4:     **if**  $ls \geq 5$  **then**
- 5:         **for**  $j \leftarrow 3$  to  $ls - 2$  **do**
- 6:              $h = T(j) - T(j - 1)$
- 7:             //five-point stencil
- 8:              $v(i) = v(i) + (S(j-2, i) - 8*S(j-1, i) + 8*S(j+1, i) - S(j+2, i))/(12*h);$
- 9:              $counter = counter + 1;$
- 10:         **end for**
- 11:         **else if**  $ls \geq 3$  **then**
- 12:             //symmetric difference quotient
- 13:             **for**  $j \leftarrow 2$  to  $ls - 1$  **do**
- 14:                  $h = T(j) - T(j - 1)$
- 15:                  $v(i) = v(i) + (S(j + 1, i) - S(j - 1, i))/(2 * h);$
- 16:                  $counter = counter + 1;$
- 17:             **end for**
- 18:         **else if**  $ls == 2$  **then**
- 19:             //Newton's difference quotient
- 20:              $h = T(2) - T(1)$
- 21:              $v(i) = (S(2, i) - S(1, i))/h;$
- 22:              $counter = 1;$
- 23:         **end if**
- 24:          $v(i) = v(i)/counter;$
- 25:     **end for**
- 26: **return**  $v$

## 6.4. Experimental Results

Five online template matching methods described before, are implemented and evaluated in Matlab to identify the strength exercise of squat in a stream of motion signal. The input data is the result of lower body estimated pose using the approach explained in Chapter 5, during an experiment with 7 subjects, in which they performed squat exercises together with other movements. In this experiment, the first squat, which was performed on the instruction of a supervisor, served as a template to identify the next repetitions in the streaming motion signal. After squats, the subjects performed other movements. Figure 6.2 shows an example of streaming data including joint angles and leg segment positions. This example has been used for a detailed analysis in the evaluation of all methods, unless for the case of ISPRING, where the algorithm fails to identify any true positives in this signal. In this case, a different example is selected for further analysis.

Streaming signals in all the test trials from all subjects contain some random movements and similar exercises such as squats, hip abduction/adductions, knee flexion/extensions, etc. The signal duration is, on average, 1 minute, which means receiving around 6000 samples. The execution time of each method is measured using TIC function in Matlab, which includes the processing time of query normalization and feature extraction in addition to stream data identification. For the proposed method the time to detect the dominant DOF is also considered in execution time.

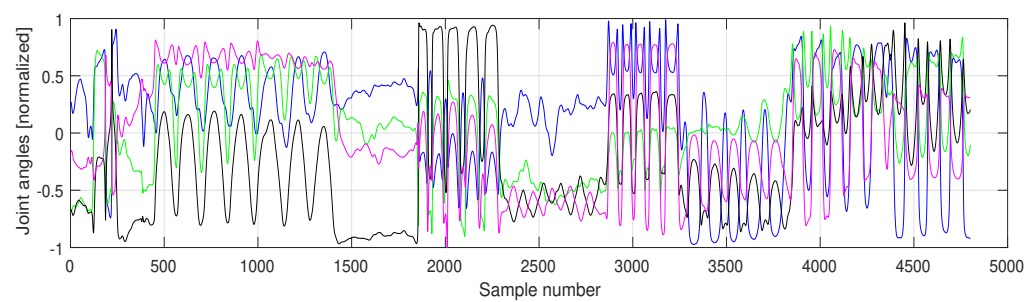
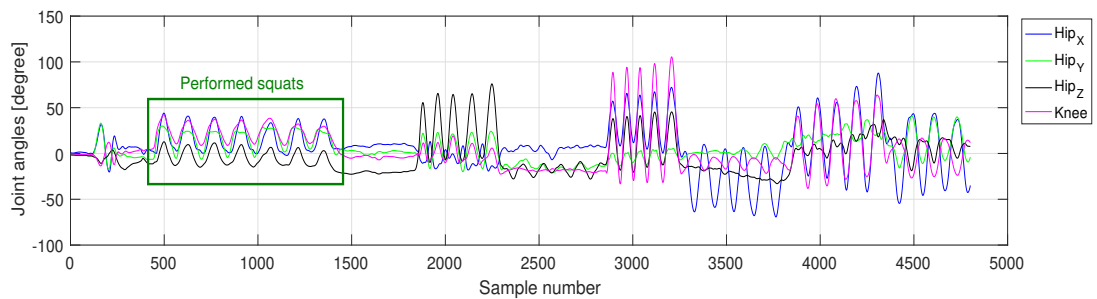
The common performance metrics, accuracy, precision, recall, and  $F1$  score are measured based on the comparison of algorithmic and manual identification. This comparison provides the number of true positives ( $TP$ ), false positives ( $FP$ ), true negatives ( $TN$ ), and false negatives ( $FN$ ) out of the total number of features in the streaming signal. These are used in the following formulas in order to calculate those metrics:

$$Accuracy = \frac{TP + TN}{total} \quad (6.18a)$$

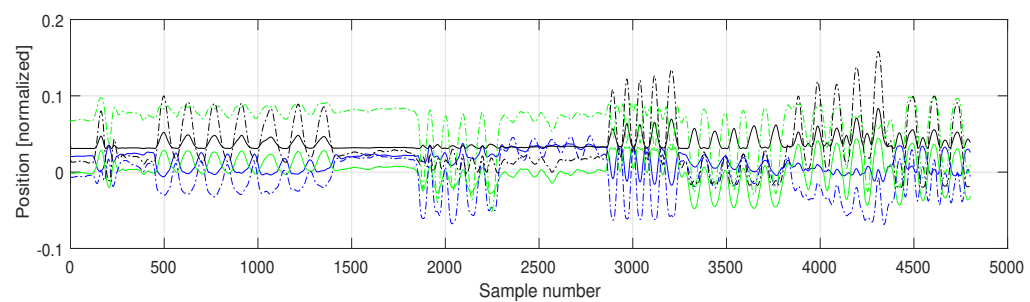
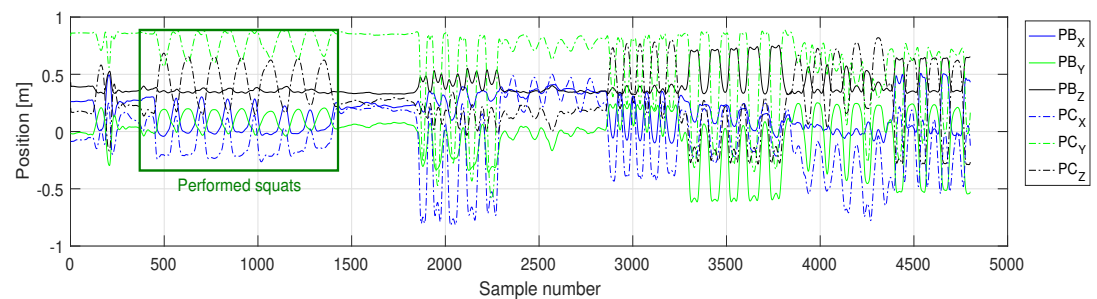
$$Precision = \frac{TP}{TP + FP} \quad (6.18b)$$

$$Recall = \frac{TP}{TP + FN} \quad (6.18c)$$

$$F1score = \frac{2 \times Recall \times Precision}{Recall + Precision} \quad (6.18d)$$



(a) Hip and knee joint angles



(b) leg segment positions

Figure 6.2.: An example of streaming signal captured during performing squats and other types of movements.

For a fair comparative evaluation, all the methods which include the disjoint query are tuned for the threshold  $\epsilon$  in the inequality of 6.5 and separately for each type of movement, so that they identify at least one  $TP$  in three of the trials. The tuning starts with a value in the range of the distances in the middle of STWM column and increasing it till a  $TP$  is found. The following sections present the evaluation of the results of each method.

### 6.4.1. Identification with SPRING

SPRING method is implemented here as proposed in [116]. Therefore, no feature extraction is required. However, to have the same range in all DOFs, each vector sample of joint angles, including hip and knee joint, is normalized.

The method is used for squat exercise identification with three different types of motion signals: 1DOF: only knee joint angle, 4 DOF: hip and knee joint angles, 6DOF: upper and lower leg segment positions. Results in terms of performance metrics and execution time are presented in Tables 6.1, 6.2, and 6.3. The best performance is related to test with the position signals as the squat can be identified better, among other movements, by incorporating more DOFs. As expected, the execution time for processing 1DOF is less than the other tests.

For a detailed analysis of the process of online DTW, embedded in SPRING method, the STWM matrix is visualized in Figure 6.3, where the darker colour indicates lower values, and the lighter colour higher values. This is collected from the test with 4DOF joint angles. It can be easily noticed there's a high amount of data, which should be processed at each sample arrival in order to update all the values in a related column. This is one of the disadvantages of SPRING which leads to high execution time especially when the query is large.

Moreover, in this example the algorithm fails to identify the fourth and seventh performed squats. This can be due to a slight difference in the amplitude of the second DOF,  $hip_Y$ , at the end of the movement, where it has a delay to rise from its minimum compared to other DOFs. This is visible in 6.3, where the STWM column after the identified subsequence is only light in the middle and not in the lower area, where the distances to the end of query exist. This as well delays reporting the identification due to disjoint query as the algorithm searches for a better transition in the shape of the signal. As the experiment with the proposed method in Section 6.4.5 shows, such amplitude deficiencies do not influence the result as other high level features are involved in the identification process.

	Squat						
	subj. 1	subj. 2	subj. 3	subj. 4	subj. 5	subj. 6	subj. 7
Accuracy[%]	99.9	99.9	99.9	99.8	99.9	99.8	99.5
Precision[%]	50.0	50.0	71.4	40.0	60.0	40.0	16.0
Recall[%]	50.0	40.0	100.0	80.0	85.7	80.0	80.0
F1 Score[%]	50.0	44.4	83.3	53.3	70.6	53.3	26.6
Execution Time[s]	3.16	1.98	1.76	1.16	1.60	2.80	1.42

Table 6.1.: Squat identification with knee joint angle based on SPRING method.

	SPRING						
	subj. 1	subj. 2	subj. 3	subj. 4	subj. 5	subj. 6	subj. 7
Accuracy[%]	99.4	99.7	99.4	99.8	99.6	99.9	99.9
Precision[%]	100.0	31.2	100.0	40.0	100.0	100.0	83.3
Recall[%]	25.0	100.0	40.0	80.0	71.0	40.0	100.0
F1 Score[%]	40.0	47.6	57.1	53.3	83.3	57.1	90.9
Execution Time[s]	3.22	2.58	2.29	1.43	2.08	3.56	1.77

Table 6.2.: Squat identification with knee and hip joint angles based on SPRING method.

	SPRING						
	subj. 1	subj. 2	subj. 3	subj. 4	subj. 5	subj. 6	subj. 7
Accuracy[%]	99.9	99.9	99.9	99.9	99.9	99.9	99.9
Precision[%]	100.0	100.0	100.0	100.0	100.0	100.0	83.3
Recall[%]	50.0	80.0	60.0	60.0	42.8	20.0	100.0
F1 Score[%]	66.6	88.8	75.0	75.0	60.0	33.3	90.9
Execution Time[s]	2.97	1.90	2.08	1.45	2.31	3.71	1.44

Table 6.3.: Squat identification with leg positions based on SPRING method.

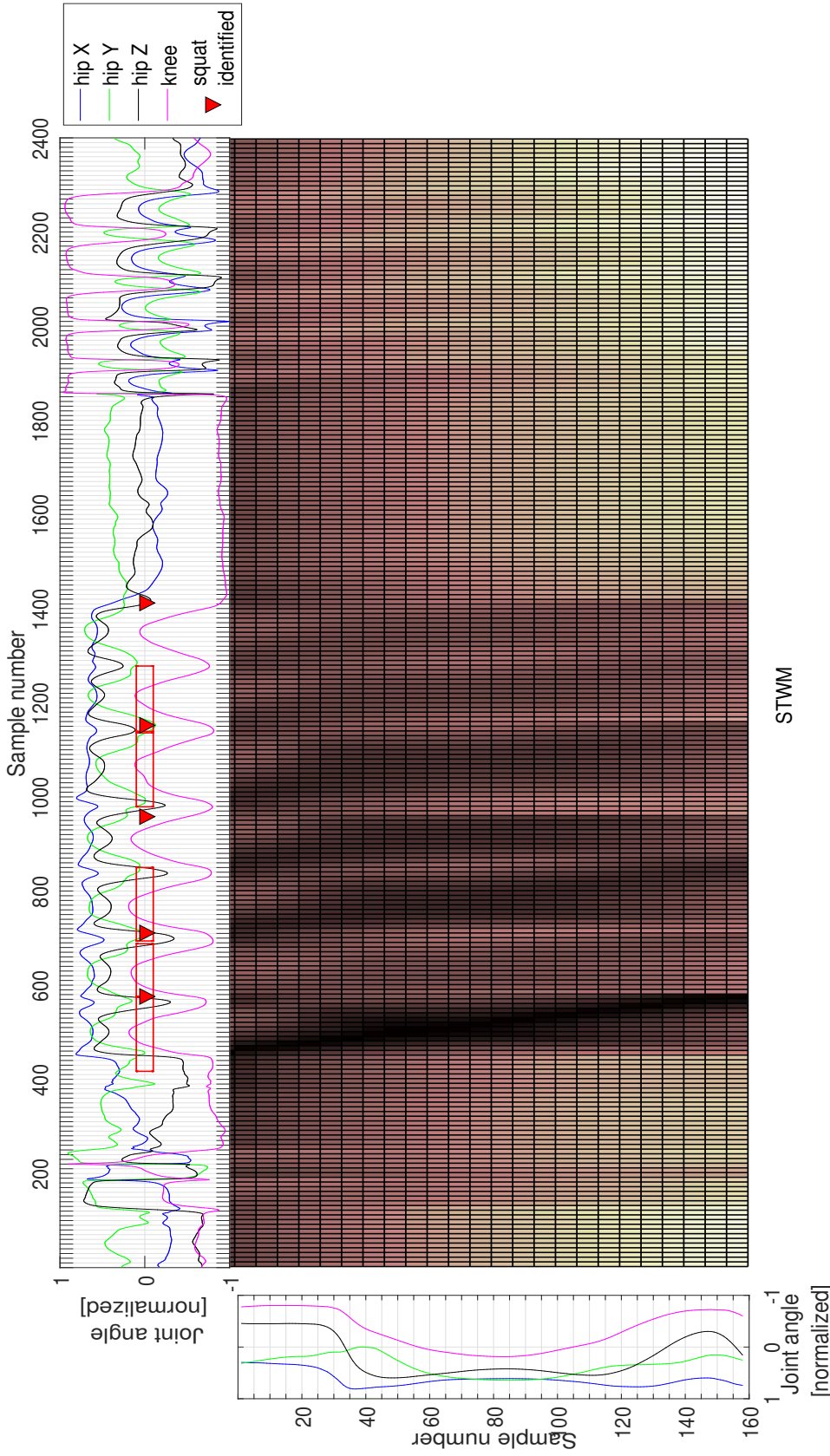


Figure 6.3.: The STWM matrix in SPRING for an experiment with 4DOF joint angles: The values of this matrix, dtw distances, are normalized by the maximum value and presented by a built-in Colormap in Matlab, where darker colours depict the lower values. Therefore, the warping path of a matched subsequence can be identified, where there is a continuous darker area from the first to the last row. For brevity, this matrix is scaled down 10 and 5 times along the row and column. The streaming signal and the query are represented at the top and left side. Note that each joint angle vector is normalized.

### 6.4.2. Identification with ISPRING

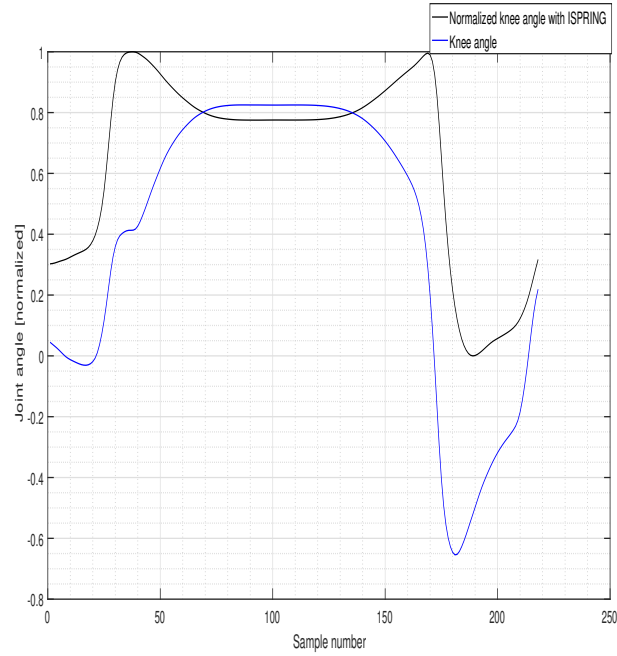
As the search for min-max coefficients in each DOF, which is required for normalization in ISPRING method, affects the warping distance calculations, it is not practical to extend this method for a multidimensional identification. Therefore only knee joint angle is used here as input. This signal is normalized using Equation 6.13 and the current min-max coefficient reported in the monitoring window. The normalization results in a modified range for both streaming signal and query, which degrades the identification performance as a specific range of motion at knee mainly defines the squat exercise. Therefore, as shown in Figure 6.4, the random movements before the main exercise are identified falsely as squats. If the length of the subsequence candidate is less than the query, as it could be the case when the subject performs squats with different speeds, it leads to a distorted normalized signal as shown in the example of Figure 6.4, which leads to fail identifying the first squat. This is due to assuming a fixed-length window for the min-max coefficient search.

Moreover, since the disjoint query proposed in SPRING is not supported in ISPRING, there are many overlapped matching subsequences, Figure 6.4. This is considered in the calculation of performance metrics by discarding all the overlapped identified subsequences in one area.

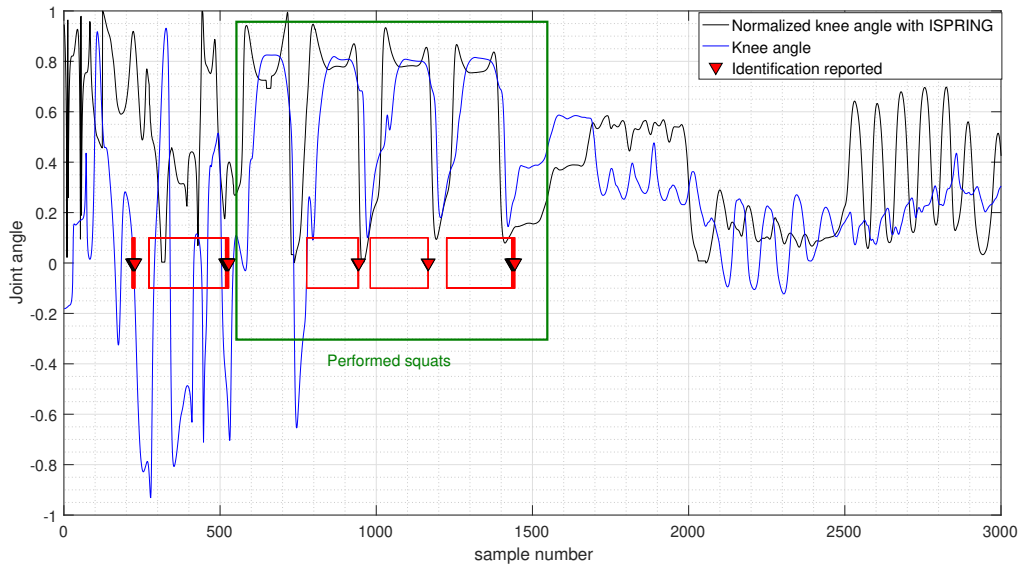
It can be noticed that the execution time in all trials is less than SPRING method as ISPRING does not include the search for disjoint query. Also, the min-max coefficient search is optimal by deploying Binary search and Quicksort functionalities as described in [42].

	Squat						
	subj. 1	subj. 2	subj. 3	subj. 4	subj. 5	subj. 6	subj. 7
Accuracy[%]	92.5	95.32	91.52	92.63	78.94	96.47	50
Precision[%]	60.0	50.0	50.0	25.0	0	75.0	0
Recall[%]	75.0	20.0	20.0	20.0	0	60	0
F1 Score[%]	66.66	28.57	28.57	22.22	0	66.66	0
Execution Time[s]	2.32	1.58	1.14	0.71	2.19	1.14	1.07

Table 6.4.: Squat identification with knee joint angle based on ISPRING method. Note that for a better comparison of the metrics with the other methods, the overlapping matches in one area, for both false positives and true positives, were counted as one.



(a) Normalized versus original knee joint angle of a squat exercise used as a query signal in ISPRING.



(b) Normalized versus original knee joint angle of squats and other types of movements used as a streaming signal in ISPRING.

Figure 6.4.: ISPRING normalization



### 6.4.3. Identification with NSPRING

The normalized signal according to NSPRING method is calculated using  $\frac{x_{t'} - M(t', i)}{SD(t', i)}$  in the Equation 6.8. In this experiment, the normalization results in the inconsistency, which is caused by extremely small standard deviations and division by such values. This problem is resolved to some extent by considering a lower bound of  $10^{-6}$  and resetting to this value when the standard deviation is lower. Note that in the test with 4DOF joint angles, these values are not normalized as it caused similar numerical problems. Figure 6.5 shows this problem, which causes the query and streaming signals to not always be in the same range in contrast to what is expected from a normalization process. As a result, the overall performance of this method is worse than SPRING while the execution time is higher especially for 4DOF data, 6.6. This is due to four added lists of  $M$  and  $SD$  for each DOF, which have to be maintained and/or updated at receiving each new sample. Moreover, as described in Section 6.2.2, there is an inherit delay in reporting the identification, Figure 6.5. The result here is not compatible with [43] since they claimed that they achieve the same results as SPRING. However, they used different performance metrics and input signals for their evaluations, which could justify this different outcome.

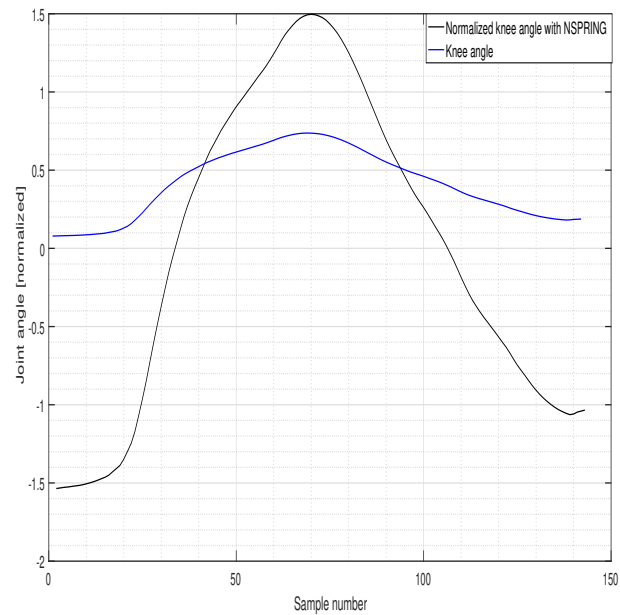
This method is evaluated for both one dimensional and multidimensional joint angle signals, 6.5, 6.6, as well as for multidimensional leg segment position signal. The latter is not presented here, due to the poor performance of this algorithm, where the  $\epsilon$  threshold tuning process fails to achieve any true positives in any of the trials.

	NSPRING						
	subj. 1	subj. 2	subj. 3	subj. 4	subj. 5	subj. 6	subj. 7
Accuracy[%]	99.87	99.85	99.74	99.72	99.91	99.89	99.70
Precision[%]	25.0	0	0	16.67	80.0	0	9.09
Recall[%]	25.0	0	0	40.0	57.14	0	20.0
F1 Score[%]	25.0	0	0	23.53	66.67	0	12.50
Execution Time[s]	3.61	2.83	2.50	1.65	3.13	3.83	2.04

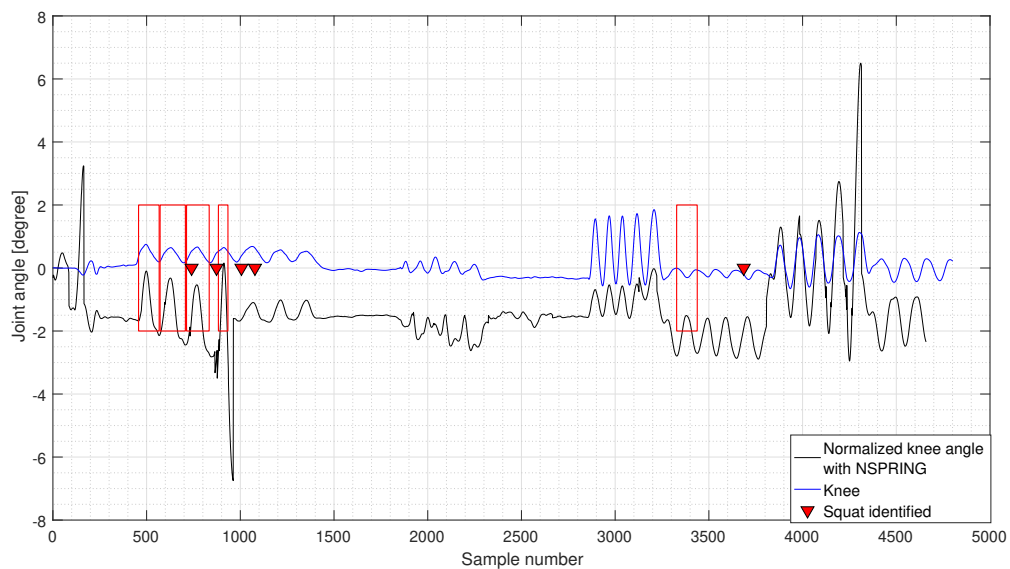
Table 6.5.: Squat identification with knee joint angle based on NSPRING method.

	NSPRING						
	subj. 1	subj. 2	subj. 3	subj. 4	subj. 5	subj. 6	subj. 7
Accuracy[%]	99.91	99.89	99.91	98.26	99.79	99.82	99.25
Precision[%]	0	0.5000	66.67	5.75	41.18	0	10.53
Recall[%]	0	20.0	40.0	100.0	100.0	0	80.0
F1 Score[%]	0	28.57	50.0	10.87	58.33	0	18.60
Execution Time[s]	7.90	6.23	5.30	4.01	5.10	8.40	4.32

Table 6.6.: Squat identification with knee and hip joint angles based on NSPRING method.



(a) Normalized versus original knee joint angle of a squat exercise used as a query signal in NSPRING.



(b) Normalized versus original knee joint angle of squats and other types of movements used as a streaming signal in NSPRING.

Figure 6.5.: NSPRING normalization

#### 6.4.4. Identification with DNRTPM

The normalization process of DNRTPM is evaluated using the knee joint angle. The similar problem of numerical inconsistency in NSPRING is evident in the normalized signal by DNRTPM as they both apply z-score normalization, Figure 6.6. However, the precision here is slightly better, see Table 6.7, as the z-score normalization is refined using amplification and offset correction proposed in Equation 6.14.

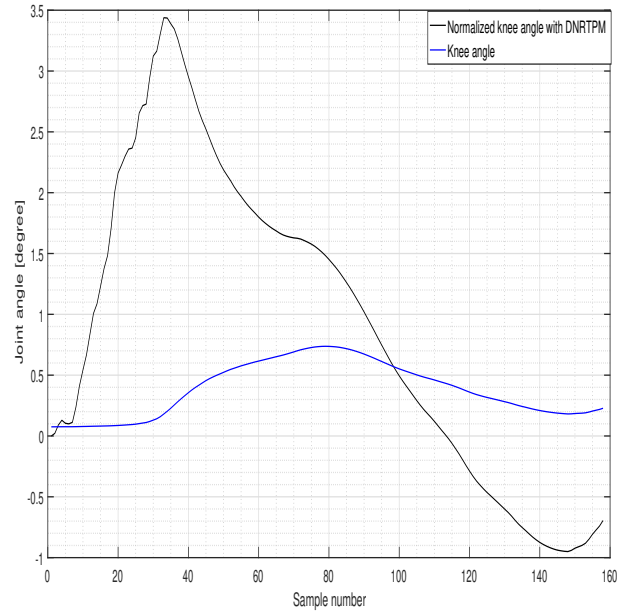
This algorithm is further developed to be used for multidimensional joint angles and leg segment positions. The results are presented in Tables 6.8, 6.9. The overall execution time is much higher than other evaluated methods in this chapter. The reason is that this method goes through three loops over all the samples in the query to find the best normalized distance as defined by Equation 6.16. Although this method offers an interesting approach for the dynamic normalization by integrating it in an online DTW, it is not practical, specifically for a real time exercise identification due to its numerical failures and high execution time.

	DNRTPM						
	subj. 1	subj. 2	subj. 3	subj. 4	subj. 5	subj. 6	subj. 7
Accuracy[%]	99.90	99.90	99.81	99.90	99.63	99.92	99.92
Precision[%]	33.33	0	16.67	0	26.09	100.0	100.0
Recall[%]	25.0	0	20.0	0	85.71	20.0	20.0
F1 Score[%]	28.57	0	18.18	0	40.0	33.33	33.33
Execution Time[s]	26.65	21.48	19.32	13.89	19.46	32.95	16.64

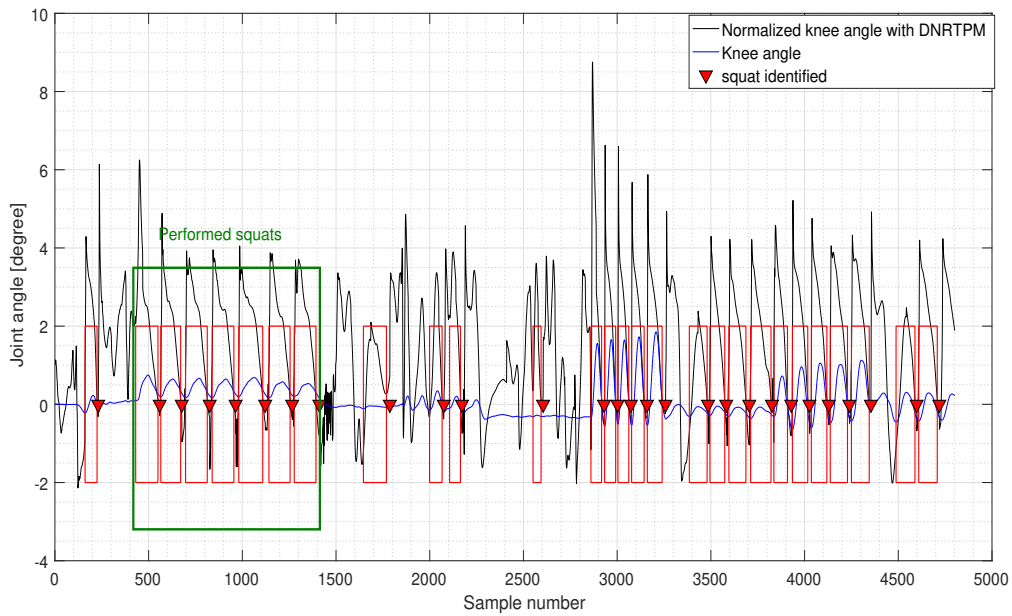
Table 6.7.: Squat identification with knee joint angle based on DNRTPM method.

	DNRTPM						
	subj. 1	subj. 2	subj. 3	subj. 4	subj. 5	subj. 6	subj. 7
Accuracy[%]	99.92	99.90	99.77	99.44	99.85	99.90	99.77
Precision[%]	0	0	31.25	15.63	0	0	12.50
Recall[%]	0	0	100.0	100.0	0	0	20.0
F1 Score[%]	0	0	47.62	27.03	0	0	15.38
Execution Time[s]	35.71	29.24	24.75	16.21	23.25	41.04	19.98

Table 6.8.: Squat identification with knee and hip joint angles based on DNRTPM method.



(a) Normalized versus original knee joint angle of a squat exercise used as a query signal in DNRTPM.



(b) Normalized versus original knee joint angle of squats and other types of movements used as a streaming signal in DNRTPM.

Figure 6.6.: DNRTPM normalization

	DNRTPM						
	subj. 1	subj. 2	subj. 3	subj. 4	subj. 5	subj. 6	subj. 7
Accuracy[%]	99.63	99.33	99.50	99.90	99.67	99.90	97.25
Precision[%]	6.25	9.09	17.24	0	23.53	0	3.65
Recall[%]	25.00	60.00	100.00	0	57.14	0	100.00
F1 Score[%]	10.00	15.79	29.41	0	33.33	0	7.04
Execution Time[s]	33.59	21.88	23.18	19.64	27.04	43.63	14.99

Table 6.9.: Squat identification with leg positions based on DNRTPM method.

### 6.4.5. Identification with the proposed method

The proposed method, as described in Section 6.3 is developed and evaluated here for squat identification using different types of motion signals i.e. joint angles and leg segment positions. In this experiment, the length of sliding window is selected to be five as this reduces the velocity calculation for ZVC to one simple equation of symmetric quotient difference from three points, i.e.  $\text{ceiling}(5/2)$ .

The extracted features for both query and streaming signal are presented in Figure 6.7 and 6.8. Each feature contains a higher level of information than the original signal, which further minimizes the DTW. This can be realized by comparing the features related to different movements in Figure 6.7 and 6.8. Therefore, the identification performance is comparable with SPRING and higher than all the other methods as presented in Table 6.10 to Table 6.12. The exception here is the performance of SPRING method for position signals, which is higher than the proposed method. This can be due to minimal values of variance compared to other features. Further evaluation of different features and their effectiveness in the process of exercise identification is the subject of future work.

Each DOF adds three types of features. Therefore, for the case of 4DOF joint angles and 6DOF position signals the vector length is 12 and 18 respectively. The results in Tables 6.11 and 6.12 verify that this does not affect the execution time, as the proposed motion primitive detection technique in Section 6.3 reduces the number of times in which a column in STWM needs to be updated. As the length of query is reduced to its motion primitives, this results in further improvement of execution time as the number of distance calculations and the search path for disjoint query is shorter than the original signal.

Figure 6.9 provides a detailed analysis on how the STWM matrix is established in this method. In comparison to Figure 6.3 for the same signal, this matrix has a smaller size, and therefore less content. This yields to less space and time complexity. Moreover, the proposed method does not fail to identify the subsequence with a different amplitude, as was the case for the test of SPRING method with the same signal.

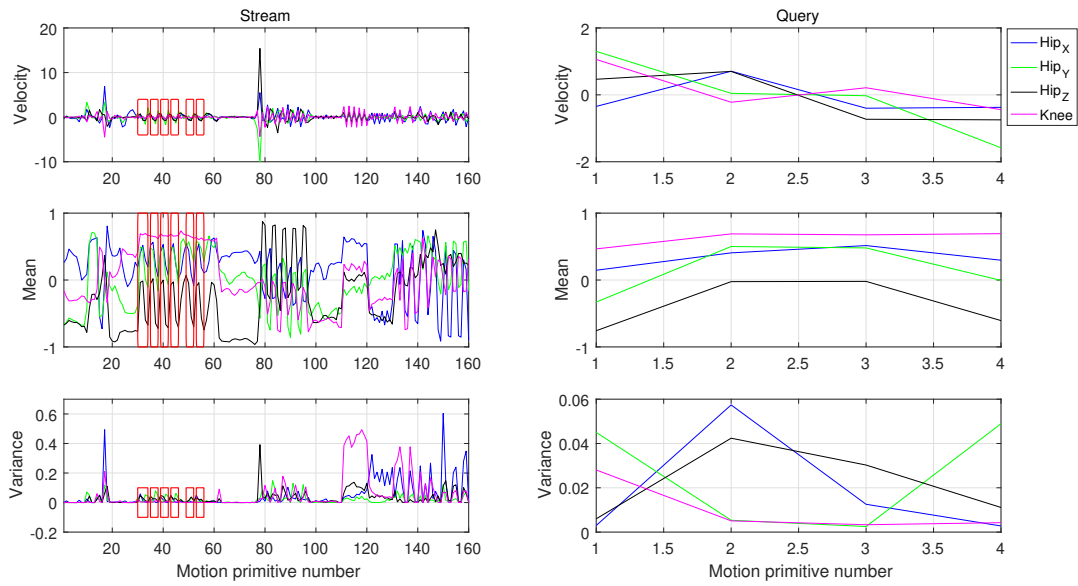


Figure 6.7.: Feature extraction from the hip and knee joint angles using the proposed method. The features extracted from the joint angles in motion primitives of the streaming signal presented at left and query at right.

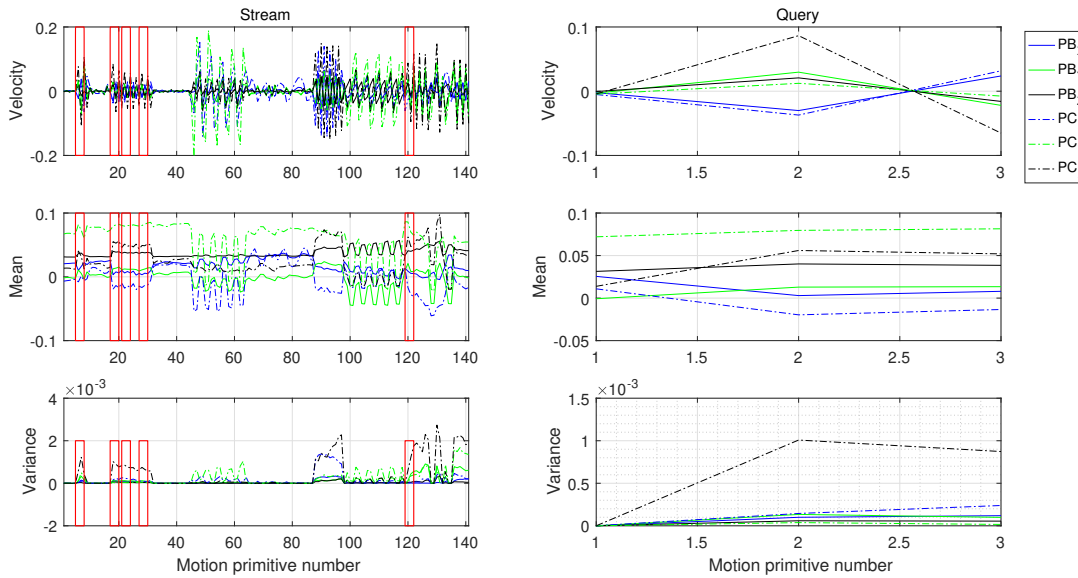


Figure 6.8.: Feature extraction from the leg positions using the proposed method. The features extracted from the leg segment positions in motion primitives of the streaming signal presented at left and query at right.

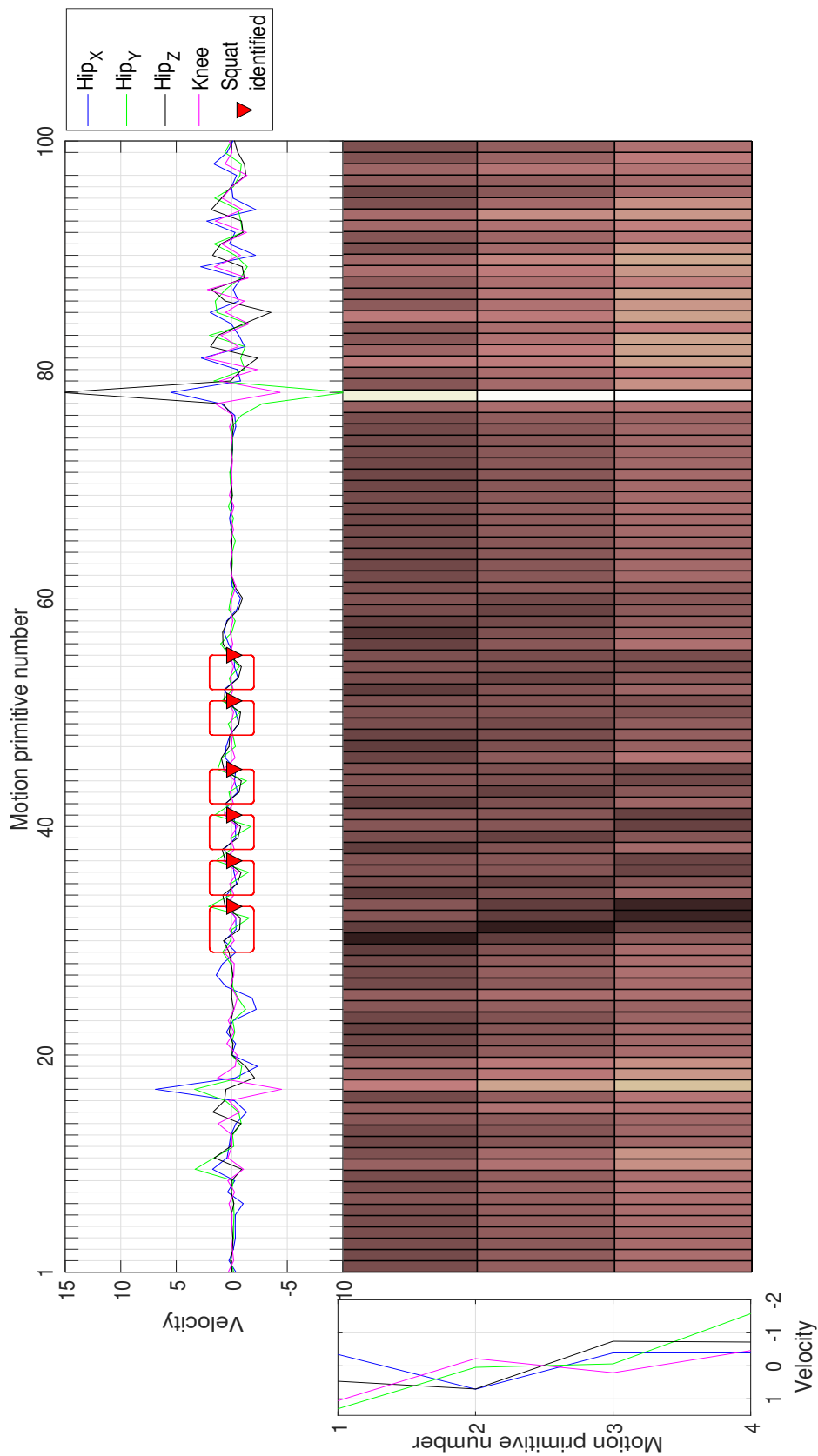


Figure 6.9.: The STWM matrix in the proposed method for an experiment with 4DOF joint angles: The values of this matrix, dtw distances, are normalized by the maximum value and presented by a built-in Colormap in Matlab, where darker colours depict the lower values. Therefore, the warping path of a matched subsequence can be identified, where there is a continuous darker area from the first to the last row. The number of rows and columns presented here correspond with the actual matrix, as a result of dimension reduction offered by the motion primitive technique in the proposed. The extracted features of streaming signal and the query are represented at the top and left side.

	subj. 1	Proposed subj. 2	method subj. 3	subj. 4	subj. 5	subj. 6	subj. 7
Accuracy[%]	97.92	97.52	97.58	96.09	90.16	96.67	98.37
Precision[%]	100.0	100.0	100.0	50.0	27.27	50.0	66.67
Recall[%]	25.00	20.0	20.0	40.0	42.86	20.0	40.0
F1 Score[%]	40.00	33.33	33.33	44.44	33.33	28.57	50.0
Execution Time[s]	0.24	0.11	0.11	0.10	0.09	0.08	0.11

Table 6.10.: Squat identification with knee joint angle based on the proposed method.

	subj. 1	Proposed subj. 2	method subj. 3	subj. 4	subj. 5	subj. 6	subj. 7
Accuracy[%]	98.35	70.18	98.27	100.0	99.38	98.29	98.90
Precision[%]	100.0	4.00	100.0	100.0	100.0	75.0	62.50
Recall[%]	25.0	40.0	20.0	100.0	85.71	60.0	100.0
F1 Score[%]	40.0	7.27	33.33	100.0	92.31	66.67	76.92
Execution Time[s]	0.27	0.20	0.17	0.14	0.18	0.17	0.14

Table 6.11.: Squat identification with knee and hip joint angles based on the proposed method.

	subj. 1	Proposed subj. 2	method subj. 3	subj. 4	subj. 5	subj. 6	subj. 7
Accuracy[%]	98.72	97.98	98.97	98.15	95.74	97.84	98.17
Precision[%]	100.0	100.0	100.0	100.0	60.0	100.0	66.67
Recall[%]	50.0	20.00	60.0	20.0	42.86	20.0	40.0
F1 Score[%]	66.67	33.33	75.0	0.33	50.0	33.33	50.0
Execution Time[s]	0.30	0.22	0.18	0.16	0.21	0.17	0.18

Table 6.12.: Squat identification with leg positions based on the proposed method.



### 6.4.6. Performance comparison

The average of the performance metrics of each method over all the trials and separately for different types of input signals are presented in Tables 6.14 to 6.15. This result verifies that the proposed method outperforms all the other method in terms of execution time while DNRTPM has the worst time performance. The precision of the proposed method outperforms the other methods in the case of test with the knee angle, while in this test SPRING has the highest recall rate. In the case of 4DOF joint angles SPRING method has the best performance while DNRTPM has the worst. The accuracy related result of proposed method is slightly worse than SPRING in the multidimensional cases.

	Accuracy[%]	Precision[%]	Recall [%]	F1 Score[%]	Execution [s] time
SPRING	99.85	46.78	73.67	54.53	1.98
ISPRING	85.34	37.14	27.80	30.38	1.45
NSPRING	99.81	18.68	20.31	18.24	2.80
DNRTPM	99.85	39.44	24.39	21.92	21.49
Proposed method	96.33	70.56	29.69	37.57	0.12

Table 6.13.: Squat identification with the knee joint angle.

	Accuracy[%]	Precision[%]	Recall [%]	F1 Score[%]	Execution [s] time
SPRING	99.91	79.23	65.20	61.35	2.42
NSPRING	99.55	24.88	48.57	23.77	5.90
DNRTPM	99.79	8.48	31.43	12.86	27.17
Proposed method	94.77	77.36	61.53	59.50	0.18

Table 6.14.: Squat identification with hip and knee joint angles.

	Accuracy[%]	Precision[%]	Recall [%]	F1 Score[%]	Execution [s] time
SPRING	99.95	97.62	58.98	69.97	2.26
DNRTPM	99.31	8.54	48.88	13.65	26.28
Proposed method	97.94	89.52	36.12	48.81	0.22

Table 6.15.: Squat identification with leg positions.

## 6.5. Conclusion

This chapter explains the application of online template matching for exercise identification, which provides real-time feedback to users by counting the number of correctly performed exercises. This can also be used to obtain a measure of repetition maximum (RM), which is one of the critical factors in monitoring the strength exercise. To optimize the procedure of online dynamic time warping approaches, a state of the art approach known as SPRING [116], and three modifications of it; ISPRING [42], NSPRING [43] and DNRTPM [152] are explained and analysed.

On the basis of SPRING, and inherit characteristics of motion signals, a new identification method is proposed. This method improves the temporal and spatial complexity of the online DTW-based approaches, by utilizing two concepts of motion primitive detection and feature extraction. Moreover, this method can be easily extended to support higher dimensions of input data, which makes it superior to the other optimization approaches, as they mainly rely on the normalization techniques with high complexities to increase the accuracy. These approaches are evaluated using different motion signals, i.e. hip and knee joint angles and the leg segments' positions for identification of the squat exercise in a streaming motion signal. The results show that the proposed method significantly improves the execution time while maintaining the accuracy. While this method outperforms other optimization approaches, it has comparable results and in some cases slightly worse performance than SPRING, in terms of precision and recall rate. This can be due to a low contribution of some features in the subsequence matching process, as observed for the case of variance feature in the experiments with the position signals. Since the proposed approach leads to high efficiency, the algorithm can be extended with additional features to further improve the accuracy without additional computational cost. Moreover, there are different exercise phases, e.g. concentric and eccentric phases of the squat, that could be identified differently depending on the characteristics or critical features for the correct performance.

## 7. Conclusion

This thesis focuses on the design and development of an IMU-based suit for the application of strength exercise monitoring. The main motivation is to provide critical measures for monitoring strength exercises, which are the essential components in the fitness and rehabilitation process. Recent advances in technology, particularly in inertial sensing and wearable systems, along with the widespread usage of smartphones and social networks, have led to increasing demand for such sport monitoring devices. Such systems, on the one hand, need to be ubiquitous and unobtrusive, available to all types of users, and work for the long possible duration of sporting sessions. Therefore, they must be low-cost and energy-efficient. On the other hand, these systems should provide a reliable estimate of the motion parameters such as body segment positions and joint angles in real-time. To meet these challenges, the previous chapters discussed all steps from the design and development of the hardware to the calibration of the IMU sensors, body-IMU calibration, lower body motion tracking, and exercise identification, and solutions are proposed respectively. These solutions are supported in each topic with experimental evaluation. The concluding results of this work are discussed in Section 7.1. Section 7.2 suggests the future work.

### 7.1. Results

First, a wearable system with an embedded network of IMUs is designed and developed. All system components can be well integrated and hidden in a flexible suit. A novel data acquisition approach is proposed in order to reduce the CPU load. Moreover, a comparative evaluation of the system is presented. The results in terms of power consumption, cost, weight, and sensor measurements, qualify the system for the application of exercise monitoring.

In the next step, before the motion tracking, the system must be calibrated once before and once after mounting the IMUs.

Since magnetometer measurements in the vicinity of ferromagnetic materials can easily be disturbed, their calibration procedure usually requires external equipment or precise information about the external magnetic field. Therefore, a complete in-field and practical magnetometer calibration method is presented and evaluated. The method provides biases, scale factors, and non-orthogonality parameters, taking the advantage of the fact that the magnitude of the true geomagnetic field vector is always constant. This introduces a geometric ellipsoid fitting problem, which is solved in a nonlinear, least-square estimator. Furthermore, the misalignment between inertial sensors and magnetometer is estimated on the basis of a constant inclination assumed in the homogeneous field. Hence, the whole process was carried out without external heading information or additional equipment. Various experiments, in terms of magnitude deviation, heading error, plane projection, and repeatability have shown a high precision of the estimated

parameters with the proposed method.

After the IMUs are integrated into the suit and the user wears the suit, the position of IMUs relative to the body segments and the joint axes relative to the IMU coordinates must be estimated in the body-IMU calibration process. These parameters are the prerequisite for most algorithms for tracking body movements. Therefore, this work presents a novel and practical body-IMU autocalibration method, which is specifically developed for the lower body. At first, a theoretical observability analysis of an existing calibration method is performed, which demonstrates its limited applicability for the hip and knee joints. Based on this, a method is proposed to simultaneously estimate the positions of three IMUs (mounted on the pelvis, upper leg, lower leg) relative to the joints. Both methods are evaluated using two types of movements; Type A, which involves random movements in all directions, and Type B, which involves the separate movements in every possible degree of freedom of each joint. In the experimental evaluation, based on simulated and real data, the proposed method shows a significant improvement in terms of accuracy and robustness, compared to the previous method, especially for suboptimal (low variation) movements during calibration.

Since the global orientation estimation in for type A movements is faulty due to outliers in the accelerometer measurements, an optimal orientation estimation method is proposed, which can be realized using only gyroscope measurements and the measurements of Type B movements. In addition, it is shown that if due to the limited balance or motion ability, only measurements of Type A movements are available, the conditions of observability, in particular angular velocity, can be evaluated to allow a primary quality check of the acquired data and the resulting calibration parameters.

The lower body pose estimation includes two online tracking procedures: pelvis orientation estimation and leg pose estimation with respect to pelvis. In order to estimate the pelvis orientation, an EKF is developed, where the state vector consists of angular velocity, angular acceleration, magnetic disturbances, and orientation. The algorithm is evaluated based measurements taken on the suit worn by subjects and while they were performing squat exercises. This shows the improvements in orientation estimation, resulting from inclusion of angular acceleration and magnetic disturbance in the states compared to a conventional EKF-based orientation estimator.

The leg pose estimation is based on another EKF, where inertial measurements contribute as control inputs. This leads to a reduction of the computational complexity because not in every correction step of the filter do the observation matrices associated with these measurements have to be calculated. This approach proposes an observation model that uses the constraints of the joints and takes into account the joint axes and positions from the body-IMU calibration process.

This approach is evaluated based on measurements of subjects performing squat and abduction/adduction exercises. This provides an accurate estimate of the hip and knee joint angles (average  $\sim 5$  degrees) and the positions of the leg segments (average  $\sim 9$  cm), which can provide critical measures for monitoring strength exercises such as ROM and posture imbalances.

To monitor the strength exercises, the idea is to capture a template signal while instructing users to perform the movements correctly according to their ability and state of health. This template is used in an online template-matching algorithm based on DTW that was evaluated using the joint angles and segment positions estimated by the pose estimation approach, while users performed the squat exercise. This method is optimized using a motion primitive detection technique and feature extraction. The results show that compared to other optimization approaches, the proposed method led to a lower execution time while maintaining a good accuracy. This effectively provides a measure for RM, which is one of the critical factors in monitoring strength exercises.

## **7.2. Future Works**

### **7.2.1. System design**

#### **7.2.1.1. Extension and further miniaturization**

By exploiting the advantages of the proposed method, i.e. those of simplified wiring and low power consumption, the system can be extended with additional IMUs. It is therefore possible to track the details of the core movements, which is of crucial importance in many strength exercises. Furthermore, wearing comfort can be improved by further minimizing the size of the controller unit.

#### **7.2.1.2. User acceptance**

In this work, the system quality is evaluated under different aspects like power consumption, weight, and costs. In addition, a user study on the suit's wearing quality and its flexibility during the exercises helps to further develop the product, taking user acceptance into account.

#### **7.2.1.3. In-situ embedded tracking**

A further future focus of work is the in-situ implementation of the tracking algorithm as this reduces the packet size and thus increases energy efficiency.

### **7.2.2. Calibration**

#### **7.2.2.1. Measurement noise and other uncertainty**

In the body-IMU calibration process, it is assumed that all the measurements are contributing to the same uncertainty. However, considering the IMU noise characteristics, error in calibration of each sensor, and each movement, the problem should assume different uncertainties. Here, varying uncertainties could account not only for different types of movements during calibration, but also, e.g. for varying amounts of garment movements or other soft tissue artifacts due

to different suit materials and styles or different body shapes.

### **7.2.2.2. Experimental observability analysis**

The observability criteria were experimentally verified for most of the trials with calibration movements, in Section 4.3.9.4. However, some exceptions were observed. These are subject to further investigations in the future. In addition, the idea of quality control of the captured data based on observability criteria to obtain better calibration results can be developed with more experiments by more subjects.

### **7.2.2.3. Movement categories**

In the experimental evaluation of this thesis, it is assumed that the subjects are healthy and able to perform the calibration movements at high intensities. This helps to better evaluate the algorithm for extreme situations when the probability of error due to acceleration outliers is high. However, in order to cover different types of applications, especially those related to rehabilitation, the experiments need to be extended to different categories, such as slow, medium, and high intensity. As with the slower movements, there are fewer possibilities of error due to the outliers, but at the same time, fewer variations in movement lead to inaccurate estimates from the optimization problem (see Section 4.3.2), while movements with high intensity for the same duration have more variations with a higher probability of outliers. Therefore, the thresholds for quality control can be estimated differently for each category.

## **7.2.3. Pose Estimation**

### **7.2.3.1. Evaluation using a known magnetic field**

In the proposed approach for pelvis orientation estimation, which is presented in Section 5.1, the estimated magnetic disturbances are evaluated by the magnitude deviation. However, a more accurate assessment can be obtained using a magnetic field from a known source and comparing the estimation in the absence and presence of that source.

### **7.2.3.2. Heading evaluation**

As discussed in Section 5.2, the use of the information obtained from the body-IMU calibration approach and joint constraints for leg pose estimation relaxes the requirement for a reference in the horizontal plane such as the Earth's magnetic field. However, this must be evaluated practically, specifically for exercises that stimulate movements in this plane, such as lateral or medial hip rotation.

### **7.2.3.3. Adaptive noise tuning**

The proposed approach for estimating the leg position can be extended by an adaptive tuning for the measurement noise to optimize the filtering for outliers. Methods such as adaptive Kalman filtering [73], [72], or the combination of Kalman filtering and machine learning in [26], where the dynamic representation of motion and noise models can be learned from data, can be used to further optimize the estimation.

## **7.2.4. Exercise Identification**

### **7.2.4.1. Exercise phase identification**

In the current work, a simple form of phase detection using the estimated knee joint angle and a predefined threshold was implemented to guide the user in performing the exercise (see Section 3.2.3). A more sophisticated approach is to use the identification method in Chapter 6 to identify different phases by taking into account their different characteristics, segments involved, and characteristics that are related or critical to the correct performance of each phase.

### **7.2.4.2. Repeatability**

More experiments over a longer period of time for each subject can help to analyze the repeatability of the identification method and, if necessary, to adjust the threshold for disjoint query accordingly. The result of such experiments is beneficial for rehabilitation processes as the patients' performance may vary depending on the type of injury, fatigue, and stage of recovery.





# A. Abbreviations

**3D** three dimensions. 3, 12, 53, 54, 65, 75, 147

**ACL** anterior cruciate ligament. 11

**ACLR** anterior cruciate ligament reconstruction. 11

**BDNF** Brain-derived neurotrophic factor. 10

**BMI** body mass index. 10

**CoR** center of rotation. 68, 77

**CPU** central processing unit. 37, 46–49, 52, 155

**CU** controller unit. 44, 45

**DH** Denavit Hartenberg. 31

**DMA** direct memory access. 45, 47, 49, 155

**DOF** degree of freedom. 25, 31, 34, 67, 70, 75, 76, 82, 84, 90, 97, 114, 116, 117, 153, 155

**DTW** dynamic time warping. 6, 33, 35, 107–109, 111, 112, 117

**EKF** extended Kalman filter. 3, 9, 16, 17, 29, 30, 32, 65, 70, 91, 92, 94, 97, 104, 138, 149, 155

**EMG** electromyography. 40

**FFM** fat-free mass. 10

**FIM** Fisher information matrix. 28, 66

**GM** Gauss Markov. 30, 93

**GPIO** general purpose input output. 44

**GPS** global positioning system. 39

**HMM** hidden Markov model. 34

- I<sup>2</sup>C** inter-integrated circuit. 44, 46–49
- IMU** inertial measurement unit. 6, 9, 13–17, 19, 22, 24–26, 30, 32, 44, 45, 47–55, 57, 59–61, 64, 65, 67–71, 73, 75–81, 83–91, 94, 97–99, 102–104, 137–139, 152, 153, 155
- JNI** Java native interface. 48
- KiC** kinematic coupling. 32
- LHBF** long head of biceps femoris. 11
- LMA** Levenberg Marquart algorithm. 56, 57, 75
- MEMS** microelectromechanical systems. 14, 37, 46
- MLE** maximum likelihood estimator. 20, 26, 27
- PCA** principle component analysis. 34
- RM** repetition maximum. 10, 12, 14, 135
- RMSE** root mean squared error. 75–77, 80, 82–84, 152, 153
- RoM** range of motion. 10–12, 14, 104, 139
- SD** standard deviation. 61, 80, 86–88, 99, 155
- SDK** software development kit. 59, 89
- SfM** structure from motion. 38
- SVD** singular value decomposition. 56, 57
- SVM** support vector machine. 34
- UART** universal asynchronous receiver-transmitter. 45–48
- VSD-EKF** variable state dimension extended Kalman filter. 30
- ZVC** zero velocity crossing. 34, 116

## B. Mathematical Notations

Notation	Meaning
$\tilde{\omega}$	gyroscope vector measurement
$\tilde{a}$	accelerometer vector measurement
$\tilde{m}$	magnetometer vector measurement
$\vec{\omega}$	angular velocity vector
$\vec{a}$	acceleration vector
$\vec{m}$	magnetic field vector
$\vec{b}_\omega$	gyroscope measurement bias
$\vec{b}_a$	accelerometer measurement bias
$\vec{b}_m$	magnetometer measurement bias
$C_\omega$	gyro misalignment rotation matrix
$C_a$	accelerometer misalignment rotation matrix
$C_m$	magnetometer misalignment rotation matrix
$S_\omega$	gyro scale factor diagonal matrix
$S_a$	accelerometer scale factor diagonal matrix
$S_m$	magnetometer scale factor diagonal matrix
$m_{ref}$	reference magnetic field
$\vec{g}$	measured gravity vector
$G$	global frame
$R_{XY}$	rotation matrix from $Y$ to $X$
$q_{XY}$	quaternion of rotation from $Y$ to $X$
$\omega_{GS}$	angular velocity of sensor with respect to global frame
$\vec{l}_{mS}$	distance vector from IMU to joint $m$
$\vec{n}_P$	normal vector of plane $P$
$\vec{x}$	state vector
$\vec{\alpha}$	angular acceleration vector
$\vec{r}_{nS}$	rotation axis of a hinge joint, $n$ , measured in the frame of sensor $S$
$\vec{r}_{mS}$	rotation axis of a spheroidal joint, $m$ , measured in the frame of sensor $S$
$P(z x)$	probability density function of $z$ given $x$
$\Gamma$	acceleration from rotation
$N(\mu, \Sigma)$	multivariate normal distribution with the mean of $\mu$ and covariance $\Sigma$
$\exp$	exponential function



# C. Quaternion, Conversions and Filtering

## C.1. Quaternion

Quaternion is a hyper-complex number (C.1b), which is commonly used to present a 3D rotation in a four dimensional vector form((C.1c)).

$$q = q_w + q_x i + q_y j + q_z k \quad (\text{C.1a})$$

$$\vec{q} = [q_w \quad q_x \quad q_y \quad q_z]^T \quad (\text{C.1b})$$

$$(\text{C.1c})$$

This work follows Hamilton definition of quaternion and expresses a passive rotation, meaning that coordinate frames are transformed. In order to transform the presentation of a 3D vector  $v_A$  from frame A to the frame B, the quaternion  $q_{BA}$  which presents rotation from A to B can be applied according to Equation C.2.

$$\vec{v}_B = \vec{q}_{BA} \otimes \vec{v}_A \otimes \vec{q}_{BA}^* \quad (\text{C.2})$$

where  $\otimes$  is a quaternion multiplication which is a standard algebraic multiplication of form C.1b. The 3D vectors are in the form of quaternion,  $\vec{v} = [0 \quad v_x \quad v_y \quad v_z]^T$  and  $q_{BA}^*$  is conjugation of  $q_{BA}$ , which also defines inverse of the quaternion:

$$\vec{q}^* = [q_w \quad -q_x \quad -q_y \quad -q_z]^T \quad (\text{C.3})$$

The quaternion multiplication of  $q_1 \otimes q_2$  can also be written as matrix vector multiplication of  $[q_1]_L q_2$  or  $[q_2]_R q_1$ .

### C.1.1. Quaternion Derivative and Integration

When the quaternion is the transformation from global to local frame, the quaternion derivative is following:

$$\dot{\vec{q}} = \frac{1}{2} \vec{\omega} \otimes \vec{q} \quad (\text{C.4})$$

Here  $\vec{\omega}$  is the quaternion form of 3D angular velocity vector which is assumed to be of the global frame with respect to the local frame and measured in the local frame *i.e.*  ${}^S \vec{\omega}_{SG}$ .

Considering that the the derivative of angular velocity can be non zero, as it is the assumption

in Section 5.1.2, the quaternion integration is achieved using the first-order of Taylor expansion [131]:

$$q_k = q_{\Delta T} \otimes q_{k-1} \quad (\text{C.5a})$$

with

$$q_{\Delta T} = q_{\bar{\omega}} + \frac{\Delta T^2}{24} \omega_{k-1} \otimes \omega_k \quad (\text{C.5b})$$

$$q_{\bar{\omega}} = \exp(\bar{\omega} \Delta T) \quad (\text{C.5c})$$

, where  $\bar{\omega}$  is the median angular rate defined by:

$$\bar{\omega} = \omega_{k-1} + \frac{1}{2} \dot{\omega} \Delta T \quad (\text{C.6})$$

## C.2. Axis-Angle

Axis-angle represents the rotation of angle of the magnitude  $\theta$  around a unit vector  $\vec{u} = [u_x \ u_y \ u_z]$ , defining the axis of rotation. Which can be presented as a quaternion using exponential mapping:

$$q = \exp(\vec{u}\theta/2) = \cos(\theta/2) + \vec{u} \sin(\theta/2) \quad (\text{C.7})$$

## C.3. Conversions

### C.3.1. Quaternion to Rotation Matrix

$$R = \begin{bmatrix} q_w^2 + q_x^2 - q_y^2 - q_z^2 & 2(q_x q_y - q_w q_z) & 2(q_x q_z + q_w q_y) \\ 2(q_x q_y + q_w q_z) & q_w^2 - q_x^2 + q_y^2 - q_z^2 & 2(q_y q_z - q_w q_x) \\ 2(q_x q_z - q_w q_y) & 2(q_y q_z + q_w q_x) & q_w^2 - q_x^2 - q_y^2 + q_z^2 \end{bmatrix} \quad (\text{C.8})$$

### C.3.2. Axis Angle to Rotation Matrix

The equivalent rotation matrix of angle axis is the following:

$$R = \begin{bmatrix} v_x^2 C + c & v_x v_y C + z c & v_x v_z C + v_y s \\ v_y v_x C + v_z s & v_y^2 C + c & v_y v_z C - v_x s \\ v_x v_z C - v_y s & v_x v_y C + v_x s & v_z^2 C + c \end{bmatrix} \quad (\text{C.9})$$

, where  $c = \cos\theta$ ,  $s = \sin\theta$ ,  $C = 1 - c$

## C.4. Filtering

### C.4.1. Accelerometer/Magnetometer Model Jacobian

In both accelerometer and magnetometer measurement models in the orientation estimators described in Section 5.1, the measurement in the reference frame,  $\vec{v} \in \{\tilde{g}_G, \tilde{m}_{ref}\}$  is mapped to the measurement in the sensor frame using (C.8). Therefore the model should be linearised using (2.17e) which results the following jacobian:

$$H = \begin{bmatrix} H_{11} & H_{12} & H_{13} & H_{14} \\ H_{21} & H_{22} & H_{23} & H_{24} \\ H_{31} & H_{32} & H_{33} & H_{34} \end{bmatrix} \quad (\text{C.10})$$

where

$$\begin{aligned} H_{11} &= 2v_x q_w - 2v_y q_z + 2v_z q_y, & H_{24} &= H_{11}, & H_{33} &= -H_{11} \\ H_{12} &= -2v_x q_y + 2v_y q_x + 2v_z q_w, & H_{23} &= H_{12}, & H_{34} &= H_{12} \\ H_{13} &= -2v_x q_y + 2v_y q_x + 2v_z q_w, & H_{22} &= -H_{13}, & H_{31} &= H_{13} \\ H_{14} &= -2v_x q_z - 2v_y q_w + 2v_z q_x, & H_{21} &= -H_{14}, & H_{32} &= -H_{14} \end{aligned}$$

### C.4.2. Quaternion Jacobian

In both EKFs, presented in this thesis, the kinematic model includes the state transition, which is defined by (C.5). In order to calculate the transition matrix,  $F_k$  in (2.16), Equation (C.5) should be linearised with respect to the related states, here quaternion,  $q$ , angular velocity,  $\omega$ , and angular acceleration,  $\alpha$ :

$$\frac{\partial q_k}{\partial q_{k-1}} = [q_{\Delta T}]_L I_{4 \times 4} \quad (\text{C.11a})$$

$$\frac{\partial q_k}{\partial \omega_{k-1}} = [q_{k-1}]_R \left( \frac{\partial q_{\bar{\omega}}}{\partial \bar{\omega}} I_{3 \times 3} + \frac{\Delta T^2}{24} [\omega_k]_R I_{4 \times 3} \right) \quad (\text{C.11b})$$

$$\frac{\partial q_k}{\partial \alpha_{k-1}} = [q_{k-1}]_R \left( \frac{\Delta T}{2} \frac{\partial q_{\bar{\omega}}}{\partial \bar{\omega}} I_{3 \times 3} \right) \quad (\text{C.11c})$$

with  $I_{n \times n}$  being the identity matrix of order  $n$  and  $I_{4 \times 3} = \begin{bmatrix} 0_{1 \times 3} \\ I_{3 \times 3} \end{bmatrix}$

In order to compute  $\frac{\partial q_{\bar{\omega}}}{\partial \bar{\omega}}$  the Equation (C.7) is used:

$$\frac{\partial q_{\bar{\omega}}}{\partial \bar{\omega}} = \begin{bmatrix} -(\bar{\omega} \Delta T / |\bar{\omega}|) \sin(|\bar{\omega} \Delta T|) \\ \sin(\bar{\omega} \Delta T) (I_{3 \times 3} |\bar{\omega}|^2 - \bar{\omega} \bar{\omega}^T) / |\bar{\omega}|^3 + \cos(\bar{\omega} \Delta T) \bar{\omega} \bar{\omega}^T \Delta T / |\bar{\omega}|^2 \end{bmatrix} \quad (\text{C.12})$$





# List of Figures

2.1.	Joints and bone segments in lower body [10] . . . . .	13
2.2.	Natural misalignment of the knee joint axis with mechanical and anatomical axis of lower body [48] . . . . .	14
2.3.	Pelvis and thigh reverse movements with the same muscle group [88]: (a) Hip abductor muscles (b) Hip adductor muscles (c) Medial rotator muscles (d) Lateral rotator muscles (e) Hip flexor muscles (f) Hip extensor muscles . . . . .	15
2.4.	Body IMU calibration for upper body based on two static poses . . . . .	17
2.5.	Body IMU calibration based on two static poses . . . . .	17
2.6.	Similarity measures: (a) Euclidean distance (b) DTW distance . . . . .	25
3.1.	Commercial products integrating multiple sensing units: (a) Xsens suit (b) Entflux (c) Rokoko . . . . .	33
3.2.	Athos motion capture suit . . . . .	34
3.3.	hardware components: (1) 5 IMUs are mounted on pelvis (a, not visible), upper/lower right leg(b/c) and upper/lower left leg(d/e); (2) controller unit;(3) textile cables; (4) tablet to store and process data. . . . .	35
3.4.	(a) IMU (b) IMU connector . . . . .	36
3.5.	controller unit contains (1) the microcontroller evaluation board; (2) Bluetooth module; (3) battery; (4) charger . . . . .	37
3.6.	Data acquisition using the cascaded approach. . . . .	39
3.7.	The stick figure visualization of squat exercise on tablet. Each phase of squat is detected and user is guided to the next phase . . . . .	40
3.8.	Inertial sensor calibration: Calibration cube in different static poses on a leveled calibration table. . . . .	42
3.9.	Calibration results. . . . .	43
4.1.	Illustrates the development of the residuals in relation to the performed iterations when starting with the same initial guess. . . . .	48
4.2.	Magnetometer measurements before (red) and after (blue) calibration by the proposed method. In order to simplify comparison, the uncalibrated measurements are scaled to the mean value of the magnitudes. Ideally, the calibrated measurements should map to a unit sphere. . . . .	50
4.3.	A high precision aluminum cube on a turntable made of glass and aluminum with a flat wooden plate as a levelled base served as test setup for performing known motions. Here, the Xsens MTi is mounted inside the cube. . . . .	51
4.4.	Magnetometer measurements calibrated with our method (blue) and the method of Hu <i>et al.</i> (purple). The dataset was sampled in a location close to the equator. . . . .	52

4.5. Magnitudes of the magnetic field vectors measured under a wide range of rotations and calibrated with the three methods. . . . .	53
4.6. Heading errors resulting from the three calibration methods. . . . .	54
4.7. Projection of the calibrated magnetometer measurements on the different coordinate planes using the three calibration methods. . . . .	55
4.8. Illustration of the IMU position estimation problem. IMUs $A$ and $B$ are mounted on the adjacent segments of the joint $m$ . . . . .	57
4.9. Illustration of the IMU position estimation problem specifically addressing the lower body. The spheroidal joint $n$ refers to the hip (three rotation axes: $r_{mx}$ , $r_{my}$ , and $r_{mz}$ ), and the hinge joint $n$ refers to the knee (one rotation axis: $r_n$ ). The two joints are linked via the upper leg segment, with a fixed length of $l_{mn}$ . The IMUs $A, B, C$ are mounted on the segments connected through the hip and knee joints. They are placed on the pelvis, upper leg, and lower leg, respectively. The quantities $l_{mA}, l_{mB}, l_{nB}, l_{nC}$ are the IMU position vectors to be estimated. $R_{GA}, R_{GB}, R_{GC}$ are the orientations of the IMU with respect to the global coordinate frame $G$ . . . . .	61
4.10. Illustration of the constraints formulated in (4.26): The upper figure shows the idealized geometry, which is the basis for the constraints. It approximates the more realistic setup in the lower figure with skew joint axes, leading to the plane $\hat{P}1$ . The latter can be assumed to have a small angle $\alpha$ with respect to the ideal plane $P1$ . . . . .	64
4.11. The proposed autocalibration method. . . . .	66
4.12. RMSE for ten different IMU mounting orientations when applying the measurement model defined in (4.23) to type 2 movements. . . . .	68
4.13. RMSE for 100 different IMU to body configurations when using the measurement model defined in (4.23) and the additional constraint in (4.26). . . . .	69
4.14. Convergence test with 100 random initial values for the IMU position. In this test the true value of $l_{mA}$ is $[0.05, 0.09, 0.03]$ and the true value of $l_{mB}$ is $[-0.17, 0.004, 0.03]$ . . . . .	70
4.15. Test setup. The red arrows show three IMUs which are mounted on 1.pelvis (not visible), 2.upper leg and 3.lower leg . . . . .	71
4.16. Results on real measurements from random movements: RMSE of the Body-IMU calibration using Seel <i>et al.</i> and the proposed method, with respect to optical tracker. In the diagram test number of all the trials are ordered from 1 to 21 which means the first 3 are related to the trials performed by subject 1, the second 3 are related to subject 2, and so on . . . . .	75
4.17. Results on real measurements from the movements on each DOF separately: RMSE of the body-IMU calibration using Seel <i>et al.</i> and the proposed method, with respect to optical tracker. In the diagram test number of all the trials are ordered from 1 to 21 which means the first 3 are related to the trials performed by subject 1, the second 3 are related to subject 2, and so on. . . . .	76

4.18. Histogram of the accelerometer measurements which have the vector norm deviation higher than $2.5m/s^2$ in comparison to gravity vector. The average capture time duration was approximately 10 seconds which equals to 500 samples in each trial. . . . .	77
4.19. The percentage of measurements with observability criteria. The criteria were detected based on the measured angular velocity and threshold of 0.5 radian. . .	81
5.1. The global coordinate system with respect to reference vectors i.e. gravity, $\vec{g}_G$ , measured by accelerometer and earth magnetic field, $\vec{m}_G$ , measured by magnetometer. . . . .	84
5.2. The estimate versus numerically computed angular acceleration from a representative experiment where a subject performing the squat exercise. . . . .	87
5.3. The estimated versus measured magnetic field from result of the tests with 7 subjects performing the squat exercise. Note that the calibrated magnetometer measurements, according to the proposed method in Section 4.2 are supposed to be mapped to a unit sphere, therefore the deviation here has no unit. . . . .	87
5.4. The comparison of error from the common estimator with the extended estimator from result of the tests with 7 subjects performing the squat exercise. . . . .	88
5.5. The comparison of error of the extended estimator with optical tracker in a representative experiment where a subject performing the squat exercise. . . . .	88
5.6. Illustration of the leg segment positions, ${}^A\vec{p}_B$ , ${}^A\vec{p}_C$ , as are defined by the position of IMUs mounted on the upper segment, IMU $B$ , and lower segment, IMU $C$ with respect to the coordinate frame of IMU $A$ mounted on the pelvis. The spheroidal joint $m$ refers to the hip, and the hinge joint $n$ refers to the knee (one rotation axis: $r_n$ ). The two joints are linked via the upper leg segment. The quantities $l_{mA}$ , $l_{mB}$ , $l_{nB}$ , $l_{nC}$ are the IMU position vectors with respect to joints which are estimated based on the proposed method in Section 4.3.4 . . . . .	90
5.7. Setup for joint angle estimation evaluation. In order to simplify two single markers, shown with arrows, are placed on each segment. . . . .	92
5.8. Comparison of the knee joint angle as estimated using the proposed pose estimation method with the optical tracker result. . . . .	93
5.9. Comparison of the hip joint angle as estimated using the proposed pose estimation method with the optical tracker result. . . . .	93
5.10. Comparison of segment position error when using body-IMU calibration methods in [124] (red) and the proposed method in Section 4.3.4 (green) . . . . .	95
5.11. The estimated positions of IMUs mounted on upper and lower leg, $P_B$ , $P_C$ , using IMU measurements and proposed method versus optical tracker from a representative experiment . . . . .	95
5.12. the overall computational graph of the system . . . . .	97

- 
- 6.1. Feature extraction of query signal using the proposed method. The query contains 4DOF joint angles captured during a squat exercise. Each DOF is defined by three different features: velocity, mean, and variance. These are correlated with each detected motion primitive. The detection motion primitives are presented by the black circle markers on the knee joint angle, as it has the highest variance and serves as a dominant DOF. . . . . 107
  - 6.2. An example of streaming signal captured during performing squats and other types of movements. . . . . 111
  - 6.3. The STWM matrix in SPRING for an experiment with 4DOF joint angles: The values of this matrix, dtw distances, are normalized by the maximum value and presented by a built-in Colormap in Matlab, where darker colours depict the lower values. Therefore, the warping path of a matched subsequence can be identified, where there is a continuous darker area from the first to the last row. For brevity, this matrix is scaled down 10 and 5 times along the row and column. The streaming signal and the query are represented at the top and left side. Note that each joint angle vector is normalized. . . . . 114
  - 6.4. ISPRING normalization . . . . . 116
  - 6.5. NSPRING normalization . . . . . 118
  - 6.6. DNRTPM normalization . . . . . 120
  - 6.7. Feature extraction from the hip and knee joint angles using the proposed method. The features extracted from the joint angles in motion primitives of the streaming signal presented at left and query at right. . . . . 122
  - 6.8. Feature extraction from the leg positions using the proposed method. The features extracted from the leg segment positions in motion primitives of the streaming signal presented at left and query at right. . . . . 122
  - 6.9. The STWM matrix in the proposed method for an experiment with 4DOF joint angles: The values of this matrix, dtw distances, are normalized by the maximum value and presented by a built-in Colormap in Matlab, where darker colours depict the lower values. Therefore, the warping path of a matched subsequence can be identified, where there is a continuous darker area from the first to the last row. The number of rows and columns presented here correspond with the actual matrix, as a result of dimension reduction offered by the motion primitive technique in the proposed. The extracted features of streaming signal and the query are represented at the top and left side. . . . . 123

# List of Tables

3.1.	Effect of using DMA and cascaded approach on the CPU processing time . . .	40
3.2.	Comparison of the CPU current drain . . . . .	41
3.3.	Weight comparison . . . . .	42
3.4.	Measurement quality evaluation in terms of noise levels (standard deviation under static conditions). . . . .	43
4.1.	The angular velocity variations for the simulated IMU measurements: 12 represents the variation between the first and the second DOF for each IMU A, B, C. Each number expresses the mean of squared differences between the simulated angular velocities for all the timesteps. . . . .	67
4.2.	The angular velocity variations for the movements in the first calibration trial. See Table 4.1 for more details. . . . .	73
4.3.	The angular velocity variations for the movements in the second calibration trial. See Table 4.1 for more details. . . . .	73
4.4.	The angular velocity variations for the movements in the third calibration trial. See Table 4.1 for more details. . . . .	73
4.5.	The error(mean $\pm$ SD) in position of each joint $m, n$ with respect to each IMU A, B, C estimated by Seel <i>et al.</i> method using type A movements . . . . .	78
4.6.	The error (mean $\pm$ SD) in position of each joint $m, n$ with respect to each IMU A, B, C estimated by the proposed method using type A movements . . . . .	78
4.7.	The error (mean $\pm$ SD) in position of each joint $m, n$ with respect to each IMU A, B, C estimated by Seel <i>et al.</i> method using type B movements . . . . .	79
4.8.	The error (mean $\pm$ SD) in position of each joint $m, n$ with respect to each IMU A, B, C estimated by proposed method using type B movements . . . . .	79
5.1.	Values of the parameters which are used in the EKFs for orientation estimation	86
5.2.	Values of the parameters which are used in the EKF for pose estimation . . . . .	91
5.3.	Error of estimated upper and lower segments positions using the proposed method for squat exercise. . . . .	94
5.4.	Error of estimated upper and lower segments positions using the proposed method for abduction and adduction exercise . . . . .	94
6.1.	Squat identification with knee joint angle based on SPRING method. . . . .	112
6.2.	Squat identification with knee and hip joint angles based on SPRING method. . . . .	113
6.3.	Squat identification with leg positions based on SPRING method. . . . .	113

6.4. Squat identification with knee joint angle based on ISPRING method. Note that for a better comparison of the metrics with the other methods, the overlapping matches in one area, for both false positives and true positives, were counted as one. . . . .	115
6.5. Squat identification with knee joint angle based on NSPRING method. . . . .	117
6.6. Squat identification with knee and hip joint angles based on NSPRING method.	117
6.7. Squat identification with knee joint angle based on DNRTPM method. . . . .	119
6.8. Squat identification with knee and hip joint angles based on DNRTPM method.	119
6.9. Squat identification with leg positions based on DNRTPM method. . . . .	121
6.10. Squat identification with knee joint angle based on the proposed method. . . . .	124
6.11. Squat identification with knee and hip joint angles based on the proposed method.	124
6.12. Squat identification with leg positions based on the proposed method. . . . .	124
6.13. Squat identification with the knee joint angle. . . . .	125
6.14. Squat identification with hip and knee joint angles. . . . .	125
6.15. Squat identification with leg positions. . . . .	125

# Bibliography

- [1] AAGAARD, P., ANDERSEN, J., BENNEKOU, M., LARSSON, B., OLESEN, J., CRAMERI, R., MAGNUSSON, S. P., AND KJAER, M. Effects of resistance training on endurance capacity and muscle fiber composition in young top-level cyclists. *Scandinavian journal of medicine & science in sports* 21, 6 (2011), e298–e307. 2
- [2] ALONSO, R., AND SHUSTER, M. D. Complete linear attitude-independent magnetometer calibration. *Journal of the Astronautical Sciences* 50, 4 (2002), 477–490. 12
- [3] ALOUI, S., VILLIEN, C., AND LESECQ, S. A new approach for motion capture using magnetic field: models, algorithms and first results. *International Journal of Adaptive Control and Signal Processing* 29, 4 (2015), 407–426. 31
- [4] ANIMAZOO IGS 180. <http://www.synertial.com/products/igs-180/>. [Online; accessed 25-January-2020]. 5, 42
- [5] ATARIFIT. <http://www.atarifit.com/>. [Online; accessed 25-January-2020]. 5
- [6] ATHOS TRAINING SYSTEM. <http://www.liveathos.com/>. [Online; accessed 25-January-2020]. 32, 34
- [7] BACHMANN, E. R., YUN, X., AND PETERSON, C. W. An investigation of the effects of magnetic variations on inertial/magnetic orientation sensors. In *Robotics and Automation, 2004. Proceedings. ICRA'04. 2004 IEEE International Conference on* (2004), vol. 2, IEEE, pp. 1115–1122. 11, 22
- [8] BAR-JOSEPH, Z., GERBER, G., GIFFORD, D. K., JAAKKOLA, T. S., AND SIMON, I. A new approach to analyzing gene expression time series data. In *Proceedings of the sixth annual international conference on Computational biology* (2002), pp. 39–48. 25
- [9] BASHIR, F., QU, W., KHOKHAR, A., AND SCHONFELD, D. Hmm-based motion recognition system using segmented pca. In *IEEE International Conference on Image Processing 2005* (2005), vol. 3, IEEE, pp. III–1288. 26
- [10] BASICMEDICAL KEY. <https://basicmedicalkey.com/lower-limb-2/>. [Online; accessed 25-January-2020]. 13, 141
- [11] BERNDT, D. J., AND CLIFFORD, J. Using dynamic time warping to find patterns in time series. In *KDD workshop* (1994), vol. 10, Seattle, WA, pp. 359–370. 25

- [12] BLESER, G., HENDEBY, G., AND MIEZAL, M. Using egocentric vision to achieve robust inertial body tracking under magnetic disturbances. In *2011 10th IEEE International Symposium on Mixed and Augmented Reality* (2011), IEEE, pp. 103–109. <sup>16</sup>
- [13] BLESER, G., STEFFEN, D., REISS, A., WEBER, M., HENDEBY, G., AND FRADET, L. Personalized physical activity monitoring using wearable sensors. In *Smart health*. Springer, 2015, pp. 99–124. <sup>1</sup>
- [14] BMA 456 . <https://www.bosch-sensortec.com/products/motion-sensors/accelerometers/bma456.html>. [Online; accessed 25-January-2020]. <sup>38</sup>
- [15] BORSHUKOV, G., PIPONI, D., LARSEN, O., LEWIS, J. P., AND TEMPELAAR-LIETZ, C. Universal capture-image-based facial animation for the matrix reloaded. In *ACM Siggraph 2005 Courses* (2005), ACM, p. 16. <sup>30</sup>
- [16] BOWDITCH, N., BOWDITCH, J. I., AND OFFICE, U. S. H. *The New American Practical Navigator..* New York: EM Blunt,[1802-18–], 1811. <sup>12</sup>
- [17] BRUIJN, S. M., MEIJER, O. G., VAN DIEEN, J. H., KINGMA, I., AND LAMOTH, C. J. Coordination of leg swing, thorax rotations, and pelvis rotations during gait: the organisation of total body angular momentum. *Gait & posture* 27, 3 (2008), 455–462. <sup>59</sup>
- [18] BUTTE, N. F., EKELUND, U., AND WESTERTERP, K. R. Assessing physical activity using wearable monitors: measures of physical activity. *Med Sci Sports Exerc* 44, 1 Suppl 1 (2012), S5–12. <sup>2</sup>
- [19] CASEY, R. T., KARPENKO, M., CURRY, R., AND ELKAIM, G. Attitude representation and kinematic propagation for low-cost uavs. In *AIAA Guidance, Navigation, and Control (GNC) Conference* (2013), p. 4615. <sup>22</sup>
- [20] CASIO, TECHNOLOGY: TIDE GRAPH DISPLAY . <https://www.casio-europe.com/euro/products/watches/technology/tide-graph-display/>. [Online; accessed 25-January-2020]. <sup>31</sup>
- [21] CHAN, M., ESTÈVE, D., FOURNIOLS, J.-Y., ESCRIBA, C., AND CAMPO, E. Smart wearable systems: Current status and future challenges. *Artificial intelligence in medicine* 56, 3 (2012), 137–156. <sup>1</sup>
- [22] CHENG, J., AMFT, O., BAHLE, G., AND LUKOWICZ, P. Designing sensitive wearable capacitive sensors for activity recognition. *IEEE Sensors Journal* 13, 10 (2013), 3935–3947. <sup>16, 32</sup>
- [23] CHENG, P., AND OELMANN, B. Joint-angle measurement using accelerometers and gyroscopes: A survey. *IEEE Transactions on instrumentation and measurement* 59, 2 (2010), 404–414. <sup>23</sup>



- [24] CHERIAN, J. J., KAPADIA, B. H., BANERJEE, S., JAUREGUI, J. J., ISSA, K., AND MONT, M. A. Mechanical, anatomical, and kinematic axis in tka: concepts and practical applications. *Current reviews in musculoskeletal medicine* 7, 2 (2014), 89–95. 14
- [25] CORAZZA, S., MUENDERMANN, L., CHAUDHARI, A., DEMATTIO, T., COBELLI, C., AND ANDRIACCHI, T. P. A markerless motion capture system to study musculoskeletal biomechanics: visual hull and simulated annealing approach. *Annals of biomedical engineering* 34, 6 (2006), 1019–1029. 30
- [26] COSKUN, H., ACHILLES, F., DIPIETRO, R., NAVAB, N., AND TOMBARI, F. Long short-term memory kalman filters: Recurrent neural estimators for pose regularization. In *Proceedings of the IEEE International Conference on Computer Vision* (2017), pp. 5524–5532. 131
- [27] DEJNABADI, H., JOLLES, B. M., AND AMINIAN, K. A new approach to accurate measurement of uniaxial joint angles based on a combination of accelerometers and gyroscopes. *IEEE Transactions on Biomedical Engineering* 52, 8 (2005), 1478–1484. 23
- [28] DEJNABADI, H., JOLLES, B. M., CASANOVA, E., FUA, P., AND AMINIAN, K. Estimation and visualization of sagittal kinematics of lower limbs orientation using body-fixed sensors. *IEEE Transactions on Biomedical Engineering* 53, 7 (2006), 1385–1393. 23
- [29] DEUTSCHER, J., BLAKE, A., AND REID, I. Articulated body motion capture by annealed particle filtering. In *Computer Vision and Pattern Recognition, 2000. Proceedings. IEEE Conference on* (2000), vol. 2, IEEE, pp. 126–133. 30
- [30] DING, H., TRAJCEVSKI, G., SCHEUERMANN, P., WANG, X., AND KEOGH, E. Querying and mining of time series data: experimental comparison of representations and distance measures. *Proceedings of the VLDB Endowment* 1, 2 (2008), 1542–1552. 25
- [31] DUNNE, L., PROFITA, H., AND ZEAGLER, C. Social aspects of wearability and interaction. In *Wearable Sensors*. Elsevier, 2014, pp. 25–43. 5
- [32] EA SPORTS. <http://www.ea.com/>. [Online; accessed 25-January-2020]. 30
- [33] ENFLUX SMART CLOTHING. 32, 34
- [34] FAVRE, J., AISSAOUI, R., JOLLES, B. M., DE GUISE, J. A., AND AMINIAN, K. Functional calibration procedure for 3d knee joint angle description using inertial sensors. *Journal of biomechanics* 42, 14 (2009), 2330–2335. 18
- [35] FERRARIS, F., GRIMALDI, U., AND PARVIS, M. Procedure for effortless in-field calibration of three-axis rate gyros and accelerometers. *Sensors and Materials* 7 (1995), 311–311. 11, 45
- [36] FITNESS RPG - FITNESS GAME, WALKING GAME . <https://play.google.com/store/apps/details?id=com.shikudo.fitrpg.google&hl=en>. [Online; accessed 25-January-2020]. 5

- [37] FOD, A., MATARIĆ, M. J., AND JENKINS, O. C. Automated derivation of primitives for movement classification. *Autonomous robots* 12, 1 (2002), 39–54. 26
- [38] GANDER, W., GOLUB, G. H., AND STREBEL, R. Least-squares fitting of circles and ellipses. *BIT Numerical Mathematics* 34, 4 (1994), 558–578. 47
- [39] GARMIN, FORERUNNER® 101. <https://buy.garmin.com/en-US/US/p/231>. [Online; accessed 25-January-2020]. 31
- [40] GAVRILA, D. M., AND DAVIS, L. S. 3-d model-based tracking of humans in action: a multi-view approach. In *Computer Vision and Pattern Recognition, 1996. Proceedings CVPR'96, 1996 IEEE Computer Society Conference on* (1996), IEEE, pp. 73–80. 30
- [41] GIAO, B. C., AND ANH, D. T. Similarity search in multiple high speed time series streams under dynamic time warping. In *2015 2nd National Foundation for Science and Technology Development Conference on Information and Computer Science (NICS)* (2015), IEEE, pp. 82–87. 27
- [42] GIAO, B. C., AND ANH, D. T. Improving spring method in similarity search over time-series streams by data normalization. In *International Conference on Nature of Computation and Communication* (2016), Springer, pp. 189–202. 100, 103, 115, 126
- [43] GONG, X., FONG, S., CHAN, J. H., AND MOHAMMED, S. Nspring: the spring extension for subsequence matching of time series supporting normalization. *The Journal of Supercomputing* 72, 10 (2016), 3801–3825. 100, 102, 117, 126
- [44] GRAVES, J. E., POLLOCK, M. L., CARPENTER, D. M., LEGGETT, S. H., JONES, A., MACMILLAN, M., AND FULTON, M. Quantitative assessment of full range-of-motion isometric lumbar extension strength. *Spine* 15, 4 (1990), 289–294. 1
- [45] HÄGGLUND, M., WALDÉN, M., AND EKSTRAND, J. Risk factors for lower extremity muscle injury in professional soccer the uefa injury study. *The American journal of sports medicine* 41, 2 (2013), 327–335. 3
- [46] HARADA, T., MORI, T., AND SATO, T. Development of a tiny orientation estimation device to operate under motion and magnetic disturbance. *The International Journal of Robotics Research* 26, 6 (2007), 547–559. 83
- [47] HEWETT, T. E., DI STASI, S. L., AND MYER, G. D. Current concepts for injury prevention in athletes after anterior cruciate ligament reconstruction. *The American journal of sports medicine* 41, 1 (2013), 216–224. 3
- [48] HIP AND KNEE BOOK. <https://hipandkneebook.com/tja-publication-blog/2017/3/1/knee-basics-native-alignment>. [Online; accessed 25-January-2020]. 14, 141
- [49] HORN, B. K., AND SCHUNCK, B. G. Determining optical flow. In *1981 Technical symposium east* (1981), International Society for Optics and Photonics, pp. 319–331. 30

- [50] HU, X., LIU, Y., WANG, Y., HU, Y., AND YAN, D. Autocalibration of an electronic compass for augmented reality. In *Proceedings of the 4th IEEE/ACM International Symposium on Mixed and Augmented Reality* (2005), IEEE Computer Society, pp. 182–183. 12, 46, 49
- [51] HUNTER, G. R., WETZSTEIN, C. J., FIELDS, D. A., BROWN, A., AND BAMMAN, M. M. Resistance training increases total energy expenditure and free-living physical activity in older adults. *Journal of Applied Physiology* 89, 3 (2000), 977–984. 2
- [52] JANUS, B., AND NAKAMURA, Y. Unsupervised probabilistic segmentation of motion data for mimesis modeling. In *ICAR'05. Proceedings., 12th International Conference on Advanced Robotics, 2005.* (2005), IEEE, pp. 411–417. 26
- [53] JULIER, S. J., AND UHLMANN, J. K. Unscented filtering and nonlinear estimation. *Proceedings of the IEEE* 92, 3 (2004), 401–422. 21
- [54] KALMAN, R. E., AND BUCY, R. S. New Results in Linear Filtering and Prediction Theory. *Journal of Basic Engineering* 83, 1 (03 1961), 95–108. 20
- [55] KAUFMAN, K. R., BRODINE, S. K., SHAFFER, R. A., JOHNSON, C. W., AND CULLISON, T. R. The effect of foot structure and range of motion on musculoskeletal overuse injuries. *The American Journal of Sports Medicine* 27, 5 (1999), 585–593. 3
- [56] KEOGH, E., CHAKRABARTI, K., PAZZANI, M., AND MEHROTRA, S. Dimensionality reduction for fast similarity search in large time series databases. *Knowledge and information Systems* 3, 3 (2001), 263–286. 100
- [57] KEOGH, E., CHAKRABARTI, K., PAZZANI, M., AND MEHROTRA, S. Locally adaptive dimensionality reduction for indexing large time series databases. In *Proceedings of the 2001 ACM SIGMOD international conference on Management of data* (2001), pp. 151–162. 25
- [58] KEOGH, E., AND RATANAMAHATANA, C. A. Exact indexing of dynamic time warping. *Knowledge and information systems* 7, 3 (2005), 358–386. 100
- [59] KEOGH, E., WEI, L., XI, X., VLACHOS, M., LEE, S.-H., AND PROTOPAPAS, P. Supporting exact indexing of arbitrarily rotated shapes and periodic time series under euclidean and warping distance measures. *The VLDB journal* 18, 3 (2009), 611–630. 100
- [60] KETTUNEN, J. A., KUJALA, U. M., RÄTY, H., VIDEMAN, T., SARNA, S., IMPIVAARA, O., AND KOSKINEN, S. Factors associated with hip joint rotation in former elite athletes. *British journal of sports medicine* 34, 1 (2000), 44–48. 2
- [61] KHAYAMBASHI, K., GHODDOSI, N., STRAUB, R. K., AND POWERS, C. M. Hip muscle strength predicts noncontact anterior cruciate ligament injury in male and female athletes a prospective study. *The American journal of sports medicine* (2015), 0363546515616237. 3

- [62] KIM, A., AND GOLNARAGHI, M. A quaternion-based orientation estimation algorithm using an inertial measurement unit. In *PLANS 2004. Position Location and Navigation Symposium (IEEE Cat. No. 04CH37556)* (2004), IEEE, pp. 268–272. <sup>22</sup>
- [63] KO, M. H., WEST, G., VENKATESH, S., AND KUMAR, M. Using dynamic time warping for online temporal fusion in multisensor systems. *Information Fusion* 9, 3 (2008), 370–388. <sup>27</sup>
- [64] KOK, M., HOL, J. D., AND SCHÖN, T. B. An optimization-based approach to human body motion capture using inertial sensors. *IFAC Proceedings Volumes* 47, 3 (2014), 79–85. <sup>23</sup>
- [65] KOKMEYER, D., WAHOFF, M., AND MYMERN, M. Suggestions from the field for return-to-sport rehabilitation following anterior cruciate ligament reconstruction: alpine skiing. *journal of orthopaedic & sports physical therapy* 42, 4 (2012), 313–325. <sup>3, 16</sup>
- [66] KULIG, K., ANDREWS, J. G., AND HAY, J. G. Human strength curves. *Exercise and sport sciences reviews* 12, 1 (1984), 417–466. <sup>1</sup>
- [67] LIN, J. F., AND KULIĆ, D. Human pose recovery using wireless inertial measurement units. *Physiological measurement* 33, 12 (2012), 2099. <sup>23</sup>
- [68] LIN, J. F.-S., AND KULIĆ, D. Online segmentation of human motion for automated rehabilitation exercise analysis. *IEEE Transactions on Neural Systems and Rehabilitation Engineering* 22, 1 (2013), 168–180. <sup>26</sup>
- [69] LUCAS FILM. <http://lucasfilm.com/>. [Online; accessed 25-January-2020]. <sup>30</sup>
- [70] LUINGE, H. J., ROETENBERG, D., AND SLYCKE, P. J. Inertial sensor kinematic coupling, Feb. 3 2011. US Patent App. 12/534,526. <sup>23, 24</sup>
- [71] LUINGE, H. J., AND VELTINK, P. H. Measuring orientation of human body segments using miniature gyroscopes and accelerometers. *Medical and Biological Engineering and computing* 43, 2 (2005), 273–282. <sup>16, 22</sup>
- [72] LUO, Y., YE, G., WU, Y., GUO, J., LIANG, J., AND YANG, Y. An adaptive kalman filter for uav attitude estimation. In *2019 IEEE 2nd International Conference on Electronics Technology (ICET)* (2019), IEEE, pp. 258–262. <sup>131</sup>
- [73] MAKNI, A., FOURATI, H., AND KIBANGOU, A. Y. Adaptive kalman filter for mems-imu based attitude estimation under external acceleration and parsimonious use of gyroscopes. In *2014 European Control Conference (ECC)* (2014), IEEE, pp. 1379–1384. <sup>131</sup>
- [74] MARINS, J. L., YUN, X., BACHMANN, E. R., MCGHEE, R. B., AND ZYDA, M. J. An extended kalman filter for quaternion-based orientation estimation using marg sensors. In *Proceedings 2001 IEEE/RSJ International Conference on Intelligent Robots and*

- Systems. Expanding the Societal Role of Robotics in the the Next Millennium (Cat. No. 01CH37180)* (2001), vol. 4, IEEE, pp. 2003–2011. <sup>22, 83</sup>
- [75] MARKETWATCH. <https://www.marketwatch.com/>. [Online; accessed 25-January-2020]. <sup>31</sup>
- [76] MAZZETTI, S. A., KRAEMER, W. J., VOLEK, J. S., DUNCAN, N. D., RATAMESS, N. A., GOMEZ, A., NEWTON, R. U., HAKKINEN, K., AND FLECK, S. J. The influence of direct supervision of resistance training on strength performance. *Medicine and Science in Sports and Exercise* 32, 6 (2000), 1175–1184. <sup>2</sup>
- [77] MCGRATH, M. J., AND SCANAILL, C. N. *Sensor Technologies: Healthcare, Wellness and Environmental Applications*. Apress, 2013. <sup>4</sup>
- [78] MENGUC, Y., PARK, Y.-L., MARTINEZ-VILLALPANDO, E., AUBIN, P., ZISOOK, M., STIRLING, L., WOOD, R. J., AND WALSH, C. J. Soft wearable motion sensing suit for lower limb biomechanics measurements. In *IEEE International Conference on Robotics and Automation (ICRA)* (2013), pp. 5309–5316. <sup>32</sup>
- [79] MICROSTRAIN. <http://www.microstrain.com/inertial>. [Online; accessed 25-January-2020]. <sup>30</sup>
- [80] MIEZAL, M., BLESER, G., SCHMITZ, N., AND STRICKER, D. A generic approach to inertial tracking of arbitrary kinematic chains. In *8th International Conference on Body Area Networks* (2013), pp. 189–192. <sup>16</sup>
- [81] MILNE, W. E. *Numerical Solution of Differential Equations*. Applied mathematics series *JohnWiley&Sons*. New York, Wiley, 1953. <sup>56, 106</sup>
- [82] MONTGOMERY, K., MUNDT, C., THONIER, G., TELLIER, A., UDOH, U., BARKER, V., RICKS, R., GIOVANGRANDI, L., DAVIES, P., CAGLE, Y., ET AL. Lifeguard—a personal physiological monitor for extreme environments. In *26th Annual International Conference of the IEEE Engineering in Medicine and Biology Society* (2004), vol. 1, pp. 2192–2195. <sup>32</sup>
- [83] MORÉ, J. J. The levenberg-marquardt algorithm: implementation and theory. In *Numerical analysis*. Springer, 1978, pp. 105–116. <sup>48</sup>
- [84] MORRIS, D., SAPONAS, T. S., GUILLORY, A., AND KELNER, I. Recofit: using a wearable sensor to find, recognize, and count repetitive exercises. In *Proceedings of the SIGCHI Conference on Human Factors in Computing Systems* (2014), ACM, pp. 3225–3234. <sup>26</sup>
- [85] MOTIONSTAR. <http://www.mindflux.com.au/products/ascension/motionstar.html>. [Online; accessed 25-January-2020]. <sup>31</sup>

- [86] MPU9250 . <https://invensense.tdk.com/products/motion-tracking/9-axis/mpu-9250/>. [Online; accessed 25-January-2020]. 38
- [87] MÜNDERMANN, L., CORAZZA, S., AND ANDRIACCHI, T. P. The evolution of methods for the capture of human movement leading to markerless motion capture for biomechanical applications. *Journal of NeuroEngineering and Rehabilitation* 3, 1 (2006), 1. 30
- [88] MUSCOLINO, J. *Manual Therapy for the Low Back and Pelvis: A Clinical Orthopedic Approach*. LWW in touch series. Wolters Kluwer Health, 2014. 15, 141
- [89] NATIONAL CENTERS FOR ENVIRONMENTAL INFORMATION. <http://www.ngdc.noaa.gov/ngdc.html>. [Online; accessed 25-January-2020]. 48
- [90] NERINO, R., CONTIN, L., DA SILVA PINTO, W., MASSAZZA, G., ACTIS, M., CAPACCHIONE, P., CHIMIENTI, A., AND PETTITI, G. A bsn based service for post-surgical knee rehabilitation at home. In *Proceedings of the 8th International Conference on Body Area Networks* (2013), ICST (Institute for Computer Sciences, Social-Informatics and Telecommunications), pp. 401–407. 1, 18
- [91] NICORA, D. A. Microsoft kinect, Sept. 13 2016. US Patent 9,440,134. 30
- [92] O'BRIEN, J. F., BODENHEIMER JR, R. E., BROSTOW, G. J., AND HODGINS, J. K. Automatic joint parameter estimation from magnetic motion capture data. 31
- [93] O'DONOVAN, K. J., KAMNIK, R., O'KEEFFE, D. T., AND LYONS, G. M. An inertial and magnetic sensor based technique for joint angle measurement. *Journal of biomechanics* 40, 12 (2007), 2604–2611. 16, 18
- [94] OERTEL-KNÖCHEL, V., MEHLER, P., THIEL, C., STEINBRECHER, K., MALCHOW, B., TESKY, V., ADEMMER, K., PRVULOVIC, D., BANZER, W., ZOPF, Y., ET AL. Effects of aerobic exercise on cognitive performance and individual psychopathology in depressive and schizophrenia patients. *European archives of psychiatry and clinical neuroscience* 264, 7 (2014), 589–604. 2
- [95] OPTITRACK FLEX 13 . <https://www.naturalpoint.com/optitrack/products/flex-13>. [Online; accessed 25-January-2020]. 68, 91
- [96] PALERMO, E., ROSSI, S., MARINI, F., PATANÈ, F., AND CAPPÀ, P. Experimental evaluation of accuracy and repeatability of a novel body-to-sensor calibration procedure for inertial sensor-based gait analysis. *Measurement* 52 (2014), 145–155. 16
- [97] PLASQUI, G., AND WESTERTERP, K. R. Physical activity assessment with accelerometers: an evaluation against doubly labeled water. *Obesity* 15, 10 (2007), 2371–2379. 2

- [98] POLAR H10 HEART RATE MONITOR. [http://www.polar.com/ca-en/products/accessories/H7\\_heart\\_rate\\_sensor](http://www.polar.com/ca-en/products/accessories/H7_heart_rate_sensor). [Online; accessed 25-January-2020]. <sup>31</sup>
- [99] POLHEMUS. <http://polhemus.com/motion-tracking/all-trackers/liberty>. [Online; accessed 25-January-2020]. <sup>31</sup>
- [100] POWERS, C. M. The influence of abnormal hip mechanics on knee injury: a biomechanical perspective. *journal of orthopaedic & sports physical therapy* 40, 2 (2010), 42–51. <sup>4</sup>
- [101] QUALISYS, APPLICATION OF HUMAN BIOMECHANICS . <https://www.qualisys.com/applications/human-biomechanics/>. [Online; accessed 25-January-2020]. <sup>30</sup>
- [102] RAKTHANMANON, T., CAMPANA, B., MUEEN, A., BATISTA, G., WESTOVER, B., ZHU, Q., ZAKARIA, J., AND KEOGH, E. Searching and mining trillions of time series subsequences under dynamic time warping. In *Proceedings of the 18th ACM SIGKDD international conference on Knowledge discovery and data mining* (2012), pp. 262–270. <sup>27, 100, 102, 104</sup>
- [103] RATANAMAHATANA, C. A., AND KEOGH, E. Making time-series classification more accurate using learned constraints. In *Proceedings of the 2004 SIAM international conference on data mining* (2004), SIAM, pp. 11–22. <sup>27</sup>
- [104] RAVICHANDRAN, R., KUMAR, A., AND KUMAR, R. Joint angle measurement using mems based inertial sensors for biped robot. In *2018 Second International Conference on Electronics, Communication and Aerospace Technology (ICECA)* (March 2018), pp. 225–231. <sup>37</sup>
- [105] REISS, A., HENDEBY, G., BLESER, G., AND STRICKER, D. Activity recognition using biomechanical model based pose estimation. In *5th European Conference on Smart Sensing and Context (EuroSSC)* (2010), pp. 42–55. <sup>14, 23</sup>
- [106] RENAUDIN, V., AFZAL, M. H., AND LACHAPELLE, G. New method for magnetometers based orientation estimation. In *Position Location and Navigation Symposium (PLANS), 2010 IEEE/ION* (2010), IEEE, pp. 348–356. <sup>12, 46, 48</sup>
- [107] ROCOCO SMARTSUIT PRO. <https://www.rokoko.com>. [Online; accessed 25-January-2020]. <sup>32</sup>
- [108] ROETENBERG, D., LUINGE, H., AND SLYCKE, P. Xsens mvn: Full 6dof human motion tracking using miniature inertial sensors. *Xsens Motion Technologies BV, Tech. Rep 1* (2009). <sup>30</sup>
- [109] ROETENBERG, D., LUINGE, H. J., BATEN, C. T., AND VELTINK, P. H. Compensation of magnetic disturbances improves inertial and magnetic sensing of human body segment

- orientation. *IEEE Transactions on neural systems and rehabilitation engineering* 13, 3 (2005), 395–405. <sup>11, 22</sup>
- [110] RØNNESTAD, B. R., HANSEN, J., HOLLAN, I., AND ELLEFSEN, S. Strength training improves performance and pedaling characteristics in elite cyclists. *Scandinavian journal of medicine & science in sports* 25, 1 (2015), e89–e98. <sup>2</sup>
- [111] RØNNESTAD, B. R., AND MUJKA, I. Optimizing strength training for running and cycling endurance performance: A review. *Scandinavian journal of medicine & science in sports* 24, 4 (2014), 603–612. <sup>2</sup>
- [112] ROSS, P. E. Top 11 technologies of the decade. *IEEE Spectrum* 1, 48 (2011), 27–63. <sup>4</sup>
- [113] RUNKEEPER. <https://runkeeper.com/>. [Online; accessed 25-January-2020]. <sup>5</sup>
- [114] SABATINI, A. M. Quaternion-based extended kalman filter for determining orientation by inertial and magnetic sensing. *Biomedical Engineering, IEEE Transactions on* 53, 7 (2006), 1346–1356. <sup>11, 22</sup>
- [115] SABATINI, A. M. Variable-state-dimension kalman-based filter for orientation determination using inertial and magnetic sensors. *Sensors* 12, 7 (2012), 8491–8506. <sup>22</sup>
- [116] SAKURAI, Y., FALOUTSOS, C., AND YAMAMURO, M. Stream monitoring under the time warping distance. In *2007 IEEE 23rd International Conference on Data Engineering* (April 2007), pp. 1046–1055. <sup>27, 100, 104, 112, 126</sup>
- [117] SALEHI, S., BLESER, G., SCHMITZ, N., AND STRICKER, D. A low-cost and lightweight motion tracking suit. In *10th International Conference on Ubiquitous Intelligence and Computing (UIC)* (2013), pp. 474–479. <sup>6</sup>
- [118] SALEHI, S., BLESER, G., AND STRICKER, D. Design and development of low-cost smart training pants (stants). In *4th International Conference on Wireless Mobile Communication and Healthcare, At Athen, Greece* (2014), IEEE, pp. 39–44. <sup>6</sup>
- [119] SALEHI, S., MOSTOFI, N., AND BLESER, G. A practical in-field magnetometer calibration method for imus. In *Proceedings of the IROS Workshop on Cognitive Assistive Systems: Closing the Action-Perception Loop* (2012), pp. 39–44. <sup>7</sup>
- [120] SALEHI, S., AND STRICKER, D. Validation of a low-cost inertial exercise tracker. In *Proceedings of the 9th International Conference on Sensor Networks, Sensornets 2020*. <sup>8</sup>
- [121] SAMSUNG GEAR FIT2 PRO. <https://www.samsung.com/global/galaxy/gear-fit2-pro/>. [Online; accessed 25-January-2020]. <sup>5, 31</sup>
- [122] SCHEPERS, H., GIUBERTI, M., AND BELLUSCI, G. Xsens mvn: Consistent tracking of human motion using inertial sensing. In *Xsens Technologies*. 2018, pp. 1–8. <sup>16</sup>



- [123] SEEL, T., RAISCH, J., AND SCHAUER, T. Imu-based joint angle measurement for gait analysis. *Sensors* 14, 4 (2014), 6891–6909. 18, 56, 57
- [124] SEEL, T., RAISCH, J., AND SCHAUER, T. Imu-based joint angle measurement for gait analysis. *Sensors* 14, 4 (2014), 6891–6909. 18, 56, 59, 60, 95, 143
- [125] SHIEH, J., AND KEOGH, E. i sax: indexing and mining terabyte sized time series. In *Proceedings of the 14th ACM SIGKDD international conference on Knowledge discovery and data mining* (2008), pp. 623–631. 100
- [126] SHIRATORI, T., PARK, H. S., SIGAL, L., SHEIKH, Y., AND HODGINS, J. K. Motion capture from body-mounted cameras. *ACM Transactions on Graphics (TOG)* 30, 4 (2011), 31. 30
- [127] SHOTTON, J., SHARP, T., KIPMAN, A., FITZGIBBON, A., FINOCCHIO, M., BLAKE, A., COOK, M., AND MOORE, R. Real-time human pose recognition in parts from single depth images. *Communications of the ACM* 56, 1 (2013), 116–124. 30
- [128] SHUSTER, M. D. A survey of attitude representations. *Navigation* 8, 9 (1993). 49
- [129] SHUSTER, M. D., AND OH, S. D. Three-axis attitude determination from vector observations. *Journal of guidance and Control* 4, 1 (1981), 70–77. 86
- [130] SNYDER, K. R., EARL, J. E., O CONNOR, K. M., AND EBERSOLE, K. T. Resistance training is accompanied by increases in hip strength and changes in lower extremity biomechanics during running. *Clinical Biomechanics* 24, 1 (2009), 26–34. 3
- [131] SOLA, J. Quaternion kinematics for the error-state kf. *Laboratoire dAnalyse et dArchitecture des Systemes-Centre national de la recherche scientifique (LAAS-CNRS), Toulouse, France, Tech. Rep* (2012). 138
- [132] SPIRE HEALTH TRACKER . <https://spirehealth.com/pages/spire-health-tag-main>. [Online; accessed 25-January-2020]. 31
- [133] SPRINGMANN, J. C., CUTLER, J. W., AND BAHCIIVAN, H. Magnetic sensor calibration and residual dipole characterization for application to nanosatellites. *Toronto, Ontario Canada* (2010). 11
- [134] STEELE, J. M. *The Cauchy-Schwarz master class: an introduction to the art of mathematical inequalities*. Cambridge University Press, 2004. 19
- [135] SUKHANOV, S., WU, R., DEBES, C., AND ZOUBIR, A. Dynamic pattern matching with multiple queries on large scale data streams. *Signal Processing* 171 (2020), 107402. 104
- [136] SUNG, M., AND PENTLAND, A. Livenet: Health and lifestyle networking through distributed mobile devices. *Proceedings WAMES* (2004). 32

- [137] SZUHANY, K. L., BUGATTI, M., AND OTTO, M. W. A meta-analytic review of the effects of exercise on brain-derived neurotrophic factor. *Journal of psychiatric research* 60 (2015), 56–64. <sup>2</sup>
- [138] TAETZ, B., BLESER, G., AND MIEZAL, M. Towards self-calibrating inertial body motion capture. In *2016 19th International Conference on Information Fusion (FUSION)* (2016), IEEE, pp. 1751–1759. <sup>23</sup>
- [139] TANG, S. L. P. Recent developments in flexible wearable electronics for monitoring applications. *Transactions of the Institute of Measurement and Control* 29, 3-4 (2007), 283–300. <sup>32</sup>
- [140] TAYLOR, C. B., SALLIS, J. F., AND NEEDLE, R. The relation of physical activity and exercise to mental health. *Public health reports* 100, 2 (1985), 195. <sup>2</sup>
- [141] TOGNETTI, A., BARTALESI, R., LORUSSI, F., AND DE ROSSI, D. Body segment position reconstruction and posture classification by smart textiles. *Transactions of the Institute of Measurement and Control* 29, 3-4 (2007), 215–253. <sup>34</sup>
- [142] TRIVISIO. <https://www.trivisio.com/inertial-motion-tracking>. [Online; accessed 25-January-2020]. <sup>5, 42, 49</sup>
- [143] UM, T. T., BABAKESHIZADEH, V., AND KULIĆ, D. Exercise motion classification from large-scale wearable sensor data using convolutional neural networks. In *2017 IEEE/RSJ International Conference on Intelligent Robots and Systems (IROS)* (2017), IEEE, pp. 2385–2390. <sup>26</sup>
- [144] VAN DEN NOORT, J. C., SCHOLTES, V. A., AND HARLAAR, J. Evaluation of clinical spasticity assessment in cerebral palsy using inertial sensors. *Gait & posture* 30, 2 (2009), 138–143. <sup>4</sup>
- [145] VASCONCELOS, J., ELKAIM, G., SILVESTRE, C., OLIVEIRA, P., AND CARDEIRA, B. A geometric approach to strapdown magnetometer calibration in sensor frame. *Navigation, Guidance and Control of Underwater Vehicles* 2, 1 (2008), 1–11. <sup>12, 46, 47, 48, 56</sup>
- [146] VELIZ, R. R., SUAREZ-ARRONES, L., REQUENA, B., HAFF, G. G., FEITO, J., AND DE VILLARREAL, E. S. Effects of in-competitive season power-oriented and heavy resistance lower-body training on performance of elite female water polo players. *The Journal of Strength & Conditioning Research* 29, 2 (2015), 458–465. <sup>2</sup>
- [147] VICON, MOTION CAPTURE . <https://www.vicon.com/motion-capture/>. [Online; accessed 25-January-2020]. <sup>5, 29</sup>
- [148] WANG, Z., AND DISSANAYAKE, G. Observability analysis of slam using fisher information matrix. In *2008 10th International Conference on Control, Automation, Robotics and Vision* (2008), IEEE, pp. 1242–1247. <sup>20, 58</sup>

- [149] WATANABE, Y., HATANAKA, T., KOMURO, T., AND ISHIKAWA, M. Human gait estimation using a wearable camera. In *Applications of Computer Vision (WACV), 2011 IEEE Workshop on* (2011), IEEE, pp. 276–281. 30
- [150] WEBER, M., BLESER, G., LIWICKI, M., AND STRICKER, D. Unsupervised motion pattern learning for motion segmentation. In *Proceedings of the 21st International Conference on Pattern Recognition (ICPR2012)* (2012), IEEE, pp. 202–205. 27
- [151] WOLLIN, M., PURDAM, C., AND DREW, M. K. Reliability of externally fixed dynamometry hamstring strength testing in elite youth football players. *Journal of Science and Medicine in Sport* 19, 1 (2016), 93–96. 3
- [152] WU, R., SUKHANOV, S., AND DEBES, C. Real time pattern matching with dynamic normalization. *arXiv preprint arXiv:1912.11977* (2019). 100, 126
- [153] XSSENS MTI . <http://www.xsens.com/en/general/mti>. [Online; accessed 25-January-2020]. 5, 30, 32, 34, 42, 51
- [154] ZHU, R., AND ZHOU, Z. A real-time articulated human motion tracking using tri-axis inertial/magnetic sensors package. *IEEE Transactions on Neural systems and rehabilitation engineering* 12, 2 (2004), 295–302. 23
- [155] ZINNEN, A., BLANKE, U., AND SCHIELE, B. An analysis of sensor-oriented vs. model-based activity recognition. In *2009 International Symposium on Wearable Computers* (2009), IEEE, pp. 93–100. 14
- [156] ZUMER, J., SLAVIC, J., AND BOLTEZAR, M. Minimization of the positional errors for an accurate determination of the kinematic parameters of a rigid-body system with miniature inertial sensors. *Mechanism and Machine Theory* (2014). 16



# Curriculum Vitae

**Name:** Sarvenaz Salehi Mourkani

## Education

2009 - 2011 — **Mid Sweden University**

Sundsvall, Sweden

*Master of Science*, Electronics Design

2001 - 2006 — **University of Isfahan**

Isfahan, Iran

*Bachelor of Science*, Computer Engineering

## Professional experience

2016 - — **Daimler Protics**

Leinfelden-Echterdingen, Germany

*Software developer*

2011 - 2016 — **German Research Center for Artificial Intelligence (DFKI)**

Kaiserslautern, Germany

*Researcher*

2009 - 2011 — **Mid Sweden University**

Sundsvall, Sweden

*Research assistance*

2008 - 2009 — **Palizafzar**

Tehran, Iran

*Embedded system developer*

2006 - 2008 — **Freelance software developer**

Tehran, Iran

2004 - 2008 — **Satrash Company**

Tehran, Iran

*Hardware technician*



# Publication list

1. Sarvenaz Salehi, Navid Mostofi, and Gabriele Bleser. A practical in-field magnetometer calibration method for IMUs. In *Proceedings of the IROS Workshop on Cognitive Assistive Systems: Closing the Action-Perception Loop*, 2012
2. Sarvenaz Salehi, Gabriele Bleser, Norbert Schmitz, and Didier Stricker. A low-cost and light-weight motion tracking suit. In *Proceedings of 10th International Conference on Ubiquitous Intelligence and Computing (UIC)*, 2013
3. Sarvenaz Salehi, Gabriele Bleser, and Didier Stricker. Design and development of low-cost smart training pants (stants). In *Proceedings of 4th International Conference on Wireless Mobile Communication and Healthcare*, 2014
4. Sarvenaz Salehi, Gabriele Bleser, Attila Reiss, and Didier Stricker. Body-IMU auto-calibration for inertial hip and knee joint tracking. In *Proceedings of 10th EAI International Conference on Body Area Networks, ICST (Institute for Computer Sciences, Social-Informatics and Telecommunications Engineering)*, 2015
5. Sarvenaz Salehi and Didier Stricker. Validation of a low-cost inertial exercise tracker. In *Proceedings of 9th International Conference on Sensor Networks (Sensornets)*, 2020.
6. Sarvenaz Salehi and Didier Stricker. Strength exercise monitoring with inertial sensors Submitted in *Communications in Computer and Information Science book series (CCIS)*, Springer.